Master's thesis

NTNU
Norwegian University of Science and Technology
Faculty of Natural Sciences
Department of Physics

Ellaine Rose Adricula Beronio

Plasmons and Magnons in Antiferromagnetic FeSn: A Time-Dependent Density Functional Theory Study

Master's thesis in Physics
Supervisor: Alireza Qaiumzadeh
May 2023

NTNU
Norwegian University of
Science and Technology

Ellaine Rose Adricula Beronio

Plasmons and Magnons in Antiferromagnetic FeSn: A Time-Dependent Density Functional Theory Study

Master's thesis in Physics
Supervisor: Alireza Qaiumzadeh
May 2023

Norwegian University of Science and Technology
Faculty of Natural Sciences
Department of Physics

NTNU
Norwegian University of
Science and Technology

ABSTRACT

This study is an exploration, via time-dependent density functional theory, of collective excitations in FeSn, a layered antiferromagnetic metal with a kagome structure. At present, interest in FeSn is spurred by novel properties promised by the predicted flat and linearly dispersive electronic bands of ideal kagome lattices.

This work focuses on plasmons, which are quanta of longitudinal charge density oscillations, in bulk and monolayer FeSn. Having been initially conceived as an exploration of the possibility of plasmon-magnon coupling, this thesis also includes a description of magnons, the quanta of spin-waves, in the bulk and monolayer forms of the material. While magnons have been discussed in existing literature on FeSn, plasmon behaviour in the material has yet to be described. The monolayer form of FeSn has not been explored in published papers, although efforts to synthesise FeSn thin films are ongoing.

From analysis of the dielectric function and loss function of FeSn for different wave vectors along the path $\overline{\Gamma M}$ of the first Brillouin zone, plasmons in bulk FeSn are found to be long-lived at the Brillouin zone boundary and the bulk plasmon dispersion is quadratic for larger wave vectors. In contrast, monolayer plasmons are short-lived and heavily influenced by the continuum of single-particle excitations that cause Landau damping and eventual plasmon decay. From the calculations, several points of departure from the expected plasmon dispersion curve for three-dimensional and two-dimensional systems have been observed for the bulk and monolayer, respectively. Most prominent is the gapped and nearly flat dispersion of monolayer plasmons. In relation to magnons, the dispersion for bulk FeSn along $\overline{\Gamma M}$ is found to agree with published reports, while calculations for the monolayer magnon dispersion produced unexpected features.

In bringing out deviations from analytical predictions, the findings open up avenues for further investigation into the collective excitations of FeSn. The results

also highlight the value of examining real materials using ab-initio computational techniques that can, in principle, provide a more realistic description of material properties.

PREFACE

This thesis marks the culmination of my two years as a master's student in physics. It is my first exposure to TDDFT and the study of plasmons and magnons. To produce it, I needed to learn not only TDDFT, linear response theory and collective excitations, but also the more practical matters of using Elk, navigating HPC environments, practising patience, and keeping faith. I started my master's in the middle of the pandemic, away from everyone I know. Getting to this point was not at all easy, but my gut feel is it is worth it.

Without the guidance and encouragement of my supervisor Alireza Qaiumzadeh, this work would not have been possible. For his generosity, I will always be grateful.

I am also thankful to Dr. Peter Elliott and Dr. Sangeeta Sharma for their valuable advice on performing computations in Elk.

Computational resources were provided by Sigma2 - the National Infrastructure for High Performance Computing and Data Storage in Norway through Project NN10006K.

I dedicate this to the memory of my parents, gone recently and too soon.
To them, I owe everything.

For Loise, for things too important to name, always.

Ad majorem Dei gloriam.

CONTENTS

LIST OF FIGURES

ABBREVIATIONS

- **2D, 3D** two-dimensional, three-dimensional
- **AFM** Antiferromagnetic
- **ALDA** Adiabatic local density approximation
- **DFT** Density functional theory
- **DOS** Density of states
- **EEL** Electron energy loss
- **EELS** Electron energy loss spectra
- **KS** Kohn-Sham
- **LAPW** Linearised augmented plane wave
- **LDA** Local density approximation
- **NTNU** Norwegian University of Science and Technology
- **RPA** Random-phase approximation
- **TDDFT** Time-dependent density functional theory
- **TDKS** Time-dependent Kohn-Sham

CHAPTER

ONE

INTRODUCTION

Collective excitations [1–4] are phenomena associated with the collective motion of the particles of a system. The motion of the particles is wave-like and can be described by oscillators [5–8]. Plasmons and magnons are types of collective excitations. Analogous to phonons, which are the quanta of vibrations of the crystal lattice [9, 10] and perhaps the most well-known type of collective excitation, plasmons are the quanta of longitudinal charge density oscillations, while magnons are the quanta of spin-waves in a material.

In generating plasmons and magnons, it is the electrons of a material that are involved. In the case of the former, the excitation is due to the motion of electrons themselves, while in the case of the latter, the excitation comes from the precession of the spin angular momentum of electrons. Thus, the study of plasmons and magnons provides a window into the electronic and magnetic properties of solids. Moreover, because plasmons and magnons are collective excitations, which are possible only because of interactions amongst particles, their study elucidates the many-body nature of materials.

This work started out as an exploration, via time-dependent density functional theory (TDDFT), of the possibility of plasmon-magnon coupling in FeSn, particularly its monolayer form. Compared to phonon-plasmon and phonon-magnon interactions, little attention has been paid to plasmon-magnon [11–13] interaction in research. This, fundamentally, is due to that fact that in bulk (three-dimensional) materials, there usually exists a mismatch in the energy (or frequency) regimes where magnons (up to hundreds of meV) and plasmons (up to tens of eV) occur [14, 15]. Two-dimensional materials (with one-atom or up to several-atoms thickness), however, are predicted to sustain a gapless plasmon dispersion, presenting

the possibility of a compatible energy range for plasmon-magnon hybridisation [14, 15].

However, in light of obtained results as well as limitations set by time and particularities of the software used, the focus of the work shifted to mainly the exploratory description and analysis of plasmons in bulk and monolayer FeSn. Nonetheless, the results obtained from the magnon calculations for the bulk and monolayer structures are presented and discussed here as well.

The choice of material for study in this thesis is motivated by recent attention paid to the antiferromagnetic kagome material FeSn. Characteristics of FeSn that have sparked research curiosity are discussed later in this chapter. At present, efforts to fabricate FeSn thin films [16–18] are ongoing, encouraged by the possibilities presented by the interesting properties of kagome lattices as well as by spintronic technologies based on antiferromagnets [19, 20], including terahertz memory and logic processing [21]. A research group under QuSpin at NTNU is actively working on growing FeSn via molecular beam epitaxy on semiconducting substrates.

As of this writing, the body of published work on FeSn is small but growing. The existing literature consists mostly of studies focusing on the material's electronic band structure [22–28] and there are papers that discuss magnons in bulk FeSn [29–32]. There have been no studies on monolayer FeSn, however. Plasmons, in particular, have not been discussed in published literature on any FeSn structure.

In this thesis, TDDFT is used to computationally obtain the dispersion relations of plasmons and magnons in FeSn. Dispersion relations show how the frequency (ω) or energy ($\hbar\omega$) of an excitation varies with the excitation's wave vector ($\mathbf{q}$). This work considers the bulk and monolayer structures of FeSn. The monolayer is modelled by a slab structure consisting of two kagome Fe_3Sn layers. The bulk and monolayer structures are described in a later chapter on computational details.

The emphasis in this work is on plasmons, which provide another way of looking at the electronic structure and properties of a material. Plasmons are closely linked to how a material interacts with electromagnetic fields. For instance, in metals, the plasmon frequency is the threshold for electromagnetic field penetration into the material [9, 10, 33]. Below the plasma frequency, the material is impene-

trable to light, reflecting it entirely. In addition, studying plasmons via TDDFT presents an opportunity to look into the dielectric function, a key quantity in understanding a material's optical properties. Considering the growing interest in FeSn, which will continue once thin films and atomically thin structures are synthesised, the study of the electronic excitations of this material becomes relevant.

The discussion in this work flows as follows: Chapter 1 (current chapter) introduces the study and gives a brief description of FeSn as well as a short introduction to plasmons and magnons (next sections); Chapter 2 describes the theoretical framework of TDDFT; Chapter 3 is a discussion of linear response theory and how it can be used to study plasmons and magnons in TDDFT; Chapter 4 is dedicated to the description of the bulk and slab models of FeSn used in this work; Chapters 5 and 6 present and discuss the results obtained from the calculations; and Chapter 7 contains conlcuding remarks and recommendations for further study.

1.1 FeSn

Recent interest in FeSn, a layered antiferromagnetic metal, springs from the material's kagome structure. A kagome pattern is a mesh of triangles with shared vertices within a two-dimensional hexagonal lattice, as seen in Figure 1.1.1 (a). The distinct star shapes of the lattice call to mind the patterns of Japanese kagome basket weaving, hence the name.

In FeSn, the Fe atoms form the characteristic triangles of the kagome lattice. FeSn consists of alternating magnetic kagome Fe_3Sn layers and honeycomb Sn layers (Figure 1.1.1 (b)). The oppositely oriented magnetisation of neighbouring kagome layers makes the material antiferromagnetic. The spins lie within the planes of the kagome layers. [34–36].

Kagome materials are predicted to exhibit properties that make them an interesting platform for investigating exotic physical phenomena. The theoretically predicted electronic band structure (shown in Figure 1.1.1(c)) of a two-dimensional kagome lattice features both linearly dispersive bands, which are associated with massless fermions and topologically protected states [22, 24, 37–39], as well as non-dispersive flat bands, which indicate localised electrons and strong electron correlation [26, 40–44].

Unlike other bulk kagome materials such as $Co_3Sn_2S_2$ or Fn_3Sn_2, for which experimental observations have failed to register both the linear and flat bands,

bulk FeSn has been observed to retain these band structure features associated with the ideal two-dimensional kagome lattice [22].

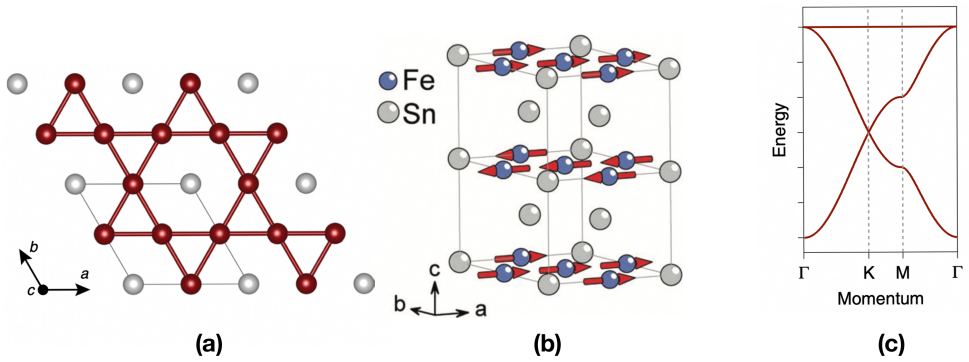

Figure 1.1.1: (a) The kagome pattern formed by the Fe atoms (red spheres) of FeSn. The white spheres are Sn atoms situated in the Fe_3Sn layer. (b) The alternating Fe_3Sn and Sn layers of FeSn. The Fe_3Sn layers are magnetic. (c) The predicted electronic band structure of a two-dimensional kagome lattice. The flat band and the linearly dispersive bands crossing at K are shown. The figures are from [34] and [22].

As mentioned earlier, most studies on FeSn have focused on the electronic band structure characteristics. Flat bands have been experimentally observed via angle-resolved photo-emission spectroscopy [22, 25, 29] in bulk FeSn and in the interface of an FeSn-semiconductor heterostructure via planar tunneling spectroscopy [23]. In studies discussing spin-waves in bulk FeSn, spin-waves have been observed in inelastic neutron scattering experiments to extend to 120 meV and to be dampened at higher energies due to interactions with Stoner excitations [29, 31]. At the M point, magnon energy is around 80 meV to 90 meV from neutron scattering measurements and calculations from linear spin-wave theory [29, 30, 34]. A more recent study based on neutron scattering measurements found indications of magnetoelastic coupling as well as spin-phonon coupling in bulk FeSn [32].

1.2 Introduction to Plasmons

In a metal, the phenomenon of longitudinal charge density oscillations, collective modes that were first systematically studied by Bohm and Pines [45–47], can be pictured by considering the sea of conduction electrons. These conduction electrons, which constitute an electron gas and, hence, a plasma, freely move over a positively charged background of ion cores made up of the nuclei and core electrons. When this electron gas is displaced relative to the positive background, charge separation generates an electric field, triggering a restoring force and bringing about the oscillation of the electron sea [6, 48, 49].

The macroscopic dynamics of electrons in response to an external potential is described by the dielectric function $\varepsilon(\omega)$, which in the classical Drude model takes the form [33]

$$\varepsilon(\omega) = 1 - \frac{\omega_p^2}{\omega(\omega + i/\tau)}, \tag{1.1}$$

which, for $\omega\tau >> 1$, reduces to

$$\varepsilon(\omega) = 1 - \frac{\omega_p^2}{\omega^2}. \tag{1.2}$$

In the above expressions, ω denotes frequency, i is the imaginary unit for which $i^2 = -1$, τ is the relaxation time that is the average time between electron collisions, and ω_p is the plasma frequency [33]

$$\omega_p = \sqrt{\frac{4\pi n e^2}{m}}, \tag{1.3}$$

where n and m stand for the electron density and effective electron mass, respectively.

At the plasma frequency, the dielectric function is zero ($\varepsilon(\omega_p) = 0$), which is characteristic of collective longitudinal oscillation modes [6, 33] whose quanta are called plasmons. These collective longitudinal modes are free modes of oscillation with natural frequency ω_p, and they persist in the electron gas in the absence of an external driving force [6]. The longitudinal oscillations, whose quanta are also called bulk plasmons or volume plasmons, are illustrated in Figure 1.2.1.

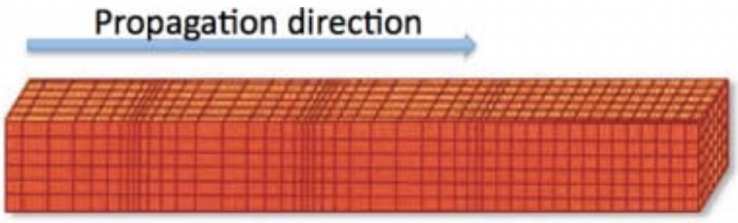

Figure 1.2.1: Illustration of the longitudinal oscillations of the conduction electrons in a metal. The blue arrow points to the propagation direction of the longitudinal wave. Figure taken from [50].

The general form of the dielectric function is also a function of the wave vector $\mathbf{q}$, reflecting non-locality: $\varepsilon(\mathbf{q}, \omega)$ [6, 33, 51]. From analytical considerations of the homogenous electron gas, the plasmon dispersion relation that this $\mathbf{q}$-dependent dielectric function yields is dependent on dimensionality. For three-dimensional

(bulk) systems, $\omega(q)$ is almost dispersionless near $\mathbf{q} = 0$ and becomes quadratic farther away [6, 48, 52]. In contrast, for two-dimensional systems, $\omega(q) \approx \sqrt{q}$ in the small wave-vector limit [52, 53]. These dispersions are illustrated in Figure 1.2.2.

The longitudinal character of plasmon modes can be discerned by considering the wave equation, which is derived from Maxwell's equations and describes traveling waves [33]:

$$q^2\mathbf{E} - \mathbf{q}(\mathbf{q}\cdot\mathbf{E}) = \varepsilon(\mathbf{q},\omega)\frac{\omega^2}{c^2}\mathbf{E}, \tag{1.4}$$

where the c is the speed of light. When the wave vector of the propagating wave $\mathbf{q}$ is parallel to the electric field $\mathbf{E}$, the equation becomes

$$\varepsilon(\mathbf{q},\omega)\frac{\omega^2}{c^2}\mathbf{E} = 0, \tag{1.5}$$

which implies that

$$\varepsilon(\mathbf{q},\omega) = 0. \tag{1.6}$$

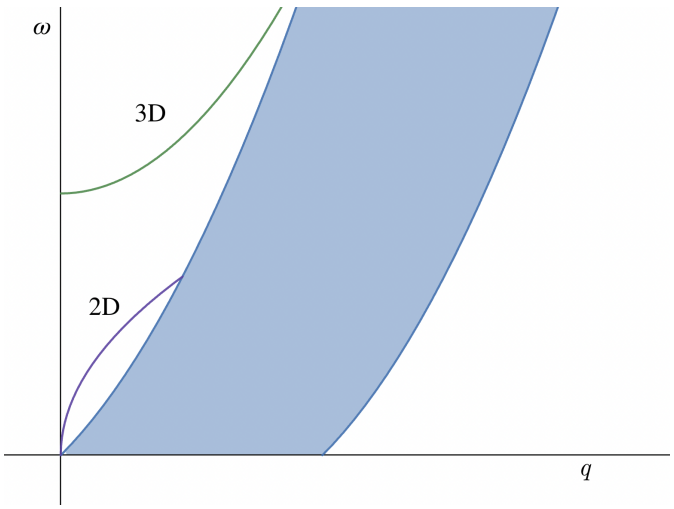

Figure 1.2.2: Plasmon dispersion in different dimensions (green for three dimensions, purple for two dimensions) and the electron-hole continuum (blue shaded region).

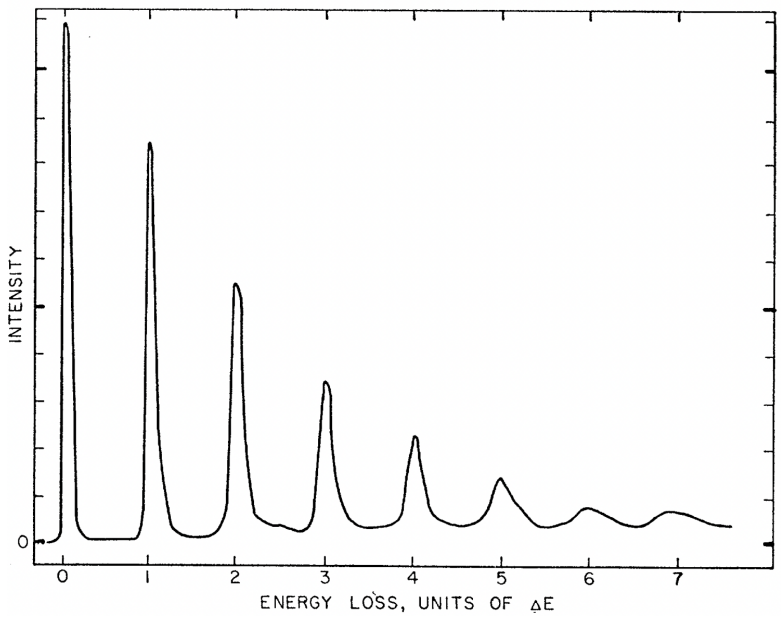

Figure 1.2.3: The energy loss peaks obtained in [54] appear in multiples of the plasmon energy $\Delta E = \hbar\omega_p$. Figure taken from [54].

Being longitudinal, plasmon modes do not couple to electromagnetic fields [6, 49, 50]. Thus, they cannot be excited by light. Plasmons, however, can be generated by bombarding the electron gas with electrons from an external source. The incoming electrons lose energy as they generate longitudinal charge density oscillations [6]. An early experimental observation [54] of plasmons in metals occurred when a beam of electrons was directed onto a sheet of Al, and the energy loss peaks in the resulting spectrum were found to correspond to multiples of $\hbar\omega_p$ ($\hbar$ being the reduced Planck's constant), which is the plasmon energy. Such procedure forms the basis of electron energy loss spectroscopy (EELS) [55–58], the standard experimental technique for studying plasmons.

Spectra from EELS are given by the loss function [6, 59]

$$-\mathrm{Im}(\varepsilon^{-1}(\mathbf{q},\omega)) = \frac{\mathrm{Im}(\varepsilon(\mathbf{q},\omega))}{[\mathrm{Re}(\varepsilon(\mathbf{q},\omega))]^2 + [\mathrm{Im}(\varepsilon(\mathbf{q},\omega))]^2}. \tag{1.7}$$

Plasmon peaks in EEL spectra appear when the real part of the dielectric function ($\mathrm{Re}(\varepsilon)$) is zero and the imaginary part of the dielectric function ($\mathrm{Im}(\varepsilon)$) is small [60–63]. Regions with $\mathrm{Im}(\varepsilon) \neq 0$ belong to the electron-hole continuum, which is dominated by excitations that occur when electrons transition to a higher energy state [51, 52]. This continuum, illustrated in Figure 1.2.2 is a region of plasmon decay known as Landau damping. It shall be discussed further, along with the results of the study.

Much of the literature in plasmonics concerns another type of collective excitations called surface plasmons [64, 65], which are different from the plasmons in three- or two-dimensional systems described above. Surface plasmons are oscillation modes confined to the interface between a metal and a dielectric (which may be vacuum) [6, 49, 50]. These oscillations consist of longitudinal and transverse components of electric and magnetic fields and thus can couple to light [6, 49, 66]. In contrast, the three- and two-dimensional plasmons are purely longitudinal oscillation modes. Indeed, surface plasmons almost exclusively exist as surface plasmon polaritons [66], a hybrid mode where charge oscillations couple to electromagnetic fields. They are thus, basically, electromagnetic waves modified by the charge density in which they propagate [66].

Like plasmons in two-dimensional systems, the dispersion curve for surface plasmons go to zero as $\mathbf{q} \to 0$. However, with increasing q, the surface plasmon dispersion (with vacuum for the dielectric) asymptotically approaches the characteristic value $\omega_p/\sqrt{2}$, with ω_p denoting the bulk plasmon frequency of the material [49, 50]. The surface plasmon dispersion for a metal is shown in Figure 1.2.4, where the surface plasmon frequency is given by [6]

$$\omega_s = \frac{\omega_p}{\sqrt{\varepsilon_d + 1}}, \tag{1.8}$$

with ε_d denoting the dielectric constant of the other material that forms the interface. For vacuum, $\varepsilon_d = 1$. In contrast to longitudinal plasmons, which require $\varepsilon(\omega) = 0$, surface plasmons are marked by the condition $\varepsilon(\omega) < 0$ [50, 66].

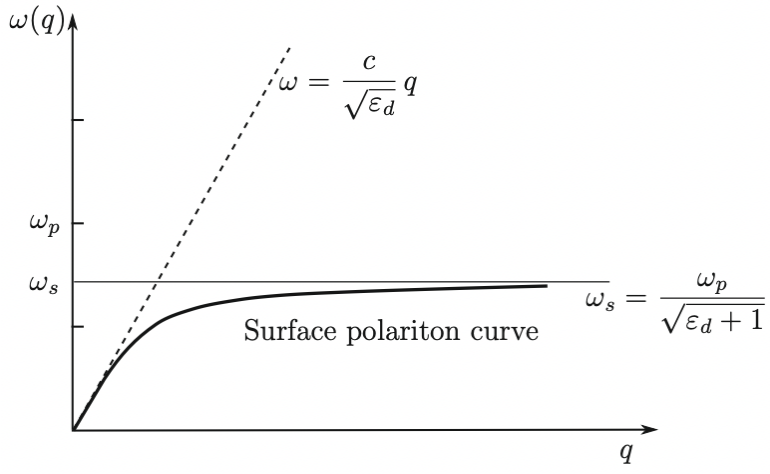

Figure 1.2.4: The surface plasmon (surface plasmon polariton) dispersion is depicted as a solid curve. The dashed line represents the light line. Figure taken from [6].

Such dispersion behaviour persists in thin metallic films for which the surface

plasmon dispersion takes the form [67]:

$$\omega = \frac{\omega_p}{\sqrt{2}}\sqrt{1 \pm e^{-qd}}, \tag{1.9}$$

where d denotes the thickness of the thin film. For atomically thin materials ($qd << 1$), a dispersion that goes with $\sqrt{q}$ is obtained [67]. The surface plasmon dispersion for thin films is shown in Figure 1.2.5.

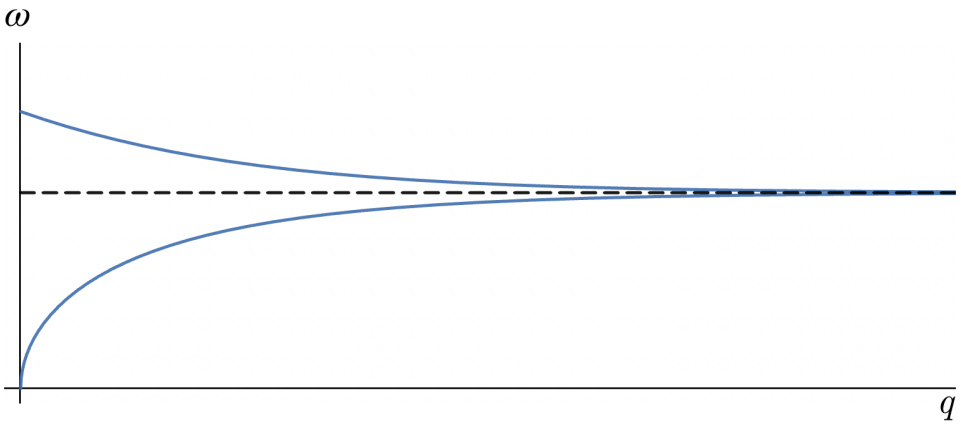

Figure 1.2.5: Surface plasmon dispersion for a thin film. The dashed line is $\omega_p/\sqrt{2}$.

1.3 Introduction to Magnons

To visualise magnons, one can imagine a one-dimensional lattice of spins, each of which is coupled to its neighbours via the exchange interaction, with energy given by [9, 68]

$$E = -2J\sum_{p=1}^{N}\mathbf{S}_p \cdot \mathbf{S}_{p+1}, \tag{1.10}$$

where the dot product describes the coupling between neighbouring spins ($\mathbf{S}_p$ and $\mathbf{S}_{p+1}$) and the sign of the exchange parameter J indicates how the spins are ordered. In the expression above, $J > 0$ signifies ferromagnetic ordering, as neighbouring spins align parallel to each other to minimise the interaction energy E. On the other hand, antiferromagnetic ordering is implied by $J < 0$, with each spin aligning antiparallel to its neighbours to achieve minimum energy [68].

In general, the exchange interaction is described by the Heisenberg Hamiltonian, which can accommodate beyond nearest-neighbour interaction [68]:

$$\hat{H} = -\sum_{ij} J_{ij}\, \hat{\mathbf{S}}_i \cdot \hat{\mathbf{S}}_j, \tag{1.11}$$

where $\hat{\mathbf{S}}_i$ refers to the spin operator for lattice site i and the exchange parameter J_{ij} is no longer the same for all terms.

The low-energy excited state of the ordered magnetic system is obtained when the spins precess at a small angle about their original direction [9, 33, 68]. The motion of these precessing spins trace out a spin-wave that propagates through the chain [69]. This is illustrated in Figure 1.3.1.

The quanta of the spin-waves are called magnons. Instead of a high-energy excited state created by flipping a single spin, that single spin flip is, so to speak, distributed, via a small canting of the spins, throughout the chain [70]. The one-dimensional spin chain model can be generalised to magnetically ordered lattices of larger dimensions.

Semi-classically, spin-waves are derived from the expression for the exchange interaction by considering the torque on the spin moment and the resulting equation of motion for the spins [9, 68, 70]. Meanwhile, a quantum mechanical approach employs the use of spin ladder operators, which are then expressed as creation and annihilation operators [6, 70]. Spin-waves in antiferromagnets are modelled by considering two lattices with opposite magnetisation [6, 70].

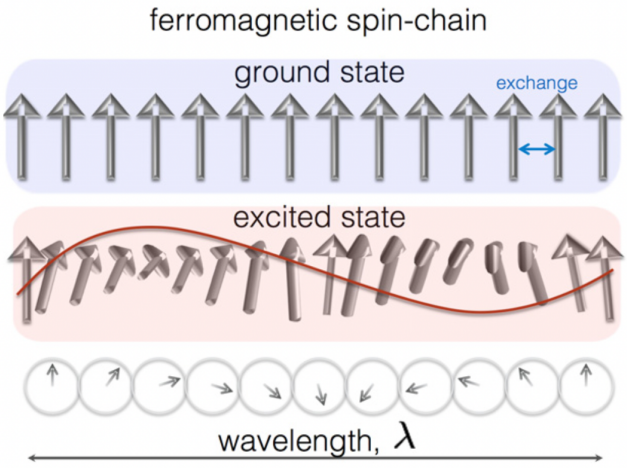

Figure 1.3.1: Spin-waves arising from the small-angle precession of the spins of a one-dimensional spin chain. Figure taken from [71].

Theoretically, ideal ferromagnetic systems are predicted to have a quadratic dispersion relation in the limit of small wave vectors, while ideal antiferromagnets

are predicted to have a linear dispersion relation in the small-$\mathbf{q}$ limit [9, 33, 70].

Magnon dispersions can be obtained more generally via spin-wave theory by adding more terms to the model Hamiltonian:

$$\hat{H} = -\sum_{ij} J_{ij}\,\hat{\mathbf{S}}_i \cdot \hat{\mathbf{S}}_j - K\sum_i (\hat{S}_i^z)^2 - \sum_{ij} \mathbf{D}_{ij} \cdot (\hat{\mathbf{S}}_i \times \hat{\mathbf{S}}_j). \tag{1.12}$$

In the above, the second term is the uniaxial anisotropy term, which accounts for the possibility of magnetic moments preferring to align in a certain direction (in this case, the z-direction, with S_i^z being the z-component of the spin operator for lattice site i.) [68]. If the anisotropy parameter $K > 0$, the maximal ordering of spins (along z) is favoured and fluctuations are energetically costly. On the other hand, if $K < 0$, energy lowering is achieved by reducing the component $\hat{S}_i^z$, implying the destabilisation of spin order. The third term is the Dzyaloshinkii-Moriya interaction (DMI) term, which applies only to systems with strong spin-orbit coupling and that lack inversion symmetry [68, 70]. To reduce energy, the DMI interaction forces the spins to be at right angles with respect to each other while staying in the plane perpendicular to the DMI vector $\mathbf{D}_{ij}$. If the two spins are initially perfectly aligned in a system with strong DMI, the effect of the DMI vector is to introduce a small cant to the spins [68, 70].

Like plasmons, magnons experience Landau damping when they interact with spin-flip single-particle excitations, which metallic magnets support along with spin-waves [69, 72]. These excitations, which involve electrons flipping their spins as they transition to excited states, are called Stoner excitations. These excitations form the Stoner continuum, visualised in Figure 1.3.2, in the $(\mathbf{q}, \omega)$ plane.

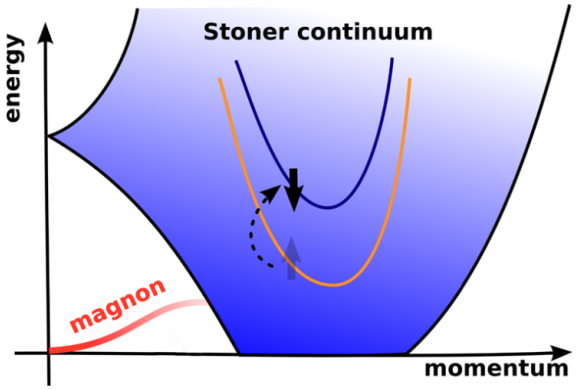

Figure 1.3.2: Magnons decay into single-particle spin-flip excitations when they enter the Stoner continuum. The figure (modified) is taken from [73].

The myriad possibilities for the technological application of magnons, includ-

ing information transmission and processing, have launched an entire field called magnonics, a subfield of spintronics focusing on the manipulation and utilisation of magnons [70, 74].

A common method to experimentally observe magnons is inelastic neutron scattering (INS) [75, 76]. An unpolarised beam of neutrons, which have magnetic moments that can interact with the magnetic moments of the material being probed, is directed onto a sample of the material. The change in momentum obtained from neutrons that scatter in the process gives information about the spin excitations. Spin-wave excitations are encoded in the differential scattering cross-section [77]

$$\frac{d^2\sigma}{d\Omega d\epsilon_f} \propto \frac{\hbar}{\pi}\frac{k_f}{k_i}S(\mathbf{Q},\omega) \tag{1.13}$$

for solid angle Ω and scattered neutron energy ϵ_f. The symbol σ stands for the cross section of the target and the initial and final momenta of the neutrons are signified by k_i and k_f, respectively. The quantity $S(\mathbf{Q},\omega)$ (for which $\mathbf{Q} = k_f - k_i$) is proportional to the spin-spin response function χ, a quantity which is obtainable via linear response theory and TDDFT, and which shall be discussed later.

CHAPTER

TWO

TIME-DEPENDENT DENSITY FUNCTIONAL THEORY

Time-dependent density functional theory (TDDFT) is the extension of ground-state density functional theory (DFT) to the time domain [78]. TDDFT allows the description of the dynamical response of a system to perturbation, such as external magnetic or electric fields, and thus makes possible the simulation of spectroscopic data and the study of excited-state properties [59, 79].

Like DFT, which applies only to the determination of ground-state observables, TDDFT replaces the many-body wave function with the electron density as the central quantity in calculations. The many-body wave function, as it is a function of the spatial coordinates of all the electrons and nuclei constituting a system, rapidly becomes too complex to compute as the number of particles increases. The electron density (given in (2.4)), in contrast, is always a function of only three spatial coordinates, no matter the system size. The sheer reduction in the number of variables gives DFT (and TDDFT) an advantage over wave-function-based methods in terms of computational efficiency [80, 81]. This has resulted in the explosion of the popularity of DFT [82], as implemented in various computer codes [83, 84], within the fields of physics, chemistry, chemical engineering, and materials science [85–89].

2.1 Density functional theory

DFT is a means of taming the complexity of the many-body problem found at the core of the first-principles study of atoms, molecules, and solids. In studying materials, a first-principles or ab-initio approach uses only as basis the principles of quantum mechanics and the atomic composition of the system, without recourse

to empirical parameters [90]. In general, materials are described by the many-body Hamiltonian (in atomic units) [91]

$$\begin{aligned}\hat{H} = &- \sum_{i}^{N} \frac{\boldsymbol{\nabla}_i^2}{2m_e} - \sum_{I}^{M} \frac{\boldsymbol{\nabla}_i^2}{2M_I} + \frac{1}{2} \sum_{i \neq j}^{NN} \frac{1}{|\mathbf{r}_i - \mathbf{r}_j|} \\ &+ \frac{1}{2} \sum_{I \neq J}^{MM} \frac{Z_I Z_J}{|\mathbf{R}_I - \mathbf{R}_J|} - \sum_{I,i}^{MN} \frac{Z_I}{|\mathbf{R}_I - \mathbf{r}_i|},\end{aligned} \tag{2.1}$$

which is composed of terms for the kinetic energy of the electrons, kinetic energy of the nuclei, electron-electron interaction, nucleus-nucleus interaction, and electron-nucleus interaction, respectively. In (2.1), m_e and M_I respectively refer to electron mass and the Ith nuclear mass, Z_I indicates atomic number, while $\mathbf{r}_i$ and $\mathbf{R}_i$ refer to the ith electron coordinate and nuclear coordinate, respectively. In the summations in the above equation, N is the total number of electrons and M (not to be confused with nuclear mass M_I) is the total number of nuclei in the system. The wave function Ψ that is the solution to the Schrödinger equation

$$\hat{H}\Psi(\mathbf{r}_1, \ldots, \mathbf{r}_N, \mathbf{R}_1, \ldots \mathbf{R}_M) = E\Psi(\mathbf{r}_1, \mathbf{r}_2, \ldots, \mathbf{r}_N, \mathbf{R}_1, \ldots \mathbf{R}_M) \tag{2.2}$$

thus depends on the N electronic coordinates $\mathbf{r}_i$ and the M nuclear coordinates $\mathbf{R}_I$ of the many-body system.

A first-step simplification is achieved via the Born-Oppenheimer approximation [92, 93]. Since nuclei are much more massive than electrons, atomic nuclei are assumed to be frozen in place. This renders the nuclei in the Hamiltonian as constants and allows for the separation of nuclear and electron dynamics in calculations, making it possible to focus mainly on electrons within DFT.

Consequently, the many-body Hamiltonian reduces to the kinetic energy term for electrons, the electron-electron interaction term, and the term for the external potential, which includes the potential created by the nuclei, now seen as external to the electron system [91]:

$$\hat{H} = - \sum_{i}^{N} \frac{\boldsymbol{\nabla}_i^2}{2m_e} + \frac{1}{2} \sum_{i \neq j}^{NN} \frac{1}{|\mathbf{r}_i - \mathbf{r}_j|} + \sum_{i}^{N} v(\mathbf{r}_i), \tag{2.3}$$

Even with the nuclear coordinates taken out, however, the wave function is still dependent on $3N$ spatial variables, with N being the number of electrons in the system. The problem remains formidable to solve, growing in complexity with

the number of electrons.

2.1.1 Hohenberg-Kohn Theorem

The ground-state electron density, the probability of finding any electron in an N-electron system with any spin σ at position $\mathbf{r}$, is given by [78, 91]

$$n(\mathbf{r}) = N \sum_{\sigma,\sigma_2,\ldots,\sigma_N} \int d^3r_2 d^3r_3 \cdots d^3r_N |\Psi(\mathbf{r}, \mathbf{r}_2, \ldots, \mathbf{r}_N, \sigma, \ldots, \sigma_N)|^2. \tag{2.4}$$

In 1964, Pierre Hohenberg and Walter Kohn [94] devised a theorem that justifies the use of this ground-state electron density in place of the many-body electron wave function in determining physical observables. The Hohenberg-Kohn theorem establishes a one-to-one correspondence between $n(\mathbf{r})$ and the external potential $v(\mathbf{r})$, the term in the Hamiltonian (2.3) that specifies the system. The theorem proves that two potentials $v(\mathbf{r})$ and $v'(\mathbf{r})$ cannot generate the same ground-state electron density $n(\mathbf{r})$ if the potentials differ by more than some constant c: $v'(\mathbf{r}) \neq v(\mathbf{r}) + c$.

The proof by contradiction proceeds as follows [95]:

Let $n(\mathbf{r})$ be the ground-state density arising from external potential $v_1(\mathbf{r})$ associated with the ground-state wave function Φ_1 with ground-state energy E_1:

$$E_1 = \langle \Phi_1 | \hat{H}_1 | \Phi_1 \rangle = \int d^3r \, v_1(\mathbf{r}) n(\mathbf{r}) + \langle \Phi_1 | \hat{T} + \hat{W} | \Phi_1 \rangle , \tag{2.5}$$

where $\hat{T}$ and $\hat{W}$ are the kinetic and potential terms of the Hamiltonian, respectively. At the same time, let a different external potential $v_2(\mathbf{r}) \neq v_1(\mathbf{r}) + c$ generate the same density $n(\mathbf{r})(= n_1(\mathbf{r}) = n_2(\mathbf{r}))$ and be associated with a different ground-state $\Phi_2 \neq \Phi_1$ with ground-state energy E_2:

$$E_2 = \langle \Phi_2 | \hat{H}_2 | \Phi_2 \rangle = \int d^3r \, v_2(\mathbf{r}) n(\mathbf{r}) + \langle \Phi_2 | \hat{T} + \hat{W} | \Phi_2 \rangle . \tag{2.6}$$

Following the Rayleigh-Ritz minimisation principle,

$$\begin{aligned} E_1 < \langle \Phi_2 | H_1 | \Phi_2 \rangle &= \int d^3r \, v_1(\mathbf{r}) n(\mathbf{r}) + \langle \Phi_2 | \hat{T} + \hat{W} | \Phi_2 \rangle \\ &= E_2 + \int d^3r \, (v_1(\mathbf{r}) - v_2(\mathbf{r})) n(\mathbf{r}) \end{aligned} \tag{2.7}$$

and

$$\begin{aligned} E_2 < \langle \Phi_1 | \, H_2 \, | \Phi_1 \rangle &= \int d^3r \, v_2(\mathbf{r}) n(\mathbf{r}) + \langle \Phi_1 | \, \hat{T} + \hat{W} \, | \Phi_1 \rangle \\ &= E_1 + \int d^3r \, (v_2(\mathbf{r}) - v_1(\mathbf{r})) n(\mathbf{r}) \end{aligned} \tag{2.8}$$

Adding (2.7) and (2.8) yields the contradiction

$$E_1 + E_2 < E_2 + E_1, \tag{2.9}$$

invalidating the original assumption that the different potentials $v(\mathbf{r})$ and $v'(\mathbf{r})$ generate the same $n(\mathbf{r})$.

This one-to-one mapping renders the external potential a unique functional of the ground-state electron density ($v(\mathbf{r}) = v[n](\mathbf{r})$), which means the Hamiltonian and the wave function of the interacting system are themselves unique functionals of the ground-state electron density ($\hat{H} = \hat{H}[n](\mathbf{r}); \Psi = \Psi[n](\mathbf{r})$). In consequence, physical observables, directly or indirectly, become functionals of the ground-state electron density as well [78].

In addition, the Hohenberg-Kohn theorem states that the true ground-state density of the system is the electron density that minimises the total energy functional [95]

$$E_v[n] = \langle \Psi[n] | \, (\hat{T} + \hat{V} + \hat{W}) \, | \Psi[n] \rangle \, , \tag{2.10}$$

where $\hat{V}$ is the external potential term of the Hamiltonian (2.3). The ground-state electron density can thus be obtained via a variational approach.

However, minimisation of the total energy functional is not simple. The total energy functional can be rewritten as [95]

$$E_v[n] = F[n] + \int d^3r \, n(\mathbf{r}) v(\mathbf{r}), \tag{2.11}$$

showing that it is constituted by a universal part $F[n]$, which is determined by the kinetic ($\hat{T}$) and interaction ($\hat{W}$) terms of the Hamiltonian and is applicable to any system with the same number of electrons and with the same electron-electron interaction regardless of atomic composition. At the same time, it contains a part that is determined by the external potential $v(\mathbf{r})$. The external potential is made up of the potential generated by the nuclei of the atoms of the system as well as

potentials from any applied fields. Thus, in contrast to $F[n]$, the contribution to the total energy of the external potential is specific to the system. The problem is that while the external potential (and thus the external potential energy term) is known, the exact form of the universal functional is unknown [95].

2.1.2 Kohn-Sham Equations

Despite the enormous simplification achieved through the Hohenberg-Kohn theorem, the difficulties presented by the electron-electron interaction and the fact that the kinetic energy term is not readily expressible in terms of the electron density [78, 95] dimmed the prospect of the practical implementation of DFT.

Walter Kohn and Lu Jeu Sham [96] worked around these difficulties by introducing, in a paper published in 1965, an auxiliary non-interacting system of electrons described by [78]

$$\left(-\frac{\boldsymbol{\nabla}^2}{2} + v_s(\mathbf{r})\right)\varphi_j(\mathbf{r}) = \varepsilon_j\varphi_j(\mathbf{r}), \tag{2.12}$$

where $\varphi_j(\mathbf{r})$ are single-particle Kohn-Sham (KS) orbitals from which the ground-state density can be obtained by summing occupied states:

$$n(\mathbf{r}) = \sum_{j}^{\text{occ}} |\varphi_j(\mathbf{r})|^2, \tag{2.13}$$

The crucial concept is that the interacting system being investigated and its auxiliary non-interacting system (the Kohn-Sham system) give the same ground-state electronic density ($n_{KS}(\mathbf{r}) = n(\mathbf{r})$).

The effective potential for the non-interacting system is the Kohn-Sham potential [78, 97]

$$v_s(\mathbf{r}) = v(\mathbf{r}) + \int d^3r' \frac{n(\mathbf{r}')}{|\mathbf{r} - \mathbf{r}'|} + v_{xc}(\mathbf{r}), \tag{2.14}$$

whose first, second, and third terms are the external potential, the Hartree potential, and the exchange-correlation potential, respectively. Following from the Hohenberg-Kohn theorem, the ground-state electronic density $n(\mathbf{r})$ of the interacting system can be uniquely mapped to an effective potential $v_s(\mathbf{r})$, which is the Kohn-Sham potential.

In the Kohn-Sham approach, the total energy functional is rewritten as [78, 95, 97]

$$E_v[n] = T_s[n] + E_{ext}[n] + E_H[n] + E_{xc}[n], \tag{2.15}$$

so that the universal functional takes the form [95]

$$F[n] = T_s[n] + E_H[n] + E_{xc}[n]. \tag{2.16}$$

In (2.15) and (2.16), $E_{ext}[n]$ is the external potential energy, while $T_s[n]$ is the non-interacting kinetic energy obtained from the Kohn-Sham orbitals

$$T_s[n] = -\sum_{j=1}^{N} \int d^3r\, \varphi_j^*(\mathbf{r}) \left(-\frac{\boldsymbol{\nabla}^2}{2}\right) \varphi_j(\mathbf{r}) \tag{2.17}$$

and the Hartree energy $E_H[n]$ is given by

$$E_H[n] = \frac{1}{2} \int dr \int d^3r' \frac{n(\mathbf{r})n(\mathbf{r}')}{|\mathbf{r} - \mathbf{r}'|}. \tag{2.18}$$

The exchange-correlation functional $E_{xc}[n]$ contains all the corrections accounting for the difference between the electron-electron interaction energy and the Hartree energy and the difference between the interacting kinetic energy and the kinetic energy of the non-interacting system. $E_{xc}[n]$ is defined by the exchange-correlation potential $v_{xc}(\mathbf{r})$ [78, 95, 97]:

$$v_{xc}(\mathbf{r}) = \frac{\delta E_{xc}[n]}{\delta n(\mathbf{r})}. \tag{2.19}$$

Thus, $v_{xc}(\mathbf{r})$ is crucial to the accurate and realistic description of materials in DFT. It takes the burden of describing all interaction effects [95, 98] to ensure that the interacting system and its auxiliary non-interacting Kohn-Sham system have the same ground-state electron density ($n_{KS}(\mathbf{r}) = n(\mathbf{r})$).

Equations (2.12), (2.13), and (2.14) constitute the Kohn-Sham equations, which are solved self-consistently.

The Kohn-Sham approach facilitates the practical implementation of DFT by shoving all complexities of the interacting system into the exchange-correlation term. One obtains the electron density of the interactive system of interest by obtaining the electron density of an auxiliary non-interactive system that is much easier to solve. Given an exact $v_{xc}(\mathbf{r})$, the ground-state electron density of the non-interacting system exactly matches that of the interacting many-body system. In practice, however, the exchange-correlation potential $v_{xc}(\mathbf{r})$ can only be

approximated [98–101].

2.2 Time-dependent density functional theory

In TDDFT, the electron density becomes a function of time as well ($n = n(\mathbf{r}, t)$) and it replaces the many-body time-dependent wave function that is a solution to the time-dependent Shrödinger equation

$$i\frac{\partial}{\partial t}\Psi(\mathbf{r}_1, \ldots \mathbf{r}_N, t) = \hat{H}(t)\Psi(\mathbf{r}_1, \ldots \mathbf{r}_N, t) \tag{2.20}$$

as the main quantity of interest.

TDDFT, however, is not a straightforward extension of ground-state DFT. TDDFT does not have a variational principle and initial states, and memory effects have to be taken into account, making the concept and implementation more complicated [78]. TDDFT has its own theorems that justify the use of the time-dependent electron density in place of the time-dependent wave function and the use a non-interacting system to obtain the electronic density of the interacting system. The proof and other details of these theorems (presented below) can be found in [78, 102, 103]. The following discussion is also based on these cited works.

The counterpart of the Hohenberg-Kohn theorem in TDDFT, the Runge-Gross theorem [104] establishes a one-to-one correspondence between the time-dependent external potential $v(\mathbf{r}, t)$ and the time-dependent electron density $n(\mathbf{r}, t)$. The crux of the theorem is that time-dependent electron densities $n(\mathbf{r}, t)$ and $n'(\mathbf{r}, t)$, which evolve from the same initial state ($\Psi(\mathbf{r}, t_0) = \Psi'(\mathbf{r}, t_0)$), will be different from each other starting at $t > t_0$ if the potentials $v(\mathbf{r}, t)$ and $v'(\mathbf{r}, t)$ that generate them are different by more than a purely time-dependent function $c(t)$ ($v'(\mathbf{r}, t) \neq v(\mathbf{r}, t) + c(t)$). The potentials must also be Taylor-expandable around the initial time $t = t_0$:

$$v(\mathbf{r}, t) = \sum_{k=0}^{\infty} \frac{1}{k!} v_k(\mathbf{r})(t - t_0)^k. \tag{2.21}$$

According to the van Leeuwen theorem [105], for a system with interaction $w(|\mathbf{r} - \mathbf{r}'|)$, potential $v(\mathbf{r}, t)$ and initial state $\Psi(\mathbf{r}, t_0)$, there exists a second system with interaction $w'(|\mathbf{r} - \mathbf{r}'|)$ and unique potential $v'(\mathbf{r}, t)$ ($v'(\mathbf{r}, t) \neq v(\mathbf{r}, t) + c(t)$) that produces the same time-dependent electron density as the first system ($n'(\mathbf{r}, t) = n(\mathbf{r}, t)$). Such is the case as long as the initial state of the second system $\Psi'(\mathbf{r}, t_0)$ is chosen so that it generates the first system's electronic density and its

time derivative at t_0.

If the second system referred to in the van Leeuwen theorem is non-interacting ($w' = 0$), the van Leeuwen theorem ensures that there is a unique potential $v_s(\mathbf{r}, t)$ such that the non-interacting system yields the electron density $n(\mathbf{r}, t)$ of the interacting system, with the assumption that the non-interacting and interacting systems have the same initial density and time-derivative of the initial density. This allows the use of the time-dependent Kohn-Sham scheme in TDDFT.

2.2.1 Time-dependent Kohn-Sham scheme

Given the Runge-Gross and van Leeuwen theorems, it is possible to set up a time-dependent Kohn-Sham (TDKS) system of non-interacting electrons under the influence of the TDKS potential [78]

$$v_s[n, \Psi_0, \Phi_0](\mathbf{r}, t), \tag{2.22}$$

which is a functional of the time-dependent density, the initial state of the interacting system Ψ_0, and the initial Kohn-Sham state Φ_0. This effective potential governs the dynamics of the system for $t > t_0$ through the equation [78, 103]

$$\left[-\frac{\boldsymbol{\nabla}^2}{2} + v_s[n](\mathbf{r}, t)\right] \varphi_j(\mathbf{r}, t) = i\frac{\partial}{\partial t}\varphi_j(\mathbf{r}, t) \tag{2.23}$$

with initial condition

$$\varphi_j(\mathbf{r}, t_0) = \varphi_j^0(\mathbf{r}), \tag{2.24}$$

where $\varphi_j^0(\mathbf{r})$ are solutions to the KS equations of ground-state DFT. The time-dependent KS orbitals can then be used to construct the time-dependent density

$$n(\mathbf{r}, t) = \sum_{j=1}^{N} |\varphi_j(\mathbf{r}, t)|^2. \tag{2.25}$$

The TDKS potential (2.22) is given by [78, 103]

$$v_s[n](\mathbf{r}, t) = v(\mathbf{r}, t) + \int d^3r' \frac{n(\mathbf{r}', t)}{|\mathbf{r} - \mathbf{r}'|} + v_{xc}[n, \Psi_0, \Phi_0](\mathbf{r}, t), \tag{2.26}$$

where the first, second, and third terms on the right-hand side are the time-dependent external potential, the time-dependent Hartree potential, and the time-dependent xc potential, respectively. As in the ground-state case, $v_{xc}(\mathbf{r}, t)$ is unknown in its exact form and must therefore be approximated [78, 103].

A commonly used approximation is the adiabatic approximation, where one simply takes the xc potential of ground-state DFT ($v_{xc}[n](\mathbf{r})$) and use it in the TDKS equation (2.23) but with the time-dependent density $n(\mathbf{r}, t)$ plugged in instead of the ground-state density $n(\mathbf{r})$ [78, 103]:

$$v_{xc}^{A}(\mathbf{r}, t) = v_{xc}[n](\mathbf{r})\Big|_{n(\mathbf{r})\to n(\mathbf{r},t)}. \tag{2.27}$$

In TDDFT, the adiabatic local density approximation (ALDA) [102], where the local density approximation (LDA) functional [106] of ground-state DFT is used in (2.27), is the one that is most widely implemented. The LDA itself is a homogeneous electron gas approximation of $v_{xc}(\mathbf{r})$. In the LDA, at every point $\mathbf{r}$, the known exchange-correlation potenial of the homogenous electron gas at that point is used [78, 103]:

$$v_{xc}^{LDA}(\mathbf{r}) = \frac{de_{xc}^{h}(\overline{n})}{d\overline{n}}\Big|_{\overline{n}=n(\mathbf{r})}, \tag{2.28}$$

where $e_{xc}^{h}(n)$ is the exchange-correlation energy density of the homogeneous electron gas.

CHAPTER

THREE

LINEAR RESPONSE THEORY

In spectroscopy experiments, materials are probed by applying fields whose strength is enough to generate a response but not strong enough to interfere with the property one wants to measure. Collective excitations can be described as responses to a weak perturbation [52, 107]. As such, they usually fall within the ambit of linear response theory.

3.1 General concepts

This section follows the discussion found in [52, 78]. When a perturbing field $F(t)$ couples to an observable $\hat{B}$ of a system, the Hamiltonian of the system under perturbation can be written as

$$\hat{H}(t) = \hat{H}_0 + F(t)\hat{B}, \tag{3.1}$$

where $\hat{H}_0$ is the Hamiltonian of the system before perturbation and $F(t)$ is taken to vanish for times before some initial time. Under the influence of the perturbation, the ground-state expectation value of another observable $\hat{A}$ of the system

$$\langle \hat{A} \rangle_0 = \langle \Psi_0 | \, \hat{A} \, | \Psi_0 \rangle \, , \tag{3.2}$$

with $|\Psi_0\rangle$ as the ground state of $\hat{H}_0$ with energy E_0, becomes time-dependent:

$$\langle \hat{A} \rangle(t) = \langle \Psi(t) | \, \hat{A} \, | \Psi(t) \rangle \, . \tag{3.3}$$

When the perturbation is weak, the response of the system ($\delta\langle \hat{A} \rangle(t)$) is linear:

$$\begin{aligned}\delta\langle\hat{A}\rangle(t) &= \langle\hat{A}\rangle(t) - \langle\hat{A}\rangle_0 \\ &= \int_0^\infty dt'\, \chi_{AB}(t-t')F(t'),\end{aligned} \tag{3.4}$$

and characterised by the linear response function $\chi_{AB}(t-t')$ given by the Kubo formula

$$\chi_{AB}(t-t') \equiv -\frac{i}{\hbar}\Theta(t-t')\left\langle\left[\hat{A}(t-t'),\hat{B}\right]\right\rangle_0. \tag{3.5}$$

The step function $\Theta(t-t')$ ensures that the expression is non-zero only when $t > t'$ and encapsulates causality, meaning the response at time t is an effect of the perturbation that coupled to the system at an earlier time t'.

The poles of the response function give the excitation energies of the system. This can be easily seen in the Lehmann representation of the response function:

$$\begin{aligned}\chi(\mathbf{r},\mathbf{r}',\omega) = \lim_{\eta\to 0^+}\frac{1}{\hbar}\sum_n\Bigg[&\frac{\langle\Psi_0|\,\hat{n}(\mathbf{r})\,|\Psi_n\rangle\,\langle\Psi_n|\,\hat{n}(\mathbf{r}')\,|\Psi_0\rangle}{\omega+\Omega_n+i\eta} \\ &-\frac{\langle\Psi_0|\,\hat{n}(\mathbf{r}')\,|\Psi_n\rangle\,\langle\Psi_n|\,\hat{n}(\mathbf{r})\,|\Psi_0\rangle}{\omega-\Omega_n+i\eta}\Bigg],\end{aligned} \tag{3.6}$$

which defines the response function in terms of the system ground state $|\Psi_0\rangle$. In (3.6), $\hat{n}(\mathbf{r})$ is the density operator, the states of the system are denoted by $|\Psi_n\rangle$, and Ω_n are excitation frequencies that define the excitation energies $E_n - E_0$, where E_0 is ground- or equilibrium-state energy.

3.2 Linear response in TDDFT

Here, the presentation of the basic concepts of linear response theory follows the discussions in [102, 108, 109]. If a system, which ground-state DFT can describe, is placed under the influence of a time-dependent external potential that is a sum of non-pertubed ($v_0(\mathbf{r})$) and perturbative parts

$$v(\mathbf{r},t) = v_0(\mathbf{r}) + v_1(\mathbf{r},t)\Theta(t-t_0) \tag{3.7}$$

and the perturbation $v_1(\mathbf{r},t)$ is small, the linear response of the density of the system can be expressed as

$$n_1(\mathbf{r},t) = \int_0^\infty dt' \int d^3r'\, \chi(\mathbf{r},t,\mathbf{r}',t') v_1(\mathbf{r}',t'). \tag{3.8}$$

In this case, $\chi(\mathbf{r},t,\mathbf{r}',t')$ is the density-density response function given by the Kubo formula

$$\chi(\mathbf{r},t,\mathbf{r}',t') = -\frac{i}{\hbar}\Theta(t-t') \left\langle [\hat{n}(\mathbf{r},t), \hat{n}(\mathbf{r}',t')] \right\rangle_0 . \tag{3.9}$$

It describes the response of the density at position $\mathbf{r}$ at time t to the perturbation that coupled to the density at another point $\mathbf{r}'$ at an earlier time t'. From the Taylor expansion of the density response, one finds that the density-density function also corresponds to the expression

$$\chi(\mathbf{r},t,\mathbf{r}',t') = \left. \frac{\delta n[v](\mathbf{r},t)}{\delta v(\mathbf{r}',t')} \right|_{v_0(\mathbf{r})} \tag{3.10}$$

evaluated at the initial potential $v_0(\mathbf{r})$.

The fundamental theorems of TDDFT ensure that the density response of the fully interacting system is the same as that of the non-interacting system in the Kohn-Sham approach. The linear response of the density is expressed in the Kohn-Sham scheme as

$$n_1(\mathbf{r},t) = \int_0^\infty dt' \int d^3r'\, \chi_s(\mathbf{r},t,\mathbf{r}',t') v_{1s}(\mathbf{r}',t'), \tag{3.11}$$

where the non-interacting Kohn-Sham linear density-density response function has the form

$$\chi_s(\mathbf{r},t,\mathbf{r}',t) = \left. \frac{\delta n[v_s](\mathbf{r},t)}{\delta v_s(\mathbf{r}',t')} \right|_{v_s[n](\mathbf{r})}, \tag{3.12}$$

with $v_s(\mathbf{r},t)$ denoting the effective Kohn-Sham potential discussed in the previous chapter. The potential acting on this system of non-interacting electrons is the linearised Kohn-Sham potential

$$v_{1s}[n](\mathbf{r},t) = v_1(\mathbf{r},t) + \int d^3r' \frac{n_1(\mathbf{r}',t)}{|\mathbf{r}-\mathbf{r}'|} + v_{1xc}(\mathbf{r},t), \tag{3.13}$$

where the first, second, and third terms are the linearised external potential, the linearised Hartree potential, and the linearised xc potential, respectively. The linearised xc potential is given by

$$v_{1xc}(\mathbf{r},t) = \int_0^\infty dt' \int d^3r' \left. \frac{\delta v_{xc}[n](\mathbf{r},t)}{\delta n(\mathbf{r}',t')} \right|_{n(\mathbf{r})} n_1(\mathbf{r}',t'), \tag{3.14}$$

evaluated at the ground-state density $n(\mathbf{r})$. The expression in (3.14) defines the exchange-correlation kernel f_{xc}:

$$f_{xc}(\mathbf{r},t,\mathbf{r}',t') = \left.\frac{\delta v_{xc}[n](\mathbf{r},t)}{\delta n(\mathbf{r}',t')}\right|_{n(\mathbf{r})}. \tag{3.15}$$

The relation between the interacting and non-interacting Kohn-Sham density-density response functions are given by a Dyson-like equation:

$$\begin{aligned}\chi(\mathbf{r},t,\mathbf{r}',t) = \chi_s(\mathbf{r},t,\mathbf{r}',t') \int dt_1 \int d^3r_1 \int dt_2 \int d^3r_2\, \chi_s(\mathbf{r},t,\mathbf{r}_1,t_1) \\ \cdot \left[\frac{\delta(t_1-t_2)}{|\mathbf{r}_1-\mathbf{r}_2|} + f_{xc}(\mathbf{r}_1,t_1,\mathbf{r}_2,t_2)\right] \chi_(\mathbf{r}_2,t_2,\mathbf{r}',t').\end{aligned} \tag{3.16}$$

3.3 Response function

In linear response TDDFT, plasmons are described as the response of the charge density of the system to an external scalar potential ($\delta n/\delta v_{ext}$), while magnons are described as the response of the magnetisation density of the system to an external magnetic field ($\delta\mathbf{m}/\delta\mathbf{B}_{ext}$) [110].

The magnetisation density is defined as the difference between the spin-up and spin-down polarised densities [69]:

$$\mathbf{m}(\mathbf{r},t) = n_\uparrow(\mathbf{r},t) - n_\downarrow(\mathbf{r},t), \tag{3.17}$$

where the axis of quantisation is taken to be the z-axis and the spin-polarised density is obtained from the spin-polarised Kohn-Sham orbitals [102]:

$$n_\sigma(\mathbf{r},t) = \sum_{\sigma=\uparrow,\downarrow} \sum_{j=1} |\varphi_{j\sigma}(\mathbf{r},t)|^2. \tag{3.18}$$

The system Hamiltonian takes the form [111]

$$\hat{H} = \hat{H}_0 + \sum_\mu \int d^3r\, \hat{\rho}^\mu(\mathbf{r}) V^\mu_{ext}(\mathbf{r},t), \tag{3.19}$$

where $\hat{\rho}^\mu$ is the four-component density operator that gives the four-component density $\rho(\mathbf{r}) = [n(\mathbf{r}), \mathbf{m}(\mathbf{r})]$ composed of the electron density and the magnetisation density. The magnetisation density is constituted by Cartesian components $m_x(\mathbf{r}), m_y(\mathbf{r}), m_z(\mathbf{r})$ and the perturbing field is composed of the scalar external potential and the external magnetic field [110, 111]:

$$V_{ext}(\mathbf{r},t) = [v_{ext}(\mathbf{r},t), \mathbf{B}_{ext}(\mathbf{r},t)]. \tag{3.20}$$

The response of the four-component density can then be expressed as [111, 112]

$$\delta\rho^{\mu}(\mathbf{r},t) = \sum_{\nu} \int dt' \int d^3r\, \chi^{\mu\nu}(\mathbf{r},\mathbf{r}',t-t') V^{\nu}_{ext}(\mathbf{r}',t'), \tag{3.21}$$

characterised by the response function [110, 112]

$$\chi^{\mu\nu}(\mathbf{r},\mathbf{r}',t,t') = \frac{\delta\rho^{\mu}(\mathbf{r},t)}{\delta V^{\nu}_{ext}(\mathbf{r}',t')}, \tag{3.22}$$

which is also given by the Kubo formula [111]

$$\chi^{\mu\nu}(\mathbf{r},\mathbf{r}',t,t') = -\frac{i}{\hbar}\Theta(t-t') \left\langle [\hat{\rho}^{\mu}(\mathbf{r},t), \hat{\rho}^{\nu}(\mathbf{r}',t')] \right\rangle_0 . \tag{3.23}$$

The response function is a tensor. χ^{00} corresponds to charge-charge response ($\delta n/\delta v_{ext}$), $\chi^{01,02,03}$ describe the charge-spin response ($\delta n/\delta \mathbf{B}_{ext}$), $\chi^{10,20,30}$ give the spin-charge response ($\delta \mathbf{m}/\delta v_{ext}$), and $\chi^{11-13,21-23,31-33}$ characterise the spin-spin response ($\delta \mathbf{m}/\delta \mathbf{B}_{ext}$) [110].

In the Kohn-Sham scheme of TDDFT, the response function of the interacting system is related to the Kohn-Sham response function $\chi^{\mu\nu}_s(\mathbf{r},\mathbf{r}',\omega)$ by a Dyson-like equation [110]

$$\begin{aligned} \chi^{\mu\nu}(\mathbf{r},\mathbf{r}',\omega) =& \chi^{\mu\nu}_s(\mathbf{r},\mathbf{r}',\omega) + \int d^3r'' \int d^3r''' \chi^{\mu\delta}_s(\mathbf{r},\mathbf{r}'',\omega) \\ & [f^{\delta\gamma}_H(\mathbf{r}'',\mathbf{r}''') + f^{\delta\gamma}_{xc}(\mathbf{r}'',\mathbf{r}''',\omega)] \chi^{\gamma\nu}(\mathbf{r}''',\mathbf{r}',\omega), \end{aligned} \tag{3.24}$$

with the Hartree kernel given by $f^{\mu\nu}_H(\mathbf{r},\mathbf{r}') = \delta^{\mu 0}\delta^{\nu 0}(1/|\mathbf{r}-\mathbf{r}'|)$ and $f^{\mu\nu}_{xc}(\mathbf{r},\mathbf{r}',\omega)$ is the Fourier transform of the xc kernel [110]

$$f^{\mu\nu}_{xc}(\mathbf{r},\mathbf{r}',t,t') = \frac{\delta V^{\mu}_{xc}(\mathbf{r},t)}{\delta\rho^{\nu}(\mathbf{r}',t')}, \tag{3.25}$$

where V^{μ}_{xc} is composed of the scalar xc potential $v_{xc}(\mathbf{r},t)$ and the xc magnetic field $\mathbf{B}_{xc}(\mathbf{r},t)$. The non-interacting Kohn-Sham response function, in the Lehmann representation, is given by [110, 113]

$$\chi^{\mu\nu}_s(\mathbf{r},\mathbf{r}',\omega) = \lim_{\eta\to 0^+} \sum_{\kappa,\xi} \sigma^{\mu}\sigma^{\nu}(f_\kappa - f_\xi) \frac{\phi^*_\kappa(\mathbf{r})\phi_\xi(\mathbf{r})\phi_\kappa(\mathbf{r}')\phi^*_\xi(\mathbf{r}')}{\hbar\omega + (\varepsilon_\kappa - \varepsilon_\xi) + i\hbar\eta}, \tag{3.26}$$

where $\phi(\mathbf{r})$ are Kohn-Sham spinors indexed by κ and ξ, each of which is a combined

band and state index. In (3.26), f_κ and f_ξ are Kohn-Sham occupation numbers and $\sigma^\mu = [\mathbb{1}, \sigma^{x,y,z}]$ can denote the identity matrix $\mathbb{1}$ or the Pauli matrices $\sigma^{x,y,z}$.

When working with periodic systems, the Fourier transform of the response function is often used [110]:

$$\chi^{\mu\nu}_{\mathbf{G}\mathbf{G}'}(\mathbf{q},\omega) = \int d^3r \int d^3r'\, e^{-i(\mathbf{q}+\mathbf{G})\cdot\mathbf{r}} \chi^{\mu\nu}(\mathbf{r},\mathbf{r}',\omega) e^{i(\mathbf{q}+\mathbf{G}')\cdot\mathbf{r}'}, \tag{3.27}$$

with $\mathbf{q}$ as the wave vector of the perturbation and $\mathbf{G}, \mathbf{G}'$ denoting reciprocal lattice vectors.

3.3.1 Plasmons

The charge-charge component of the response function in (3.27) is used to obtain the plasmon energies. It defines the microscopic dielectric function for a periodic system [59, 78, 110]:

$$\varepsilon^{-1}_{\mathbf{G},\mathbf{G}'}(\mathbf{q},\omega) = \delta_{\mathbf{G},\mathbf{G}'} + v(q)\chi^{00}_{\mathbf{G},\mathbf{G}'}(\mathbf{q},\omega), \tag{3.28}$$

with $v(q)$ being the Coulomb potential in wave-vector space. The microscopic dielectric function is then used to obtain the macroscopic response function [59, 78, 107]

$$\varepsilon_M(\mathbf{q}\omega) = \frac{1}{\varepsilon^{-1}_{\mathbf{G},\mathbf{G}'}(\mathbf{q},\omega)\big|_{\mathbf{G}=\mathbf{G}'=0}}, \tag{3.29}$$

which corresponds to experimental measurements. The loss function that gives the EEL spectra is given by [59, 114]

$$-\mathrm{Im}\left[\varepsilon^{-1}_M(\mathbf{q},\omega)\right]. \tag{3.30}$$

A peak in the spectra for which $\mathrm{Re}(\varepsilon_M) = 0$ and $\mathrm{Im}(\varepsilon_M)$ is small indicates a plasmon [61]. $\mathrm{Im}(\varepsilon_M)$ characterises damping and absorption of electromagnetic waves [114].

For the rest of this section, the superscript is omitted in χ^{00}, with the understanding that χ refers to the charge-charge part of the response function. In general, the interacting response function takes the form

$$\chi(\mathbf{q},\omega) = \frac{\chi_0(\mathbf{q},\omega)}{1 - [v(q) + f_{xc}(q,\omega)]\chi_0(\mathbf{q},\omega)}, \tag{3.31}$$

where $f_{xc}(q,\omega)$ is the response kernel, $v(q)$ is the Coulomb interaction, and $\chi_0(\mathbf{q},\omega)$

is the Lindhard function. The Lindhard function is the density-density response function of the non-interacting electron gas system [51, 52].

The conditions for identifying a plasmon — $\mathrm{Re}(\varepsilon_M) = 0$ and a small value of $\mathrm{Im}(\varepsilon_M)$ — can be appreciated by considering the expressions for the dielectric function and the response function in the random-phase approximation (RPA). In the RPA, for which $f_{xc} = 0$ [52], the dielectric response function is expressed as [51, 52]

$$\varepsilon^{RPA}(\mathbf{q}, \omega) = 1 - v(q)\chi_0(a, \omega) \tag{3.32}$$

and the interacting response function is given by [51, 52]

$$\chi(q, \omega) = \frac{\chi_0(q, \omega)}{1 - v(q)\chi_0(q, \omega)}. \tag{3.33}$$

From the fluctuation-dissipation theorem [52, 78], which states that the fluctuation of the density is directly proportional of the dissipation described by the imaginary part of the response function, the density fluctuation spectrum of an interacting electron gas is given by [52]

$$\mathrm{Im}(\chi(\mathbf{q}, \omega)) = \frac{\mathrm{Im}(\chi_0(\mathbf{q}, \omega))}{[1 - v(q)\mathrm{Re}(\chi_0(\mathbf{q}, \omega))]^2 + [\mathrm{Im}(\chi_0(\mathbf{q}, \omega))]^2}. \tag{3.34}$$

This expression gives the shape of a Lorentzian distribution. The numerator and the second term in the denominator both correspond to $\mathrm{Im}(\varepsilon^{RPA})$, while the first term of the denominator corresponds to $\mathrm{Re}(\varepsilon^{RPA})$. The expression gives a well-defined peak when $\mathrm{Im}(\varepsilon^{RPA}) \approx 0$ and $\mathrm{Re}(\varepsilon^{RPA}) = 0$.

In addition, the numerator, which is the imaginary part of the Lindhard response function, describes the dissipation of the non-interacting electron gas, whose excitations are single-particle rather than collective [51, 52]. Thus, the values in the $(\mathbf{q}, \omega)$ plane for which $\mathrm{Im}(\chi_0(\mathbf{q}, \omega))$ is non-zero defines the electron-hole continuum of single-particle excitations. One then sees that within regions where $\mathrm{Im}(\varepsilon^{RPA})$ is considerable, collective excitations experience Landau damping and decay into electron-hole pairs. The shape of the theory-predicted electron-hole continuum [51, 52] is illustrated in Figure 1.2.2 in the Introduction.

3.3.2 Magnons

The transverse spin-spin response function $\chi^{+-}(\mathbf{q}, \omega)$ [52, 113, 115] describes the response of the magnetisation density to an external magnetic field oriented perpendicular to the direction of spin polarisation of the ground-state system [111,

115]:

$$\delta m_+(\mathbf{r},t) = \int dt' \int d\mathbf{r}'\, \chi^{+-}(\mathbf{r},\mathbf{r}',t-t')B_+(\mathbf{r}',t'). \tag{3.35}$$

In the above equation, the transverse magnetisation density is given by $m_+ = m_x(\mathbf{r}) + im_y(\mathbf{r})$ and the transverse magnetic field is given by $B_+ = B_x(\mathbf{r}) + iB_y(\mathbf{r})$. $m_x(\mathbf{r}), m_y(\mathbf{r})$ and $B_x(\mathbf{r}), B_y(\mathbf{r})$ are the x and y components of the magnetisation density and the applied magnetic field, respectively.

In the collinear case, the spin-spin part of the response function in (3.22) becomes block diagonal, decoupling the transverse spin-spin response from the longitudinal spin-spin response χ^{zz} and the charge-charge response χ^{00} [73, 111]. The transverse components of the spin-spin response function are then given by [52, 110]:

$$\begin{aligned} \chi^{+-} &= \chi^{S^+S^-} = 2\chi^{xx} + 2i\chi^{xy} \\ \chi^{-+} &= \chi^{S^-S^+} = 2\chi^{xx} - 2i\chi^{xy}, \end{aligned} \tag{3.36}$$

In the indices above, $S^\pm$ refer to spin ladder operators defined as $\hat{S}^\pm = \hat{S}^x \pm i\hat{S}^y$, with $\hat{S}^x$ and $\hat{S}^y$ being spin components in the x and y directions, respectively.

In inelastic neutron scattering experiments, information about magnons are obtained from the neutron scattering cross section (1.13), which is proportional to the imaginary part of the transverse response function [77, 112, 115]. Thus, in linear-response TDDFT computations, magnon energies are obtained from the peaks of $\mathrm{Im}(\chi^{+-}(\mathbf{q},\omega))$ [110, 112, 115].

CHAPTER

FOUR

COMPUTATIONAL DETAILS

All ground-state and TDDFT calculations were done using the all-electron full-potential linearised augmented plane-wave (FP-LAPW) code Elk [116]. To approximate the exchange-correlation energy, the local density approximation (LDA) was used for the ground-state calculations, while the TDDFT calculations made use of the adiabatic local density approximation (ALDA).

4.1 Bulk and monolayer cells

Two structures, bulk and monolayer, are considered in this work. To capture the material's antiferromagnetic character, the bulk structure (image on the left in Figure 4.1.1) is modelled using a cell that is double the unit cell of FeSn along the c-direction. The slab model for the monolayer (image on the right in Figure 4.1.1), on the other hand, consists of two Fe_3Sn layers and three Sn layers to preserve symmetry and the material's antiferromagnetic character. Note that in both cells illustrated in Figure 4.1.1, the top layer is merely a periodic repetition of the bottom layer. Both structures were based on experimental lattice constants [117]. For both, the in-plane lattice parameters used were $a = b = 5.297$ Å. In the bulk, the out-of-plane lattice parameter used was $c = 8.96$ Å, which is double the experimental value of $c = 4.48$ Å of the FeSn unit cell. In the slab structure, a 20-Å vacuum layer was added to ensure the separation of periodic slabs. In both cases, atomic positions were relaxed prior to TDDFT calculations.

The spins of the Fe atoms of FeSn are in-plane, pointing along the a-axis of the crystal ([100] direction) [34, 118]. The material is ferromagnetic in each kagome plane, but neighbouring kagome planes are antiferromagnetic. The calculated magnetic moment of Fe was 1.85 μ_B for the bulk and and 1.96 μ_B for the slab.

For both structures, the obtained net magnetic moment was zero. In Elk, as is standard in many DFT codes, collinear calculations can only be performed if spins point along the Cartesian z-direction which, by convention, is the $c-$axis. Since collinearity is assumed in the computation of the transverse magnetic response function (χ^{+-}) in Elk, the bulk and slab FeSn structures were rotated so that their spins pointed along the z-direction for magnon calculations. Spin-orbit coupling is not considered in this thesis.

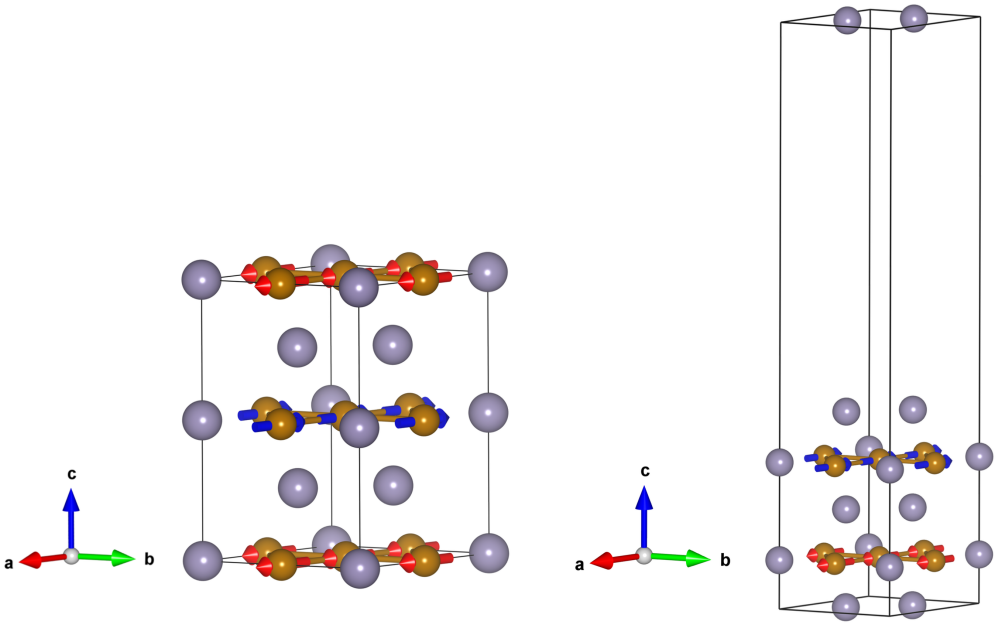

Figure 4.1.1: The bulk (left) and monolayer slab (right) structures of FeSn. Brown and grey spheres represent Fe and Sn, respectively. The orientation of spins are also shown. Note that in each cell, the top layer is merely a periodic repetition of the bottom layer.

The calculated electronic band structures of paramagnetic bulk and monolayer FeSn as well as their antiferromagnetic (AFM) counterparts are shown in Figure 4.1.2. The electronic band structure obtained for bulk AFM FeSn is in agreement with results from previous DFT studies [30, 34]. DFT-obtained band structures for the paramagnetic case (bulk and monolayer) as well as for the AFM monolayer have not been reported previously.

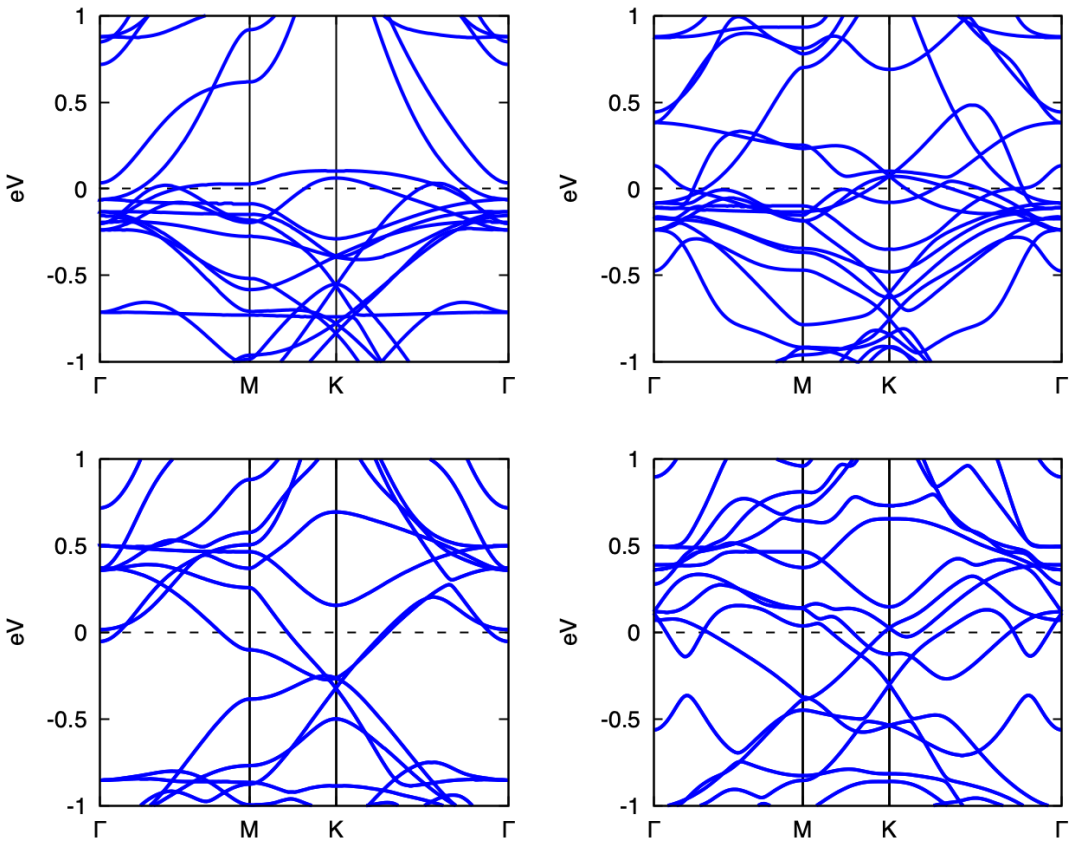

Figure 4.1.2: Calculated electronic band structure for paramagnetic bulk (top left), paramagnetic monolayer (top right), AFM bulk (bottom left), and AFM monolayer (bottom right) FeSn.

4.2 Computational parameters

Convergence tests were performed to obtain the optimal values for relevant parameters used in the ground-state and TDDFT calculations in Elk. These parameters are discussed below. The results obtained from calculations for plasmons and magnons performed in Elk using these parameters are presented and discussed in the next two chapters.

4.2.1 Plasmon calculations

The plasmon calculations for the bulk and slab structures used the same values except for the size of the k-point mesh. The energy cut-off (parameter `emaxrf`) used to limit the summation over states in the calculation of the Kohn-Sham response function (see (3.26)) was 2 Hartree. This represents an energy window above and below the Fermi energy ε_F: $|\varepsilon_\xi - \varepsilon_F| < 2$ Hartree. The maximum length of $\mathbf{G}$

vectors used in the calculation of the response function (see (3.27) and (3.29)) as a matrix in $\mathbf{G}, \mathbf{G}'$ was 1.8 Bohr^{-1}. This value, set by the parameter `gmaxrf`, is converged for the bulk. For the slab, however, it was a value settled for, as calculations beyond it would not complete due to computational expense. For the expansion of the interstitial density and potential, a $\mathbf{G}$ vector maximum length (parameter `gmaxvr`) of 11.0 Bohr^{-1} was used, while the value of $R^{MT} \times \texttt{max}(|\mathbf{G}+\mathbf{k}|)$ (parameter `rgkmax`) used in the expansion of plane waves in the LAPW basis was set to 7.0. R^{MT} refers to the radius of the muffin tins, which are the spherical regions used in the LAPW method [119]. The Brillouin zone was sampled using k-point meshes of size $16 \times 16 \times 8$ and $16 \times 16 \times 1$ for the bulk and slab, respectively.

4.2.2 Magnon calculations

For magnon calculations, the response functions were calculated using a converged energy cut-off parameter of 1.5 Hartree and 0.6 Hartree for the bulk and slab, respectively. The matrix expansion of the response functions used a $\mathbf{G}$ vector maximum length of 1.1 Bohr^{-1} for the bulk and 1.6 Bohr^{-1} for the slab. These values for the maximum $\mathbf{G}$ vector, set via parameter `gmaxrf`, are not converged, as calculations with higher values would not complete due to a large demand on computational resources. For both structures, a maximum $\mathbf{G}$ vector length of 12.0 Bohr^{-1} was used for the expansion of the interstitial density and potential, while the value of $R^{MT} \times \texttt{max}(|\mathbf{G} + \mathbf{k}|)$ was set to 8.5 and 8.0 for the bulk and slab, respectively. The k-point mesh used in the sampling of the Brillouin zone was $12 \times 12 \times 6$ for the bulk and $12 \times 12 \times 1$ for the slab. As mentioned in the discussion of the structures, the bulk and monolayer cells had to be rotated to obtain the transverse spin-spin response function within Elk.

CHAPTER

FIVE

PLASMONS IN BULK AND MONOLAYER FeSn

5.1 Dielectric function

This chapter begins with a brief description of the dielectric function $\varepsilon(\mathbf{q}, \omega)$ of FeSn. The dielectric function, which in general is a function of wave vector $\mathbf{q}$ and frequency ω, describes the response of a material to external electric fields and electromagnetic waves [33]. As such, it is a key quantity used to characterise a material's electronic and optical properties.

As defined in terms of the electric displacement field $\mathbf{D} = \varepsilon\mathbf{E}$, it determines the polarisation of charges in a material that is subjected to an external electric field $\mathbf{E}$. In addition, it is related to electrical conductivity $\sigma(\omega)$ via the relation [33]

$$\varepsilon(\omega) = 1 - i4\pi\sigma(\omega)/\omega. \tag{5.1}$$

With regard to optical response, the complex dielectric function $\varepsilon = \mathrm{Re}(\varepsilon(\omega)) + i\mathrm{Im}(\varepsilon(\omega))$ is related to experimentally accessible properties. Its relation to the index of refraction $n(\omega)$ and extinction coefficient $\kappa(\omega)$, optical quantities obtainable from reflectivity measurements, is given by the complex refractive index [33]

$$N(\omega) = \sqrt{\varepsilon(\omega)} = n(\omega) + i\kappa(\omega). \tag{5.2}$$

The real and imaginary parts of the dielectric function can be obtained once $n(\omega)$ and $\kappa(\omega)$ have been determined since $\mathrm{Re}(\varepsilon(\omega)) = n^2(\omega) - \kappa^2(\omega)$ and $\mathrm{Im}(\varepsilon(\omega)) = 2n(\omega)\kappa(\omega)$ [33]. Moreover, since the absorption coefficient, the rate of the decay of light waves in a material, is given by $\alpha(\omega) = \omega\mathrm{Im}(\varepsilon)/n(\omega)c$, where c is the speed of light, the absorption spectrum of a material is also obtainable from the

dielectric function [33].

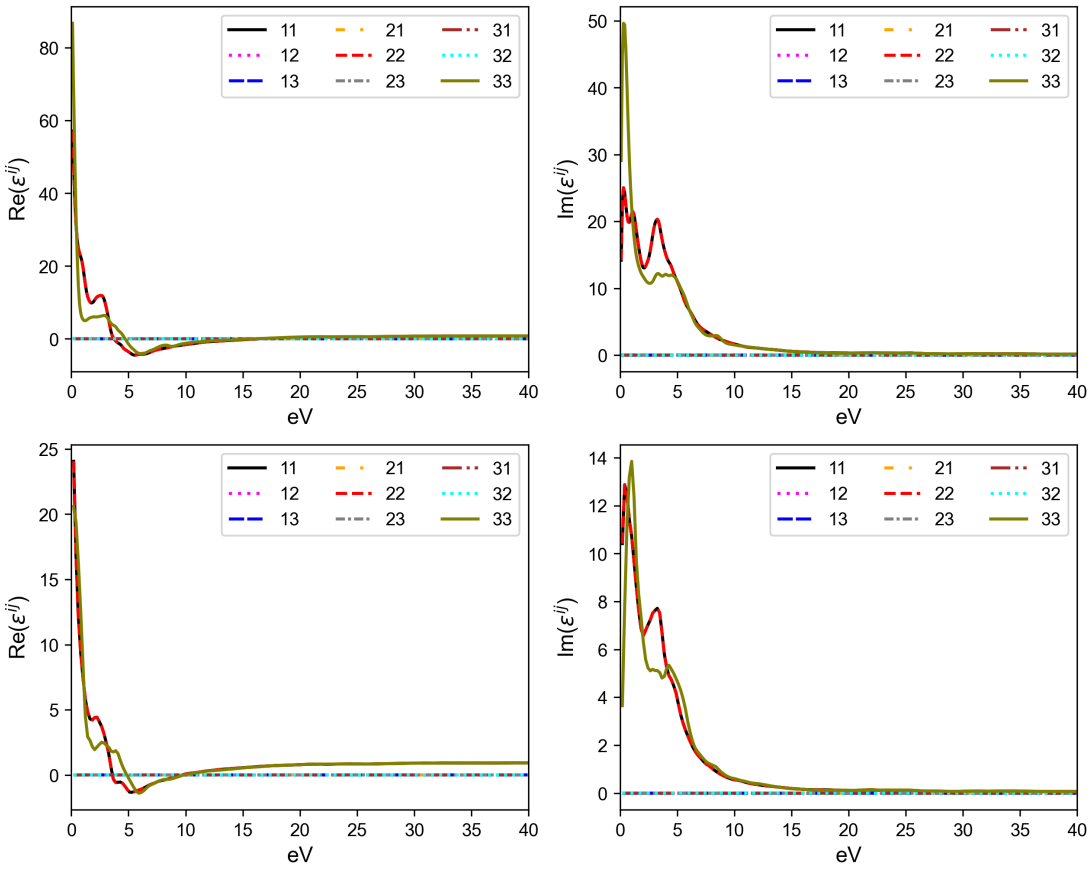

Figure 5.1.1: The real and imaginary components of the dielectric function for bulk (top row) and monolayer (bottom row) FeSn at $q = 0$. The labels refer to indices ij.

In general, the dielectric function is a 3×3 tensor

$$\begin{pmatrix} \varepsilon^{11} & \varepsilon^{12} & \varepsilon^{13} \\ \varepsilon^{21} & \varepsilon^{22} & \varepsilon^{23} \\ \varepsilon^{31} & \varepsilon^{32} & \varepsilon^{33} \end{pmatrix} \tag{5.3}$$

that reflects anisotropy in real materials. ε^{ij} describes the response of the material along the i-axis to an external field applied along the j-axis. The on-diagonal elements are the longitudinal components of the dielectric tensor. They characterise responses that are oriented along the same axis as the applied field. The off-diagonal components, on the other hand, pertain to responses that arise along an axis that is different from the orientation of the applied external field. The components of the dielectric tensor, in general, are functions of both frequency ω and wave vector $\mathbf{q}$.

In Elk, the indices $i, j = 1, 2, 3$ in ε^{ij} refer to the a, b, or c crystal axes, respec-

tively. Figure 5.1.1 presents the real and imaginary components of the dielectric tensor of bulk and monolayer FeSn for $\mathbf{q} = 0$, which is the Γ point of the first Brillouin zone. As illustrated in Figure 5.1.3, the Γ point is the centre while the M point is a boundary of the first Brillouin zone of a hexagonal crystal.

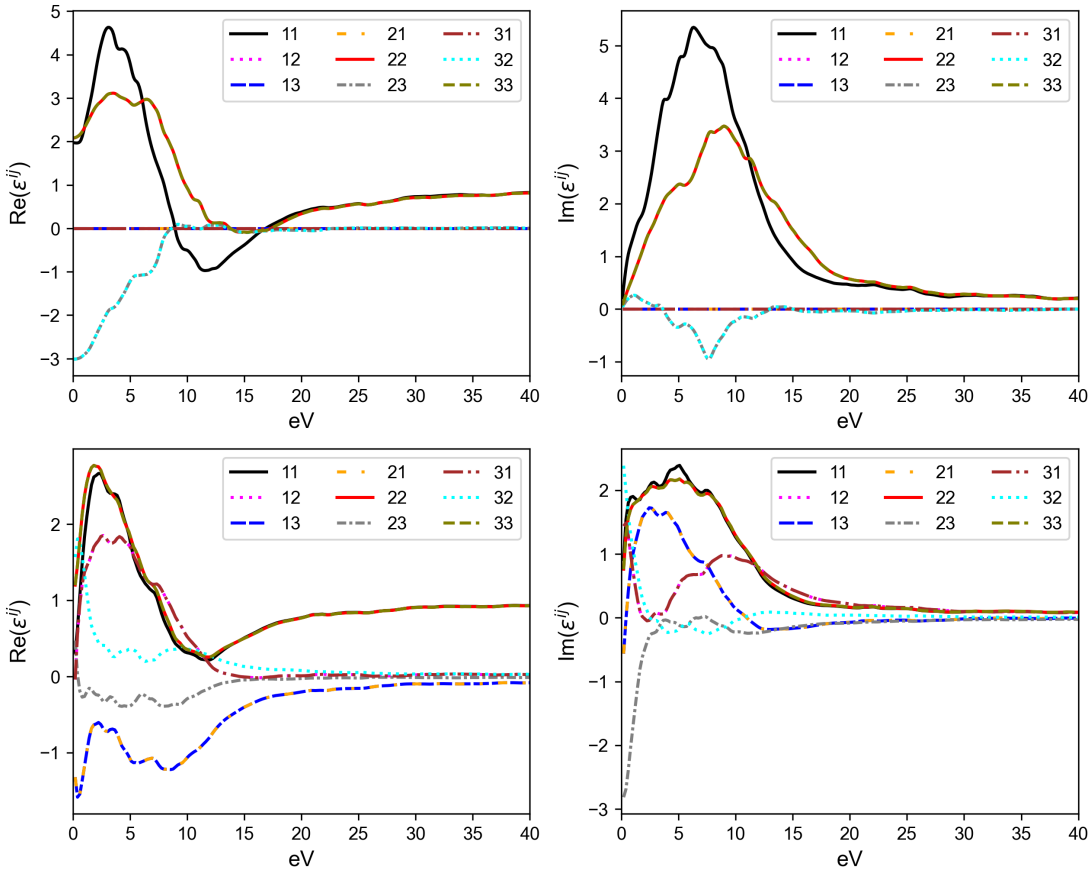

Figure 5.1.2: The real and imaginary components of the dielectric function for bulk (top row) and monolayer (bottom row) FeSn at $q = \mathrm{M}$. The labels refer to indices ij.

In both bulk and monolayer structures for $q = 0$, the calculated dielectric tensor is diagonal, where $\varepsilon^{11} = \varepsilon^{22}$, and ε^{33} has a different value:

$$\begin{pmatrix} \varepsilon^{11} & 0 & 0 \\ 0 & \varepsilon^{11} & 0 \\ 0 & 0 & \varepsilon^{33} \end{pmatrix}. \tag{5.4}$$

The components ε^{11} and ε^{22} pertain to response parallel to the kagome plane of FeSn. Thus, $\varepsilon^{11} = \varepsilon^{22}$ reflects the in-plane isotropy of the hexagonal crystal structure.

Figure 5.1.2 shows the behaviour of the dielectric function of bulk and monolayer FeSn away from $q = 0$, in particular at the M point of the first Brillioun

zone. In both cases, non-zero off-diagonal components occur and ε^{11} is no longer equal to ε^{22}. The presence of non-zero off-diagonal components indicate coupling between different directions in the response of the material to applied fields. Compared to Γ, which is the centre of the Brillouin zone, the Brillouin zone edge is no longer isotropic in-plane. Furthermore, at the M point, the dielectric tensor of the monolayer looks very different from the bulk. All off-diagonal components in the monolayer case are non-zero and the tensor is no longer symmetric.

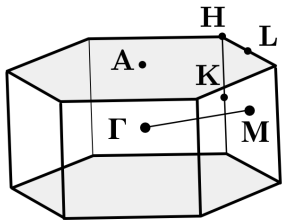

Figure 5.1.3: The path between q points Γ and M in the first Brillouin zone of a hexagonal crystal is indicated by the connecting line. Other high-symmetry points are also shown.

Often, the wavelengths of electromagnetic radiation used as experimental probes are longer than the material's lattice constant. Thus, optical properties are usually deduced from the dielectric function in the $q \to 0$ limit, so that $\varepsilon = \varepsilon(\omega)$ and the dielectric function for $q = 0$ is the relevant quantity.

In the discussion that follows regarding the plasmons of bulk and monolayer FeSn, $\varepsilon(\mathbf{q}, \omega)$ refers to the longitudinal component ε^{11}, as it was the dielectric tensor component that was used to obtain the plasmon dispersions.

5.2 Bulk FeSn plasmons

Being metallic, bulk FeSn supports plasmons that come from the longitudinal oscillations of the conduction electrons occupying bands crossing the Fermi energy. The electronic band structure of paramagnetic bulk FeSn is shown in Figure 5.2.1.

The calculated loss function $-\mathrm{Im}(\varepsilon^{-1}(\mathbf{q}, \omega))$ for paramagnetic bulk FeSn obtained for several values of momentum transfer $\mathbf{q}$ along the path from Γ ($q = 0$) to M ($q = 0.19$ Å^{-1}) in the first Brillouin zone of the material is shown in Figure 5.2.2.

The main peak of each loss function corresponds to $\mathrm{Re}(\varepsilon(\mathbf{q}, \omega)) = 0$ (see Figure 5.2.3), where the real part of the dielectric function crosses zero from negative to

positive values, and to small $\mathrm{Im}(\varepsilon(\mathbf{q},\omega))$. Thus, the main peaks are associated with plasmons. The conditions for identifying plasmons in the loss spectra can be gleaned from (1.7) and from (3.34).

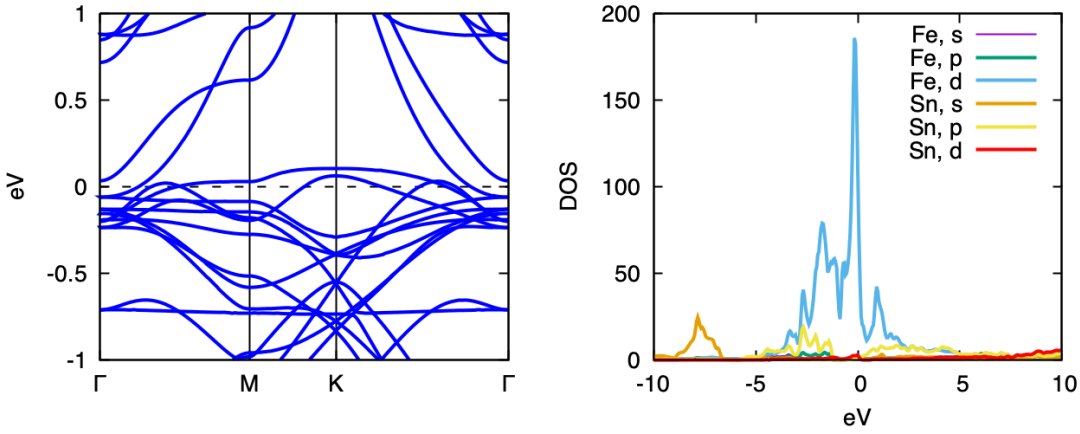

Figure 5.2.1: Electronic band structure of bulk FeSn (left) and density of states (DOS) (right) projected on the s, p, and d states of an Fe and an Sn atom of a kagome layer of bulk FeSn. The Fermi energy is set to zero.

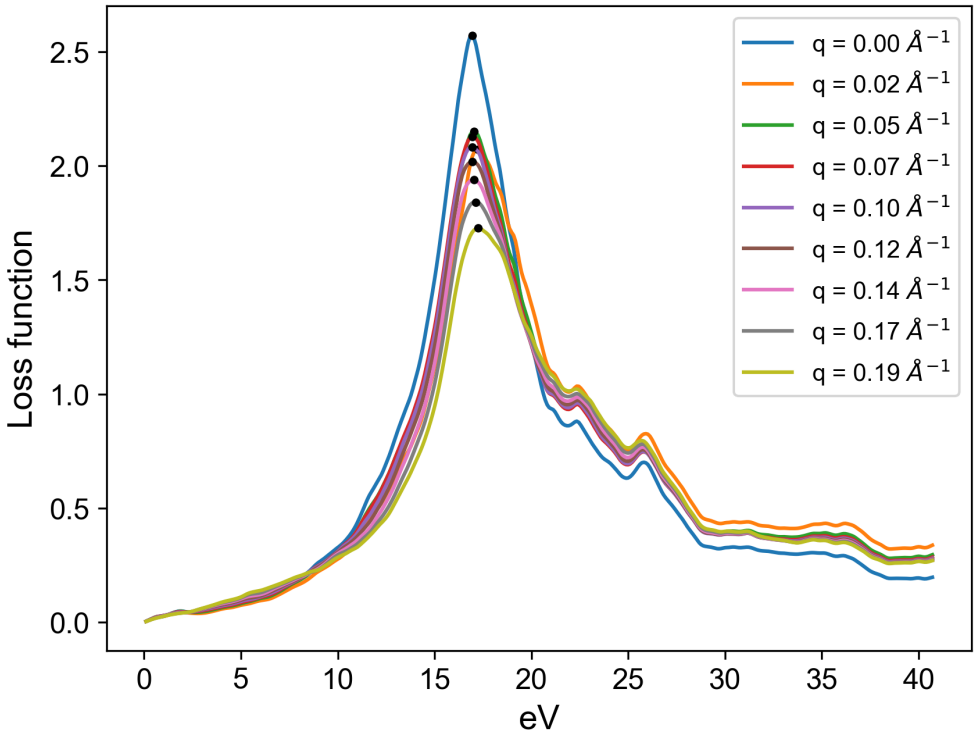

Figure 5.2.2: The loss function of bulk FeSn for various $\mathbf{q}$ along $\overline{\Gamma M}$ in the first Brillouin zone. Γ is $q = 0$ and M is $q = 0.19$ Å^{-1}. Black dots mark the plasmon peaks.

In general, for bulk FeSn, the plasmon peak of the loss function advances to higher energies for larger q, the length of the wave vector along $\overline{\Gamma M}$. At the same

time, for increasing q, the plasmon peak broadens and loses intensity. This indicates the influence of the electron-hole continuum.

The electron-hole continuum is a region of the energy–wave vector plane that is dominated by single-particle excitations (see Figure 1.2.2). In this region, electrons transition to unoccupied bands upon excitation, leaving behind positively charged holes. This process is also known as interband transition. In the homogenous electron gas model [52] of electron-density excitations, away from $q = 0$, plasmon energies move closer to the electron-hole continuum and thus collective excitations increasingly experience what is known as Landau damping. When plasmons interact with the electron-hole continuum, they decay as they impart their energy to the generation of electron-hole pairs. Thus, well within the electron-hole continuum, plasmons no longer exist.

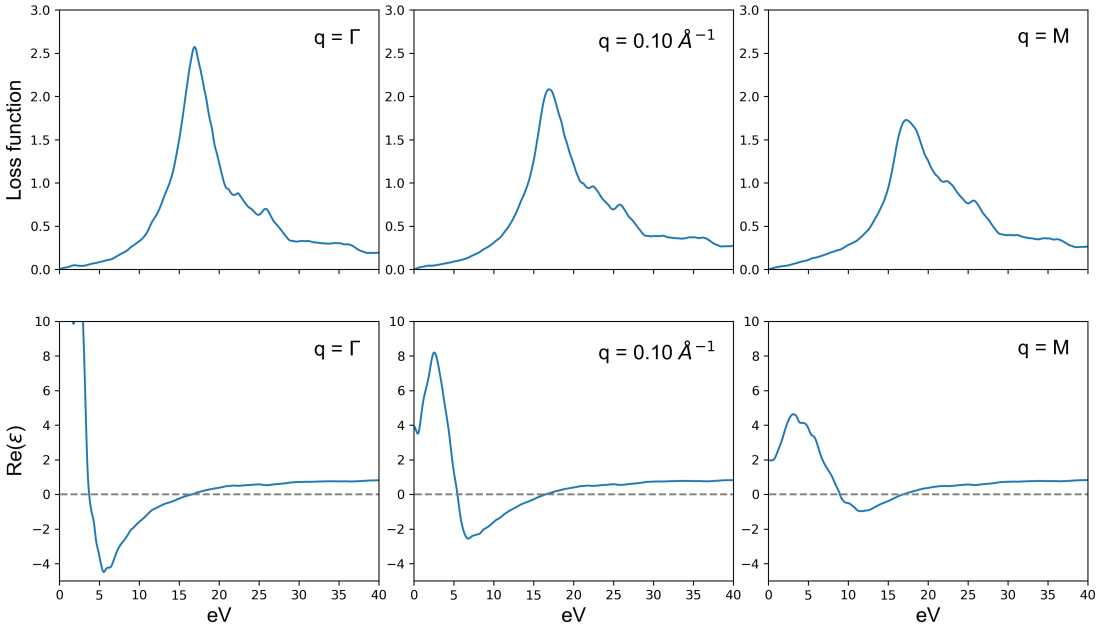

Figure 5.2.3: Correspondence between the main peak of the loss function (top row) and the zero-crossing of the real part of the dielectric function (bottom row), shown for three values of $q(= \Gamma, 0.10$ Å^{-1}, M) in bulk FeSn. Top and bottom rows share the same horizontal axis.

The imaginary part of the dielectric function, which gives the absorption spectra of a material, is associated with interband transitions and is therefore related to plasmon damping [33, 51]. Plasmons experience damping when $\mathrm{Im}(\varepsilon(\mathbf{q}, \omega)) \neq 0$. As can be seen in Figure 5.2.4, as q increases, $\mathrm{Im}((\varepsilon(\mathbf{q}, \omega))$ also increases around the frequency where $\mathrm{Re}(\varepsilon(\mathbf{q}, \omega)) = 0$ occurs. This is in correspondence with the broadening of the plasmon peak of the loss function for increasing q. The location of the peaks of $\mathrm{Im}((\varepsilon(\mathbf{q}, \omega))$ indicate that bulk FeSn absorbs light in the visible to

ultraviolet part of the electromagnetic spectrum.

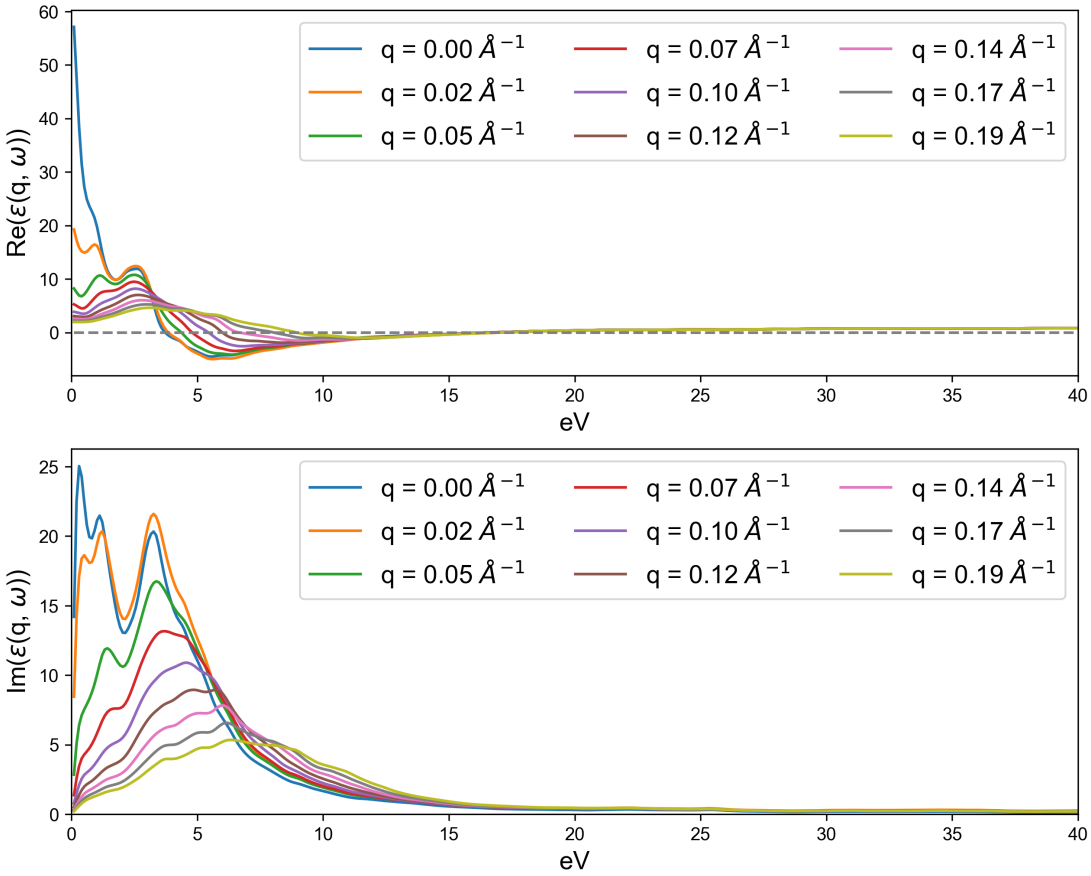

Figure 5.2.4: The real (top) and imaginary parts (bottom) of the dielectric function of bulk FeSn for various $\mathbf{q}$ along $\overline{\Gamma M}$ in the first Brillouin zone.

Since high values of $\mathrm{Im}((\varepsilon(\mathbf{q},\omega))$ occur within the electron-hole continuum, the shape of the electron-hole continuum itself can be gleaned from the dielectric function. The colour map of $\mathrm{Im}((\varepsilon(\mathbf{q},\omega))$ in Figure 5.2.5 shows high intensity near the Γ point, where the peaks of $\mathrm{Im}((\varepsilon(\mathbf{q},\omega))$ for various wave vectors along $\overline{\Gamma M}$ are highest. It also shows that single-particle excitation energies increase away from $q = 0$, as can be expected from predictions based on the homogenous electron gas model. However, in contrast to this model, the electron-hole continuum is finite even at $q = 0$, suggesting that interband transitions exert some influence on plasmons in bulk FeSn even for very short wave vectors.

The relation between energy and wave vector is presented in the dispersion plot for plasmons of bulk FeSn in Figure 5.2.6. At the Γ point, the plasmon energy is $\sim$ 16.5 eV, which is within the ultraviolet frequency regime that is usual for metals [49]. Bulk FeSn plasmons are almost dispersionless from $q = 0.07$ Å^{-1} to $q = 0.12$Å^{-1}. In this region, the plasmon energy is almost constant, with a value that is close to the energy at $q = \Gamma$. Given that the slope of the dispersion relation

describes plasmon group velocity ($v = d\omega/dq$), the almost-flat slope suggests that electron density oscillations exist as standing waves within this wave vector region. Beyond this region, the plasmon energy slowly rises quadratically (see Figure 5.2.6) as q moves towards the M point, as is expected for a bulk material for larger wave vectors. The positive slope of the dispersion suggests the forward propagation ($v > 0$) of plasmons for wave vectors nearer the edge of the Brillouin zone.

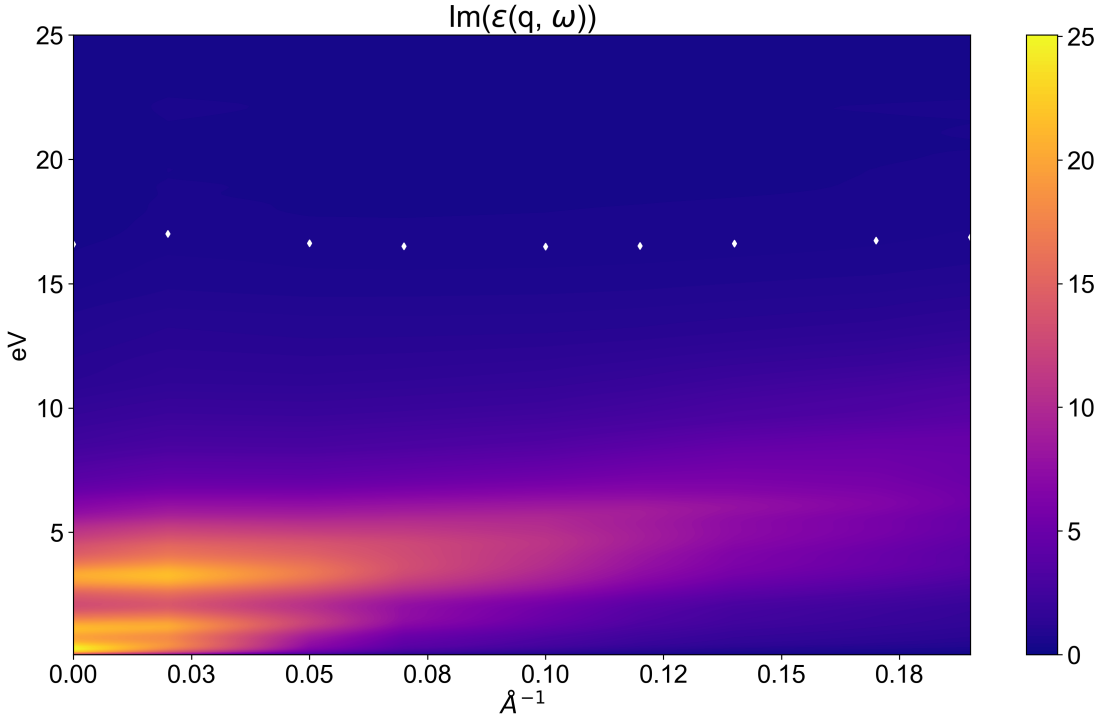

Figure 5.2.5: Colour map of $\mathrm{Im}(\varepsilon(\mathbf{q}, \omega))$ for bulk FeSn. Bright yellow and dark violet indicate the highest and lowest values of $\mathrm{Im}(\varepsilon(\mathbf{q}, \omega))$, respectively. The plasmon dispersion for bulk FeSn is superimposed as white dots.

A notable contrast to predictions based on the homogenous electron gas for bulk systems is the behaviour of the dispersion relation near $q = 0$. Between $q = 0$ and about $q = 0.05$ Å^{-1}, the plasmon energy rises before falling back to a value close to the energy obtained for $q = 0$. This suggests that plasmons propagate forward ($v > 0$) until around $q = 0.02$ Å^{-1} then propagate backward ($v < 0$) until the dispersion curve flattens out halfway between Γ and M. From Figure 5.2.2, it can be see that an abrupt broadening of the loss function for $q = 0.02$ Å^{-1} pulls the peak to a higher energy relative to the peaks for neighbouring q. Random-phase approximation (RPA) calculations, which were performed to check for the presence of this rise in the plasmon dispersion using a different method, contain the same dispersion behaviour. The plasmon energies from RPA are slightly higher than the LDA values, with the largest difference of only 0.18 eV at the M point.

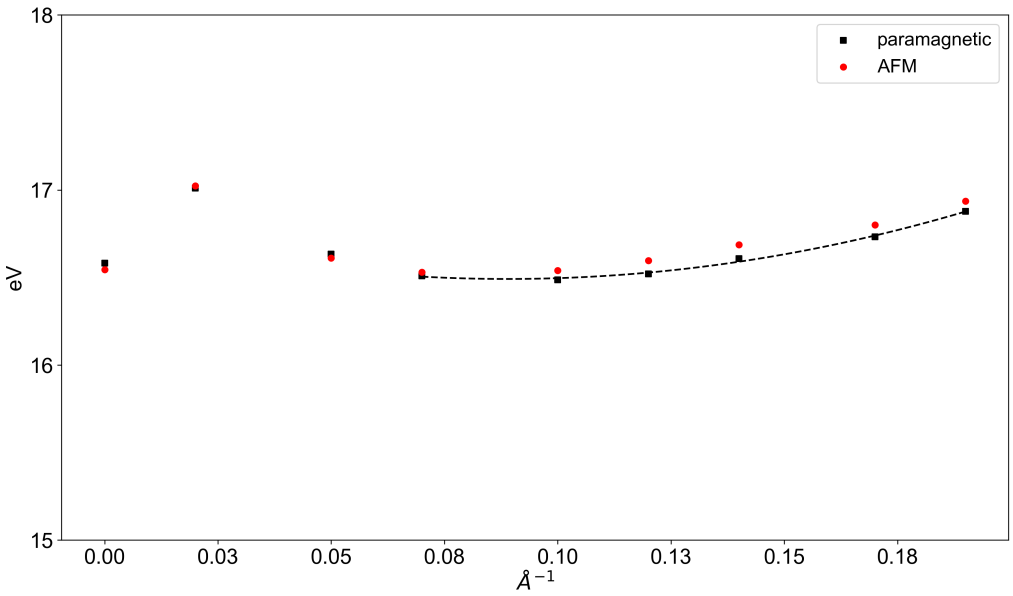

Figure 5.2.6: Plasmon dispersion relation for bulk FeSn. Black/red dots are for the paramagnetic/AFM case. The dashed line is the quadratic fit for values away from $q = 0$, for the paramagnetic case.

The plasmon dispersion for bulk FeSn is superimposed over the colour map of $\mathrm{Im}(\varepsilon(\mathbf{q}, \omega))$ (see Figure 5.2.6). Throughout the Brillouin zone region $\overline{\Gamma M}$, the plasmon dispersion steers clear of the electron-hole continuum. Plasmons of bulk FeSn continue to exist outside of the electron-hole continuum at the M point and hence are not significantly damped at this Brillouin zone boundary. This accords with the loss function still having a distinct main peak at $q = \mathrm{M}$ (0.19 Å^{-1}).

The plasmon dispersion of bulk FeSn in the antiferromagnetic (AFM) state was also obtained. The AFM dispersion plot, shown as red dots in Figure 5.2.6, follows the shape obtained for the paramagnetic case. The calculated plasmon energies for the paramagnetic and AFM cases are comparable, the largest difference being 0.08 eV near the Brillouin zone edge. This suggests that the behaviour of plasmons in FeSn is not significantly altered when the material is in the AFM state. In the following discussion of plasmons in monolayer FeSn, only the paramagnetic case is considered.

5.3 Monolayer FeSn plasmons

The electronic band structure of paramagnetic monolayer FeSn is shown in Figure 5.3.1. Like in the bulk case, plasmons in monolayer FeSn come from conduction bands crossing the Fermi energy. As will be discussed later in this section, these longitudinal oscillations are affected by electron transitions between bands.

In contrast to the bulk case, the calculated loss function for different values of $\mathbf{q}$ along $\overline{\Gamma M}$ (Figure 5.3.2) has a more complex shape, which drastically changes along with the wave vector length q. Unlike in bulk FeSn, where the highest point in the loss function corresponds to $\mathrm{Re}(\varepsilon(\mathbf{q},\omega)) = 0$, in the monolayer case the zero-crossing of the real part of the dielectric function matches a shoulder that occurs prior to the highest point. This is clearly seen in the loss function calculated for Γ (see Figure 5.3.3).

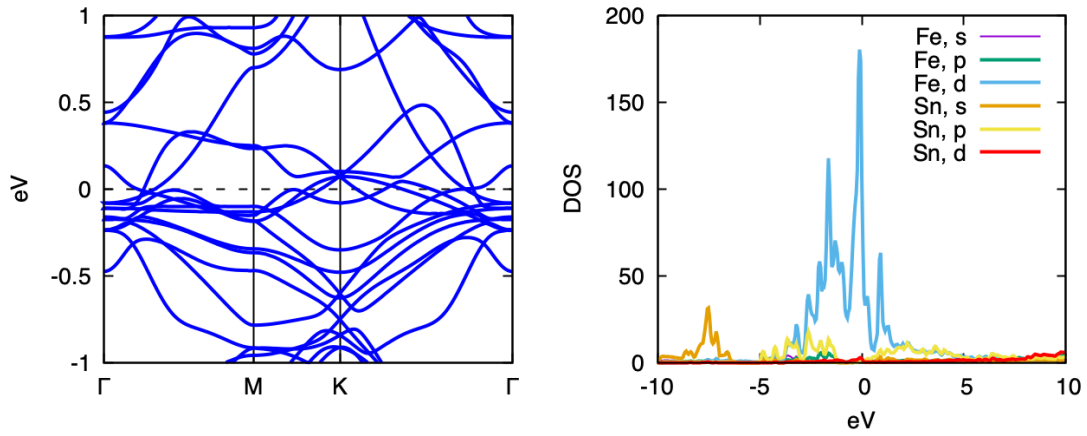

Figure 5.3.1: Electronic band structure of mnolayer FeSn (left) and density of states (DOS) (right) projected on the s, p, and d states of an Fe and an Sn atom of a kagome layer of monolayer FeSn. The Fermi energy is set to zero.

As in the case for the bulk, the loss function for Γ in the monolayer is the tallest and most well-defined among the calculated curves. Compared to the bulk, however, the monolayer loss function for Γ is much shorter and broader. As q increases, the loss function for monolayer FeSn quickly loses its shape and is substantially broadened and flattened towards the Brillouin zone edge. The shoulder that corresponds to $\mathrm{Re}(\varepsilon(\mathbf{q},\omega)) = 0$ is already hardly discernible for $q = 0.12$ Å^{-1}, as can be seen in Figure 5.3.3. This points to significant damping of plasmons away from $q = 0$. Indeed, from $q = 0.17$ Å^{-1}, $\mathrm{Re}(\varepsilon(\mathbf{q},\omega))$ no longer crosses zero and is positive throughout the energy range considered. This can be seen in Figure 5.3.4, which also shows that the dip in the curve that develops as $\mathrm{Re}(\varepsilon(\mathbf{q},\omega))$ changes signs, becomes shallower as q increases. This behaviour in the real part of the the dielectric function is accompanied by an increase in $\mathrm{Im}(\varepsilon(\mathbf{q},\omega))$ at the energy where $\mathrm{Re}(\varepsilon(\mathbf{q},\omega)) = 0$ occurs (see Figure 5.3.4), pointing to the increasing influence of interband transitions on the plasmons.

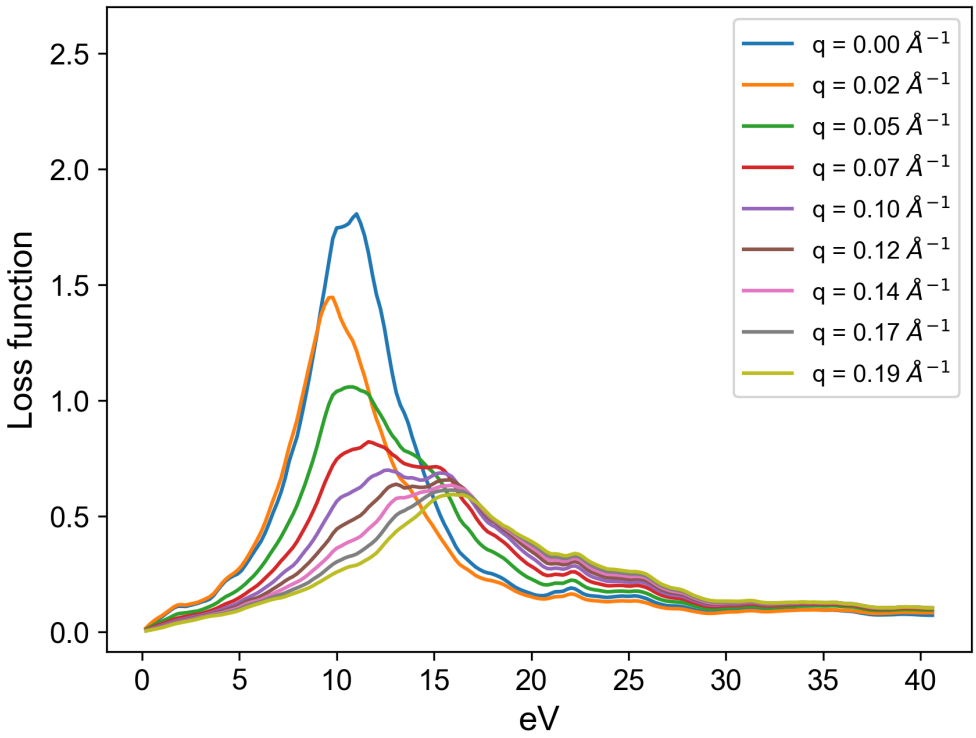

Figure 5.3.2: The loss function of monolayer FeSn for various **q** along $\overline{\Gamma M}$ in the first Brillouin zone.

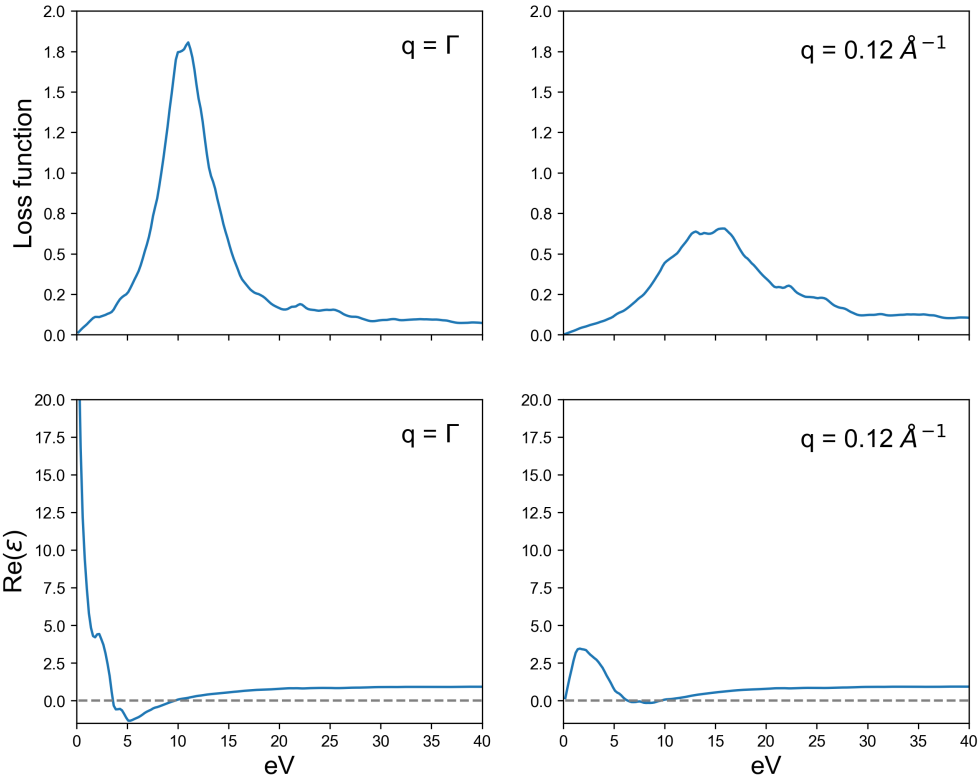

Figure 5.3.3: The loss function (top row) and the real part (bottom row) of the dielectric function for $q = \Gamma$ and $q = 0.12$ Å^{-1}. The zero-crossing of Re(ε) corresponds to a shoulder that occurs before the main peak.

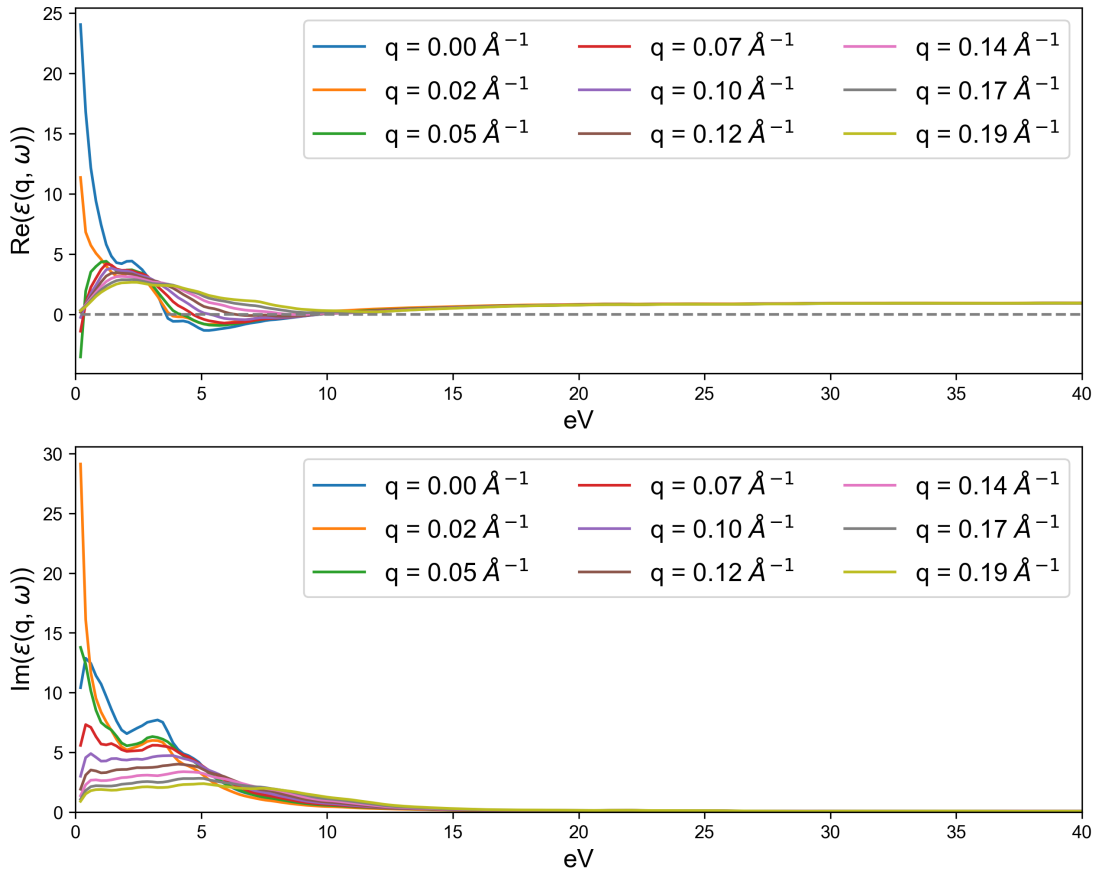

Figure 5.3.4: The real (top) and imaginary (bottom) parts of the dielectric function (bottom) for different values of $\mathbf{q}$ along $\overline{\Gamma M}$.

Thus, in monolayer FeSn, plasmons are considerably damped as q increases. From $q = 0.17$ Å^{-1}, plasmons in monolayer FeSn no longer exist. This suggests that near the Brillouin zone edge, excitations occur within the electron-hole continuum [61, 62] and plasmons decay into single-particle interband transitions. Compared to the bulk case, therefore, plasmons of monolayer FeSn are short-lived.

The colour map of $\mathrm{Im}(\varepsilon(\mathbf{q}, \omega))$ for monolayer FeSn is presented in Figure 5.3.5. The faint colouring reflects the lower intensity of $\mathrm{Im}(\varepsilon(\mathbf{q}, \omega))$ for the monolayer and corresponds to the uniformity of the values of $\mathrm{Im}(\varepsilon(\mathbf{q}, \omega))$ for wave vectors nearer the Brillouin zone boundary. As in the bulk case, the shape formed by $\mathrm{Im}(\varepsilon(\mathbf{q}, \omega)) \neq 0$ indicates that the electron-hole continuum is finite at $q = 0$ for the monolayer.

In Figure 5.3.5, the superimposed monolayer FeSn plasmon dispersion can be seen to lie closer to the electron-hole continuum. This reflects the observation that even for small q, $\mathrm{Im}(\varepsilon(\mathbf{q}, \omega))$ for the monolayer is appreciable near $\mathrm{Re}(\varepsilon(\mathbf{q}, \omega)) = 0$ (see Figure 5.3.4), pointing to a more pronounced influence of the electron-hole

continuum compared to bulk FeSn. Such influence results in the broadened and more complex loss function shape. Beyond $q = 0.14$ Å^{-1}, Re($\varepsilon(\mathbf{q}, \omega)$) becomes positive throughout, suggesting that the plasmon dispersion enters the electron-hole continuum. Thus, for larger q values along $\overline{\Gamma M}$, plasmons in monolayer FeSn no longer exist.

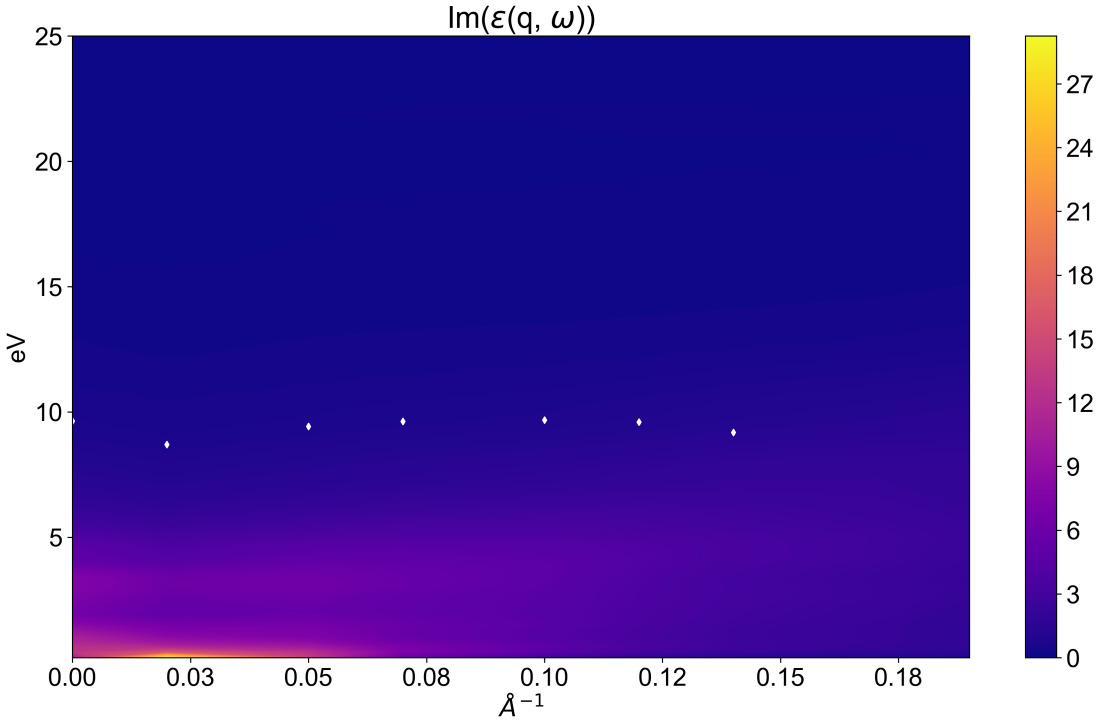

Figure 5.3.5: Colour map of Im($\varepsilon(\mathbf{q}, \omega)$) for monolayer FeSn. Bright yellow and dark violet indicate the highest and lowest values of Im($\varepsilon(\mathbf{q}, \omega)$), respectively. The plasmon dispersion for monolayer FeSn is superimposed as white dots.

The plasmon dispersion for monolayer FeSn, obtained from Re($\varepsilon(\mathbf{q}, \omega)$) = 0 and shown in Figure 5.3.6, starts at $q = 0$ at a lower energy (~ 9.6 eV) compared to the bulk case. This is expected from the reduced thickness and hence lower electron density of the monolayer structure. As for bulk FeSn, the monolayer plasmon dispersion shows a considerable change in plasmon energy between $q = 0$ and $q = 0.05$ Å^{-1}. However, in the monolayer case, the plasmon dispersion first dips before rising back.

In contrast to the homogenous electron gas model for longitudinal charge density oscillations in two-dimensional systems, whose dispersion is characterised by a $\sqrt{q}$ curve [52], the plasmon dispersion for monolayer FeSn is finite at $q = 0$. In addition, the dispersion is almost flat between $q = 0.07$ Å^{-1} and $q = 0.12$ Å^{-1}, in the middle of the path $\overline{\Gamma M}$. Also contrary to the electron gas model for plasmons in two-dimensional systems, the FeSn monolayer dispersion plot curves downward

towards the edge of the Brillouin zone. This gives a negative slope, suggesting the backward propagation of plasmons ($v < 0$) near the M point.

Plasmon dispersions that contrast with homogenous electron gas predictions of a $\sqrt{q}$ curve have also been found from ab-initio calculations for certain materials that possess a quasi-2D structure (2D materials that are more than one-atom-thick). Flatness and negative slope in their plasmon dispersions have been associated with local field effects [120, 121]. Local field effects are microscopic-scale variations in the electric field in the material, that are especially relevant in the presence of inhomogeneity [102, 107].

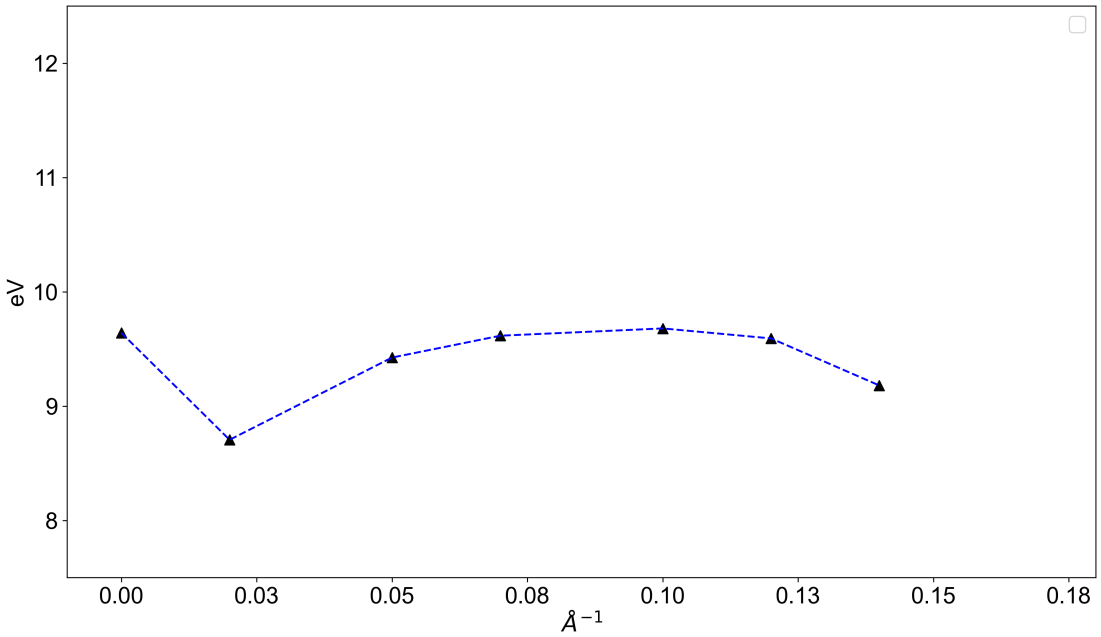

Figure 5.3.6: Plasmon dispersion relation for monolayer FeSn. The dashed line is a guide to the eye.

In Elk, the calculation of the macroscopic dielectric function (discussed in the chapter on TDDFT) is calculated using a matrix in reciprocal lattice vectors $\mathbf{G}$ and $\mathbf{G}'$. This matrix, whose size is determined by the parameter `gmaxrf`, accounts for local field effects. One would expect that because of the truncation along the $c-$axis, local field effects would be more pronounced in monolayer FeSn compared to the bulk structure. However, as noted in the chapter on computational details, the `gmaxrf` value used for the plasmon calculations for the FeSn monolayer is not a converged value due to computational expense. Thus, further investigation of local field effects and how convergence in terms of the $\mathbf{G}$ and $\mathbf{G}'$ vectors might affect the monolayer plasmon dispersion, including the gap at $q = 0$, would be useful in understanding plasmon behaviour in monolayer FeSn.

CHAPTER

SIX

MAGNONS IN BULK AND MONOLAYER FeSn

6.1 Bulk FeSn magnons

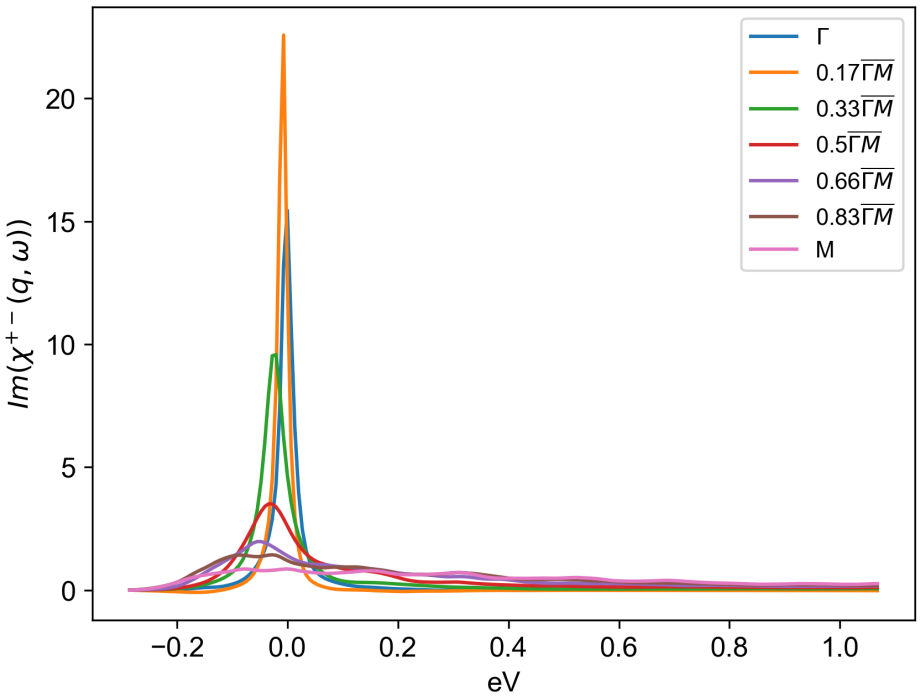

Figure 6.1.1: The imaginary part of the transverse spin-spin response function $\mathrm{Im}(\chi^{+-}(\mathbf{q},\omega))$ of bulk FeSn for various $\mathbf{q}$, which appear here as fractions of the path $\overline{\Gamma M}$ in the first Brillouin zone.

Figure 6.1.1 shows the imaginary part of the transverse spin-spin response function $\mathrm{Im}(\chi^{+-}(\mathbf{q},\omega))$ calculated for various wave vectors $\mathbf{q}$ along the path connecting the Γ and M points of the first Brillouin zone of bulk FeSn. The magnon excitation energies are the energies where the peaks of $\mathrm{Im}(\chi^{+-}(\mathbf{q},\omega))$ occur. To satisfy the Goldstone theorem [122], which stipulates the vanishing of magnons at $q = 0$

[5, 68], the finite magnon excitation energy obtained for $q = \Gamma$ — the so-called Goldstone error [111, 123] — was subtracted from all calculated spectra. This process shifted the peak of $\mathrm{Im}(\chi^{+-}(\mathbf{q},\omega))$ to $\hbar\omega = 0$. The magnon dispersion for bulk FeSn, superimposed as black dots in Figure 6.1.2 was obtained using the absolute values of the energies at which the shifted peaks occur. Many TDDFT codes, including Elk, are known to introduce the Goldstone error as an artefact of numerical computation [111, 115].

The calculated $\mathrm{Im}(\chi^{+-}(\mathbf{q},\omega))$ starts out near $q = 0$ with a well-defined peak. From around the middle of the path $\overline{\Gamma M}$, however, the peak broadens and begins to disintegrate, until it is no longer well-defined at the M point. This behaviour is indicative of Landau damping for magnons, which stems from the influence of the Stoner continuum [124]. At certain wave-vectors, magnetic excitations are dominated by single-particle spin-flip processes, in which electrons transition from a spin-polarised band to a band with opposite spin polarisation. Inside this region, called the Stoner continuum, magnons decay into such single-particle spin-flip transitions. These single-particle spin excitation are especially pronounced in magnetic metals, where itinerant conduction electrons interact via the exchange interaction and form the Stoner continuum [69, 124].

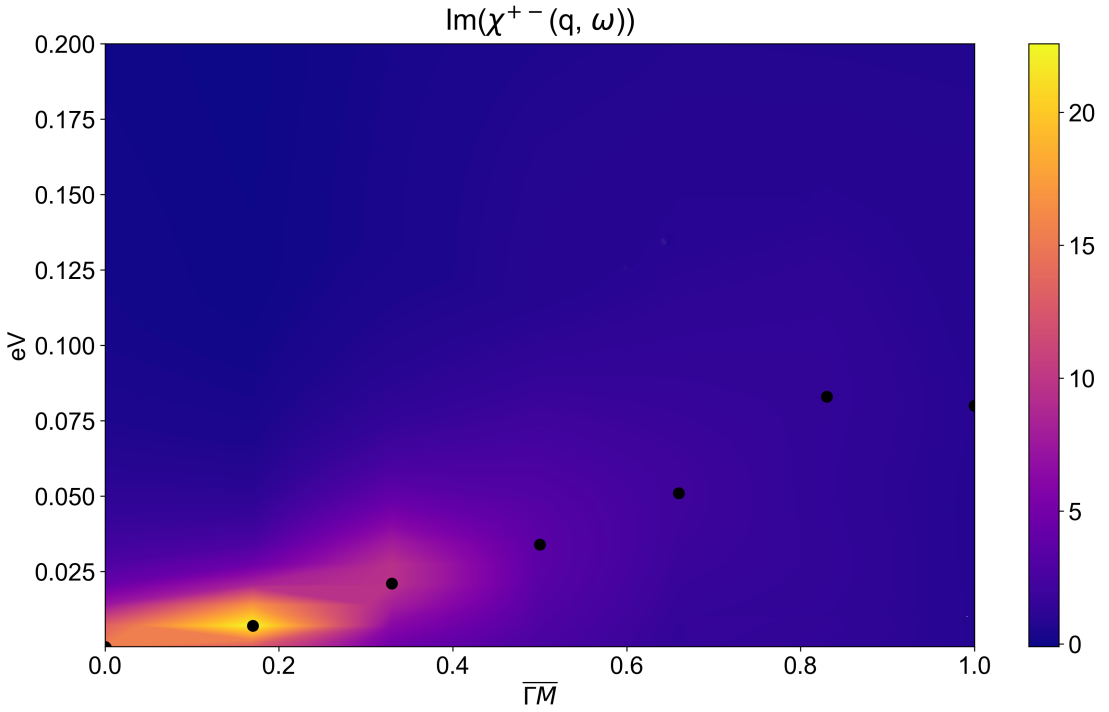

Figure 6.1.2: Colour map of $\mathrm{Im}(\chi^{+-}(\mathbf{q},\omega))$ for bulk FeSn. Bright yellow and dark violet indicate the highest and lowest values of $\mathrm{Im}(\chi^{+-}(\mathbf{q},\omega))$, respectively. The magnon dispersion for bulk FeSn is superimposed as black dots. The horizontal axis shows fractions of the $\overline{\Gamma M}$ distance.

The magnon dispersion for bulk FeSn is linear near $q = 0$, as is expected for an antiferromagnetic metal from theoretical predictions based on the Heisenberg exchange model [69, 70]. The magnon energy steadily rises with increasing q values starting from Γ. This positive slope of the dispersion points to the forward propagation of magnons ($v = d\omega/dq > 0$) for the majority of wave vectors along the $\overline{\Gamma M}$ path. Near the M point, the dispersion plateaus at ~ 80 eV, which suggests that at the Brillouin zone boundary, the spin-wave group velocity approaches zero, resulting in a standing wave. The obtained magnon dispersion is in agreement with previous studies on bulk FeSn [29–31].

In the colour map of $\mathrm{Im}(\chi^{+-}(\mathbf{q}, \omega))$ for bulk FeSn, the superimposed magnon dispersion follows the shape formed by the peaks of $\mathrm{Im}(\chi^{+-}(\mathbf{q}, \omega))$. While the peaks are most intense near the Γ point, the intensity quickly fades and becomes significantly smudged out about halfway between Γ and M. This reflects the disintegration of the magnon peak, as shown in Figure 6.1.1, which can be attributed to the influence of the Stoner continuum.

6.2 Monolayer FeSn magnons

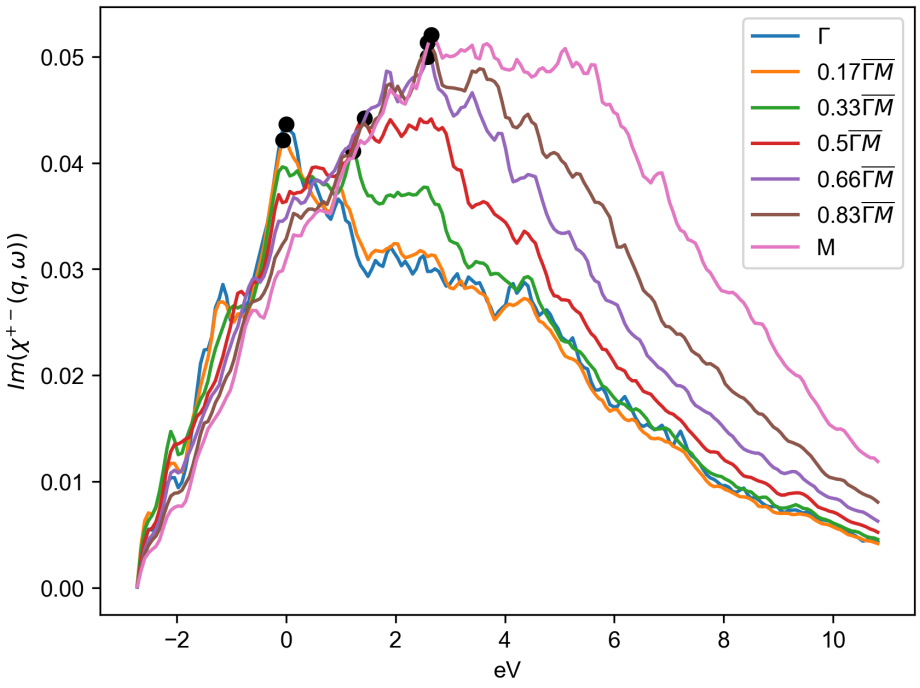

Figure 6.2.1: Peaks of $\mathrm{Im}(\chi^{+-}(\mathbf{q}, \omega))$ for monolayer FeSn for different values of q along the path $\overline{\Gamma M}$ in the first Brillouin zone. Black dots indicate the highest point in each curve.

In contrast to the bulk case where $\mathrm{Im}(\chi^{+-}(\mathbf{q},\omega))$ begins as a simple curve for $q = \Gamma$, all $\mathrm{Im}(\chi^{+-}(\mathbf{q},\omega))$ curves obtained for the monolayer structure are jagged, showing multiple high points, as can be seen in Figure 6.2.1. Though $\mathrm{Im}(\chi^{+-}(\mathbf{q},\omega))$ intensifies with increasing q, the curve broadens and the distinctness of the peak at $q = \Gamma$ is lost. In consequence, the region of high intensity in the colour map of $\mathrm{Im}(\chi^{+-}(\mathbf{q},\omega))$ in Figure 6.2.2 for the monolayer case is very broad compared to the bulk case and it stretches all the way to the Brillouin zone boundary.

The resulting plasmon dispersion, obtained from the highest points of $\mathrm{Im}(\chi^{+-}(\mathbf{q},\omega))$ and which is superimposed on the colour map in Figure 6.2.2, is vaguely linear, with a small slope in the middle of the path $\overline{\Gamma M}$. The dispersion is almost constant nearer to the M point. The highest magnon excitation energy obtained for the structure is ~ 2 eV, higher than what is usually obtained for AFM magnons, which can go up to a few terahertz [125].

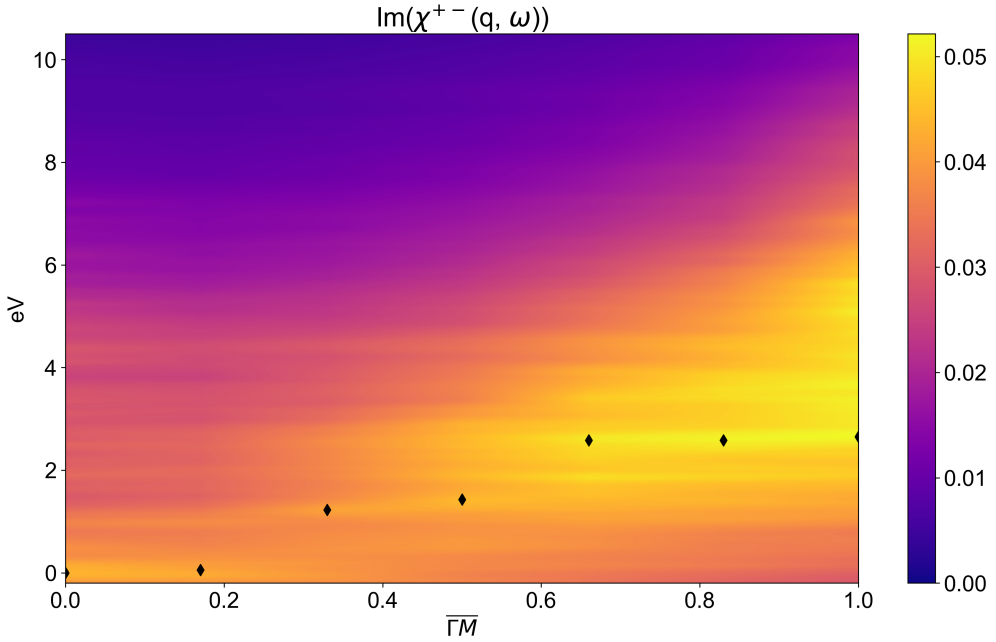

Figure 6.2.2: Colour map of $\mathrm{Im}(\chi^{+-}(\mathbf{q},\omega))$ for monolayer FeSn. Bright yellow and dark violet indicate the highest and lowest values, respectively. The magnon dispersion for monolayer FeSn is superimposed as black dots. The horizontal axis shows fractions of the $\overline{\Gamma M}$ distance.

It should be noted that in the calculations for the magnon dispersion, the slab structure had to be rotated in order for Elk to recognise the magnetic configuration as collinear and thereby generate the transverse spin-spin response function. While this does not seem to have a noticeable effect on the bulk structure, it might have introduced computational artefacts that are more evident in the case of the slab

model. The parameter `gmaxrf` is also not converged for the magnon calculations. While it does not seem to have greatly affected the bulk magnon calculations (given the agreement with results from previous studies), it might have generated a more significant effect on the monolayer. The results obtained for the magnon dispersion of the FeSn monolayer thus needs to be validated and the possible effect of the rotation of the slab as well as of `gmaxrf` convergence investigated.

CHAPTER

SEVEN

CONCLUDING REMARKS AND OUTLOOK

To study plasmons in FeSn, the loss function as well as the real and imaginary parts of the dielectric function $\varepsilon(\mathbf{q}, \omega)$ were obtained via TDDFT for different wave vectors $\mathbf{q}$ along the path $\overline{\Gamma M}$ of the material's first Brillouin zone. TDDFT calculations for magnons were performed as well, and the magnon dispersion for bulk and monolayer FeSn were obtained from the peaks of the imaginary part of the transverse spin-spin response function $\chi^{+-}(\mathbf{q}, \omega)$.

For bulk FeSn, the plasmon energy obtained at the Γ point $q = 0$ is within the range expected for a metal and the plasmon dispersion rises quadratically nearer to the Brillouin zone boundary. Throughout the path $\overline{\Gamma M}$, the plasmon dispersion lies away from the electron-hole continuum, so that bulk plasmons continue to be long-lived at the edge of the first Brillouin zone at the M point. Many of these results conform to theoretical expectations for a metallic bulk material.

Compared to the bulk case, the plasmon energies obtained along $\overline{\Gamma M}$ of monolayer FeSn are lower. In addition, the plasmons are short-lived, pointing to a more pronounced interaction with the electron-hole continuum. Near the edge of the first Brillouin zone, plasmons in the FeSn monolayer no longer exist.

Several of the results obtained, however, goes against the predicted behaviour for plasmons based on analytical theories that use the homogenous electron gas as model. These deviations are particularly evident in the monolayer case. Contrary to the prediction of $\sqrt{q}$ behavior, the obtained monolayer plasmon dispersion is gapped. The middle of the dispersion curve is also nearly flat and the slope becomes negative nearer to the Brillouin zone boundary. Moreover, between $q = \Gamma$ and the nearly dispersionless portion of the curve, there is a conspicuous dip in

energy. This has a counterpart in the bulk plasmon dispersion, where the energy rises before it falls back to a value that is close to that found for $q = 0$.

When it comes to magnons, the results for bulk FeSn are once again more straightforward than the results for the monolayer. For bulk FeSn, the magnon dispersion starting from Γ rises linearly until it flattens out near the Brillouin zone edge at the M point. This behaviour and the energies obtained are comparable to those found in previous studies on FeSn. The dispersion also follows the theoretically expected linear curve for antiferromagnets. In contrast, the energies obtained for monolayer FeSn, which go up to ~ 2 eV, are higher than expected for an antiferromagnetic material. The calculated $\mathrm{Im}(\chi^{+-}(\mathbf{q}, \omega))$ curves are quite jagged, making the peaks harder to discern. As stated in the previous chapter, the magnon calculation results for monolayer FeSn may suffer from some computational artefact introduced by the rotation of the slab model and difficulties in parameter convergence. The results, particularly for the monolayer, thus need to be validated. One could use other TDDFT codes that employ techniques that may offer more computational efficiency (for instance [77]).

Returning to plasmons, it is recommended that the results obtained in this thesis be reproduced and validated, in particular to investigate the origins of the deviations from analytical predictions and thereby gain better insight into the plasmon behaviours described here. The gapped monolayer dispersion, local field effects, and factors that result in the rise/dip in plasmon energy merit further study. The monolayer case is particularly interesting, given also the recent attention being paid to plasmon behaviours in real materials [121, 126]. It might be helpful and instructive to use other methods, such as the GW method [121], or other TDDFT codes.

That being said, the presence of plasmon dispersion characteristics that deviate from theoretical expectations highlights the relevance of paying attention to possible differences between analytical models and real materials. In studies of plasmon-magnon coupling in 2D materials for instance, the theoretical $\sqrt{q}$ behaviour is usually assumed. However, as noted in the chapter on plasmons, published studies have pointed out the marked differences between this theoretical behaviour and the plasmon dispersion obtained for specific real 2D materials. The existence of such deviations also points to the value of ab-initio methods, which in principle provide a more realistic description of materials.

It would be intriguing to revisit the results in this work when efforts to fab-

ricate FeSn thin films and atomically-thin FeSn come to fruition, as results from experimental observations can then be compared to the TDDFT results presented here. Further computational studies can, in that case, be based on questions such experimental findings may raise.

An avenue for further study would be the investigation of the effects of spin-orbit coupling on the plasmon and magnon dispersions of FeSn. Spin-orbit coupling was not considered in the present work because of the huge computational overhead that it presented. In magnon dispersions, spin-orbit coupling is known to introduce a gap at $q = 0$. Since spin-orbit coupling changes the electronic band structure, it would be interesting to look into how it affects plasmons in FeSn as well.

Another path of future inquiry would be to study the effect of external magnetic fields on the collective excitations. In this work, the focus is on the paramagnetic case. Sufficiently strong external magnetic fields can change the magnetic properties of FeSn and affect excitations in the material.

Future work can also be done on the effects of an applied external electric field or of defects such as vacancies and impurities (doping) on the plasmons of bulk and monolayer FeSn. These factors can affect the electronic band structure, including the Fermi level, and may thus influence plasmon energies and the plasmon dispersion shape. It would be interesting to see if these factors could affect the plasmon energy for $q \to 0$ and perhaps make plasmon-magnon coupling possible, particularly in the monolayer case.

REFERENCES

[1] Eberhard K. U. Gross, E. Runge, and O. Heinonen. *Many-Particle Theory,* A. Hilger, Nov. 1991. 442 pp. ISBN: 978-0-7503-0155-8.

[2] David Pines. *Elementary Excitations In Solids*. Boca Raton: CRC Press, May 23, 2019. 312 pp. ISBN: 978-0-429-50085-5. DOI: 10.1201/9780429500855.

[3] Otfried Madelung. *Introduction to Solid-State Theory*. Red. by Manuel Cardona et al. Vol. 2. Springer Series in Solid-State Sciences. Berlin, Heidelberg: Springer, 1978. ISBN: 978-3-540-78061-8 978-3-642-61885-7. DOI: 10.1007/978-3-642-61885-7. URL: http://link.springer.com/10.1007/978-3-642-61885-7 (visited on 05/11/2023).

[4] William Jones and Norman Henry March. *Theoretical Solid State Physics*. Wiley-Interscience, 1973. 700 pp. ISBN: 978-0-471-44900-3.

[5] Piers Coleman. *Introduction to Many-Body Physics*. Cambridge: Cambridge University Press, 2015. ISBN: 978-0-521-86488-6. DOI: 10.1017/CBO9781139020916. URL: https://www.cambridge.org/core/books/introduction-to-manybody-physics/B7598FC1FCEE0285F5EC767E835854C8 (visited on 05/08/2023).

[6] Giuseppe Grosso and Giuseppe Pastori Parravicini. *Solid State Physics*. Elsevier, Feb. 14, 2000. 741 pp. ISBN: 978-0-08-048102-9.

[7] James D. Patterson and Bernard C. Bailey. *Solid State Physics: Introduction to the Theory*. Berlin, Heidelberg: Springer, 2007. ISBN: 978-3-540-24115-7 978-3-540-34933-4. DOI: 10.1007/978-3-540-34933-4. URL: https://link.springer.com/10.1007/978-3-540-34933-4 (visited on 05/09/2023).

[8] Steven M. Girvin. "Collective Excitations". In: *The Quantum Hall Effect*. Ed. by Richard E. Prange and Steven M. Girvin. Graduate Texts in Contemporary Physics. New York, NY: Springer US, 1987, pp. 353–378. ISBN: 978-1-4684-0499-9. DOI: 10.1007/978-1-4684-0499-9_9. URL: https://doi.org/10.1007/978-1-4684-0499-9_9 (visited on 05/08/2023).

[9] Charles Kittel. *Introduction to Solid State Physics*. Wiley, Nov. 11, 2004. 704 pp. ISBN: 978-0-471-41526-8.

[10] Neil W. Ashcroft and N. David Mermin. *Solid State Physics*. Holt, Rinehart and Winston, 1976. 868 pp. ISBN: 978-0-03-083993-1.

[11] J. Barnas. "Coupling of magnons to plasmons and to LA-phonons in the s-d model". In: *Acta Phys. Pol., A; (Poland)* 56:6 (Dec. 1, 1979). URL: https://www.osti.gov/etdeweb/biblio/6064224 (visited on 05/08/2023).

[12] J. Barnas. "A theoretical study of interactions in the magnon-plasmon system in ferromagnetic semiconductors". In: *Acta Physica Polonica Series A* 55.5 (1979). Place: Poland INIS Reference Number: 11553444, pp. 647–660. ISSN: 0587-4246.

[13] G. Baskaran and K. P. Sinha. "Plasmon-magnon interaction in magnetic semiconductors". In: *Pramana* 1.1 (July 1, 1973), pp. 31–36. ISSN: 0973-7111. DOI: 10.1007/BF02846146. URL: https://doi.org/10.1007/BF02846146 (visited on 05/08/2023).

[14] Sayandip Ghosh et al. *Plasmon-magnon interactions in two-dimensional honeycomb magnets*. Nov. 20, 2022. DOI: 10.48550/arXiv.2211.11098. arXiv: 2211.11098[cond-mat]. URL: http://arxiv.org/abs/2211.11098 (visited on 05/08/2023).

[15] Anna Dyrdał et al. *Magnon-Plasmon Hybridization Mediated by Spin-Orbit Interaction in Magnetic Materials*. Dec. 12, 2022. DOI: 10.48550/arXiv.2212.06105. arXiv: 2212.06105[cond-mat]. URL: http://arxiv.org/abs/2212.06105 (visited on 05/08/2023).

[16] Deshun Hong et al. "Molecular beam epitaxy of the magnetic Kagome metal FeSn on LaAlO3 (111)". In: *AIP Advances* 10.10 (Oct. 12, 2020), p. 105017. ISSN: 2158-3226. DOI: 10.1063/5.0001909. URL: https://doi.org/10.1063/5.0001909 (visited on 05/09/2023).

[17] Hisashi Inoue et al. "Molecular beam epitaxy growth of antiferromagnetic Kagome metal FeSn". In: *Applied Physics Letters* 115.7 (Aug. 12, 2019), p. 072403. ISSN: 0003-6951. DOI: 10.1063/1.5111792. URL: https://doi.org/10.1063/1.5111792 (visited on 05/09/2023).

[18] Durga Khadka et al. "High quality epitaxial thin films and exchange bias of antiferromagnetic Dirac semimetal FeSn". In: *Applied Physics Letters* 117.3 (July 22, 2020), p. 032403. ISSN: 0003-6951. DOI: 10.1063/5.0011497. URL: https://doi.org/10.1063/5.0011497 (visited on 05/09/2023).

[19] V. Baltz et al. “Antiferromagnetic spintronics”. In: *Reviews of Modern Physics* 90.1 (Feb. 15, 2018). Publisher: American Physical Society, p. 015005. DOI: 10.1103/RevModPhys.90.015005. URL: https://link.aps.org/doi/10.1103/RevModPhys.90.015005 (visited on 05/11/2023).

[20] Libor Šmejkal et al. “Topological antiferromagnetic spintronics”. In: *Nature Physics* 14.3 (Mar. 2018). Number: 3 Publisher: Nature Publishing Group, pp. 242–251. ISSN: 1745-2481. DOI: 10.1038/s41567-018-0064-5. URL: https://www.nature.com/articles/s41567-018-0064-5 (visited on 05/09/2023).

[21] Wei Han. “Magnetic Memory and Logic”. In: *Handbook of Magnetism and Magnetic Materials*. Ed. by J. M. D. Coey and Stuart S.P. Parkin. Cham: Springer International Publishing, 2021, pp. 1553–1592. ISBN: 978-3-030-63210-6. DOI: 10.1007/978-3-030-63210-6_33. URL: https://doi.org/10.1007/978-3-030-63210-6_33 (visited on 05/11/2023).

[22] Mingu Kang et al. “Dirac fermions and flat bands in the ideal kagome metal FeSn”. In: *Nature Materials* 19.2 (Feb. 2020). Number: 2 Publisher: Nature Publishing Group, pp. 163–169. ISSN: 1476-4660. DOI: 10.1038/s41563-019-0531-0. URL: https://www.nature.com/articles/s41563-019-0531-0 (visited on 05/09/2023).

[23] Minyong Han et al. “Evidence of two-dimensional flat band at the surface of antiferromagnetic kagome metal FeSn”. In: *Nature Communications* 12.1 (Sept. 15, 2021). Number: 1 Publisher: Nature Publishing Group, p. 5345. ISSN: 2041-1723. DOI: 10.1038/s41467-021-25705-1. URL: https://www.nature.com/articles/s41467-021-25705-1 (visited on 05/09/2023).

[24] Zhiyong Lin et al. “Dirac fermions in antiferromagnetic FeSn kagome lattices with combined space inversion and time-reversal symmetry”. In: *Physical Review B* 102.15 (Oct. 2, 2020). Publisher: American Physical Society, p. 155103. DOI: 10.1103/PhysRevB.102.155103. URL: https://link.aps.org/doi/10.1103/PhysRevB.102.155103 (visited on 05/09/2023).

[25] Daniel Multer et al. “Imaging real-space flat band localization in kagome magnet FeSn”. In: *Communications Materials* 4.1 (Feb. 22, 2023). Number: 1 Publisher: Nature Publishing Group, pp. 1–6. ISSN: 2662-4443. DOI: 10.1038/s43246-022-00328-1. URL: https://www.nature.com/articles/s43246-022-00328-1 (visited on 05/09/2023).

[26] William R. Meier et al. “Flat bands in the CoSn-type compounds”. In: *Physical Review B* 102.7 (Aug. 31, 2020). Publisher: American Physical Society, p. 075148. DOI: 10.1103/PhysRevB.102.075148. URL: https:

//link.aps.org/doi/10.1103/PhysRevB.102.075148 (visited on 05/09/2023).

[27] Masashi Kakihana et al. "Electronic States of Antiferromagnet FeSn and Pauli Paramagnet CoSn". In: *Journal of the Physical Society of Japan* 88.1 (Jan. 15, 2019). Publisher: The Physical Society of Japan, p. 014705. ISSN: 0031-9015. DOI: 10.7566/JPSJ.88.014705. URL: https://journals.jps.jp/doi/full/10.7566/JPSJ.88.014705 (visited on 05/08/2023).

[28] R. Masrour et al. "Electronic and magnetic structures of FeSn compound investigated by first principle, mean field and series expansions calculations". In: *Physica A: Statistical Mechanics and its Applications* 414 (Nov. 15, 2014), pp. 249–253. ISSN: 0378-4371. DOI: 10.1016/j.physa.2014.07.049. URL: https://www.sciencedirect.com/science/article/pii/S0378437114006335 (visited on 05/09/2023).

[29] Yaofeng Xie et al. "Spin excitations in metallic kagome lattice FeSn and CoSn". In: *Communications Physics* 4.1 (Nov. 11, 2021). Number: 1 Publisher: Nature Publishing Group, pp. 1–11. ISSN: 2399-3650. DOI: 10.1038/s42005-021-00736-8. URL: https://www.nature.com/articles/s42005-021-00736-8 (visited on 05/10/2023).

[30] Yi-Fan Zhang et al. "Ab initio study of spin fluctuations in the itinerant kagome magnet FeSn". In: *Physical Review B* 106.18 (Nov. 23, 2022). Publisher: American Physical Society, p. 184422. DOI: 10.1103/PhysRevB.106.184422. URL: https://link.aps.org/doi/10.1103/PhysRevB.106.184422 (visited on 05/10/2023).

[31] Seung-Hwan Do et al. "Damped Dirac magnon in the metallic kagome antiferromagnet FeSn". In: *Physical Review B* 105.18 (May 6, 2022). Publisher: American Physical Society, p. L180403. DOI: 10.1103/PhysRevB.105.L180403. URL: https://link.aps.org/doi/10.1103/PhysRevB.105.L180403 (visited on 05/10/2023).

[32] Yu Tao et al. "Investigating the magnetoelastic properties in FeSn and Fe_3Sn_2 flat band metals". In: *Physical Review B* 107.17 (May 5, 2023). Publisher: American Physical Society, p. 174407. DOI: 10.1103/PhysRevB.107.174407. URL: https://link.aps.org/doi/10.1103/PhysRevB.107.174407 (visited on 05/10/2023).

[33] Michael P. Marder. *Condensed Matter Physics*. John Wiley & Sons, Nov. 17, 2010. 986 pp. ISBN: 978-0-470-94994-8.

[34] Brian C. Sales et al. “Electronic, magnetic, and thermodynamic properties of the kagome layer compound FeSn”. In: *Physical Review Materials* 3.11 (Nov. 25, 2019). Publisher: American Physical Society, p. 114203. DOI: 10.1103/PhysRevMaterials.3.114203. URL: https://link.aps.org/doi/10.1103/PhysRevMaterials.3.114203 (visited on 05/09/2023).

[35] Hong Li et al. “Spin-polarized imaging of the antiferromagnetic structure and field-tunable bound states in kagome magnet FeSn”. In: *Scientific Reports* 12.1 (Aug. 25, 2022). Number: 1 Publisher: Nature Publishing Group, p. 14525. ISSN: 2045-2322. DOI: 10.1038/s41598-022-18678-8. URL: https://www.nature.com/articles/s41598-022-18678-8 (visited on 05/09/2023).

[36] Si-Hong Lee et al. “Spin-polarized and possible pseudospin-polarized scanning tunneling microscopy in kagome metal FeSn”. In: *Communications Physics* 5.1 (Sept. 22, 2022). Number: 1 Publisher: Nature Publishing Group, pp. 1–8. ISSN: 2399-3650. DOI: 10.1038/s42005-022-01012-z. URL: https://www.nature.com/articles/s42005-022-01012-z (visited on 05/09/2023).

[37] H.-M. Guo and M. Franz. “Topological insulator on the kagome lattice”. In: *Physical Review B* 80.11 (Sept. 25, 2009), p. 113102. ISSN: 1098-0121, 1550-235X. DOI: 10.1103/PhysRevB.80.113102. URL: https://link.aps.org/doi/10.1103/PhysRevB.80.113102 (visited on 05/08/2023).

[38] Enke Liu et al. “Giant anomalous Hall effect in a ferromagnetic kagome-lattice semimetal”. In: *Nature Physics* 14.11 (Nov. 2018). Number: 11 Publisher: Nature Publishing Group, pp. 1125–1131. ISSN: 1745-2481. DOI: 10.1038/s41567-018-0234-5. URL: https://www.nature.com/articles/s41567-018-0234-5 (visited on 05/08/2023).

[39] Linda Ye et al. “Massive Dirac fermions in a ferromagnetic kagome metal”. In: *Nature* 555.7698 (Mar. 2018). Number: 7698 Publisher: Nature Publishing Group, pp. 638–642. ISSN: 1476-4687. DOI: 10.1038/nature25987. URL: https://www.nature.com/articles/nature25987 (visited on 05/08/2023).

[40] Zhiyong Lin et al. “Flatbands and Emergent Ferromagnetic Ordering in Fe 3 Sn 2 Kagome Lattices”. In: *Physical Review Letters* 121.9 (Aug. 27, 2018), p. 096401. ISSN: 0031-9007, 1079-7114. DOI: 10.1103/PhysRevLett.121.096401. URL: https://link.aps.org/doi/10.1103/PhysRevLett.121.096401 (visited on 05/08/2023).

[41] C. Mielke et al. “Nodeless kagome superconductivity in $LaRu_3Si_2$”. In: *Physical Review Materials* 5.3 (Mar. 29, 2021). Publisher: American Physical Society, p. 034803. DOI: 10.1103/PhysRevMaterials.5.034803. URL: https://link.aps.org/doi/10.1103/PhysRevMaterials.5.034803 (visited on 05/08/2023).

[42] Zhonghao Liu et al. “Orbital-selective Dirac fermions and extremely flat bands in frustrated kagome-lattice metal CoSn”. In: *Nature Communications* 11.1 (Aug. 10, 2020). Number: 1 Publisher: Nature Publishing Group, p. 4002. ISSN: 2041-1723. DOI: 10.1038/s41467-020-17462-4. URL: https://www.nature.com/articles/s41467-020-17462-4 (visited on 05/09/2023).

[43] Mingu Kang et al. “Topological flat bands in frustrated kagome lattice CoSn”. In: *Nature Communications* 11.1 (Aug. 10, 2020). Number: 1 Publisher: Nature Publishing Group, p. 4004. ISSN: 2041-1723. DOI: 10.1038/s41467-020-17465-1. URL: https://www.nature.com/articles/s41467-020-17465-1 (visited on 05/09/2023).

[44] Domenico Di Sante et al. “Electronic correlations and universal long-range scaling in kagome metals”. In: *Physical Review Research* 5.1 (Jan. 19, 2023). Publisher: American Physical Society, p. L012008. DOI: 10.1103/PhysRevResearch.5.L012008. URL: https://link.aps.org/doi/10.1103/PhysRevResearch.5.L012008 (visited on 05/09/2023).

[45] David Bohm and David Pines. “A Collective Description of Electron Interactions. I. Magnetic Interactions”. In: *Physical Review* 82.5 (June 1, 1951). Publisher: American Physical Society, pp. 625–634. DOI: 10.1103/PhysRev.82.625. URL: https://link.aps.org/doi/10.1103/PhysRev.82.625 (visited on 05/11/2023).

[46] David Pines and David Bohm. “A Collective Description of Electron Interactions: II. Collective vs Individual Particle Aspects of the Interactions”. In: *Physical Review* 85.2 (Jan. 15, 1952). Publisher: American Physical Society, pp. 338–353. DOI: 10.1103/PhysRev.85.338. URL: https://link.aps.org/doi/10.1103/PhysRev.85.338 (visited on 05/11/2023).

[47] David Bohm and David Pines. “A Collective Description of Electron Interactions: III. Coulomb Interactions in a Degenerate Electron Gas”. In: *Physical Review* 92.3 (Nov. 1, 1953). Publisher: American Physical Society, pp. 609–625. DOI: 10.1103/PhysRev.92.609. URL: https://link.aps.org/doi/10.1103/PhysRev.92.609 (visited on 05/11/2023).

[48] Alexander L. Fetter and John Dirk Walecka. *Quantum Theory of Many-particle Systems*. Courier Corporation, June 20, 2003. 644 pp. ISBN: 978-0-486-42827-7.

[49] Stefan A. Maier. *Plasmonics: Fundamentals and Applications*. New York, NY: Springer US, 2007. ISBN: 978-0-387-33150-8 978-0-387-37825-1. DOI: 10.1007/0-387-37825-1. URL: http://link.springer.com/10.1007/0-387-37825-1 (visited on 05/09/2023).

[50] Y. Wang, E. W. Plummer, and K. Kempa. "Foundations of Plasmonics". In: *Advances in Physics* 60.5 (Oct. 1, 2011), pp. 799–898. ISSN: 0001-8732. DOI: 10.1080/00018732.2011.621320. URL: https://doi.org/10.1080/00018732.2011.621320 (visited on 05/09/2023).

[51] Henrik Bruus et al. *Many-Body Quantum Theory in Condensed Matter Physics: An Introduction*. Oxford Graduate Texts. Oxford, New York: Oxford University Press, Sept. 2, 2004. 464 pp. ISBN: 978-0-19-856633-5.

[52] Gabriele Giuliani and Giovanni Vignale. *Quantum Theory of the Electron Liquid*. Cambridge: Cambridge University Press, 2005. ISBN: 978-0-521-52796-5. DOI: 10.1017/CBO9780511619915. URL: https://www.cambridge.org/core/books/quantum-theory-of-the-electron-liquid/EA75F41350A1C41D5E1BD202D539BB9E (visited on 01/16/2023).

[53] Frank Stern. "Polarizability of a Two-Dimensional Electron Gas". In: *Physical Review Letters* 18.14 (Apr. 3, 1967). Publisher: American Physical Society, pp. 546–548. DOI: 10.1103/PhysRevLett.18.546. URL: https://link.aps.org/doi/10.1103/PhysRevLett.18.546 (visited on 05/11/2023).

[54] L. Marton et al. "Plural Scattering of 20-kev Electrons in Aluminum". In: *Physical Review* 126.1 (Apr. 1, 1962). Publisher: American Physical Society, pp. 182–192. DOI: 10.1103/PhysRev.126.182. URL: https://link.aps.org/doi/10.1103/PhysRev.126.182 (visited on 05/09/2023).

[55] R. F. Egerton. "Electron energy-loss spectroscopy in the TEM". In: *Reports on Progress in Physics* 72.1 (Dec. 2008), p. 016502. ISSN: 0034-4885. DOI: 10.1088/0034-4885/72/1/016502. URL: https://dx.doi.org/10.1088/0034-4885/72/1/016502 (visited on 05/11/2023).

[56] R. Brydson. *Electron Energy Loss Spectroscopy*. London: Garland Science, Aug. 14, 2020. 152 pp. ISBN: 978-1-00-307685-8. DOI: 10.1201/9781003076858.

[57] M.G. Bell and W.Y. Liang. "Electron energy loss studies in solids; The transition metal dichalcogenides". In: *Advances in Physics* 25.1 (Jan. 1, 1976), pp. 53–86. ISSN: 0001-8732. DOI: 10.1080/00018737600101362. URL: https://doi.org/10.1080/00018737600101362 (visited on 05/11/2023).

[58] Vladimir P. Oleshko. "Electron Energy-Loss Spectroscopy and Imaging". In: *Encyclopedia of Analytical Science (Third Edition)*. Ed. by Paul Worsfold et al. Oxford: Academic Press, Jan. 1, 2019, pp. 264–288. ISBN: 978-0-08-101984-9. DOI: 10.1016/B978-0-12-409547-2.14406-3. URL: https://www.sciencedirect.com/science/article/pii/B9780124095472144063 (visited on 05/11/2023).

[59] Silvana Botti and Matteo Gatti. "The Microscopic Description of a Macroscopic Experiment". In: *Fundamentals of Time-Dependent Density Functional Theory*. Ed. by Miguel A.L. Marques et al. Lecture Notes in Physics. Berlin, Heidelberg: Springer, 2012, pp. 29–50. ISBN: 978-3-642-23518-4. DOI: 10.1007/978-3-642-23518-4_3. URL: https://doi.org/10.1007/978-3-642-23518-4_3 (visited on 05/09/2023).

[60] Tom Westerhout et al. "Plasmon confinement in fractal quantum systems". In: *Physical Review B* 97.20 (May 21, 2018). Publisher: American Physical Society, p. 205434. DOI: 10.1103/PhysRevB.97.205434. URL: https://link.aps.org/doi/10.1103/PhysRevB.97.205434 (visited on 05/11/2023).

[61] Sean M. Anderson et al. "Plasmon dispersion in graphite: A comparison of current ab initio methods". In: *Physical Review B* 100.4 (July 22, 2019). Publisher: American Physical Society, p. 045205. DOI: 10.1103/PhysRevB.100.045205. URL: https://link.aps.org/doi/10.1103/PhysRevB.100.045205 (visited on 05/11/2023).

[62] Pierluigi Cudazzo et al. "High-energy collective electronic excitations in layered transition-metal dichalcogenides". In: *Physical Review B* 90.12 (Sept. 16, 2014). Publisher: American Physical Society, p. 125125. DOI: 10.1103/PhysRevB.90.125125. URL: https://link.aps.org/doi/10.1103/PhysRevB.90.125125 (visited on 05/11/2023).

[63] L. Hung et al. "Interpretation of monoclinic hafnia valence electron energy-loss spectra by time-dependent density functional theory". In: *Physical Review B* 93.16 (Apr. 6, 2016). Publisher: American Physical Society, p. 165105. DOI: 10.1103/PhysRevB.93.165105. URL: https://link.aps.org/doi/10.1103/PhysRevB.93.165105 (visited on 05/11/2023).

[64] R. H. Ritchie. "Surface plasmons in solids". In: *Surface Science* 34.1 (Jan. 1, 1973), pp. 1–19. ISSN: 0039-6028. DOI: 10.1016/0039-6028(73)90183-0. URL: https://www.sciencedirect.com/science/article/pii/0039602873901830 (visited on 05/09/2023).

[65] J. M. Pitarke et al. "Theory of surface plasmons and surface-plasmon polaritons". In: *Reports on Progress in Physics* 70.1 (Dec. 2006), p. 1. ISSN: 0034-4885. DOI: 10.1088/0034-4885/70/1/R01. URL: https://dx.doi.org/10.1088/0034-4885/70/1/R01 (visited on 05/09/2023).

[66] Eric C. Le Ru and Pablo G. Etchegoin. "Chapter 3 - Introduction to plasmons and plasmonics". In: *Principles of Surface-Enhanced Raman Spectroscopy*. Ed. by Eric C. Le Ru and Pablo G. Etchegoin. Amsterdam: Elsevier, Jan. 1, 2009, pp. 121–183. ISBN: 978-0-444-52779-0. DOI: 10.1016/B978-0-444-52779-0.00009-X. URL: https://www.sciencedirect.com/science/article/pii/B978044452779000009X (visited on 05/09/2023).

[67] Kristian Sommer Thygesen. "Calculating excitons, plasmons, and quasiparticles in 2D materials and van der Waals heterostructures". In: *2D Materials* 4.2 (June 2017). Publisher: IOP Publishing, p. 022004. ISSN: 2053-1583. DOI: 10.1088/2053-1583/aa6432. URL: https://dx.doi.org/10.1088/2053-1583/aa6432 (visited on 05/11/2023).

[68] Stephen Blundell and Stephen Blundell. *Magnetism in Condensed Matter*. Oxford Master Series in Physics. Oxford, New York: Oxford University Press, Oct. 4, 2001. 256 pp. ISBN: 978-0-19-850591-4.

[69] Olle Eriksson et al. *Atomistic Spin Dynamics: Foundations and Applications*. Oxford, New York: Oxford University Press, Feb. 23, 2017. 266 pp. ISBN: 978-0-19-878866-9.

[70] Sergio M. Rezende. *Fundamentals of Magnonics*. Vol. 969. Lecture Notes in Physics. Cham: Springer International Publishing, 2020. ISBN: 978-3-030-41316-3 978-3-030-41317-0. DOI: 10.1007/978-3-030-41317-0. URL: https://link.springer.com/10.1007/978-3-030-41317-0 (visited on 05/11/2023).

[71] Corina Etz et al. "Atomistic spin dynamics and surface magnons". In: *Journal of Physics. Condensed Matter: An Institute of Physics Journal* 27.24 (June 24, 2015), p. 243202. ISSN: 1361-648X. DOI: 10.1088/0953-8984/27/24/243202.

[72] Tôru Moriya. *Spin Fluctuations in Itinerant Electron Magnetism*. Red. by Peter Fulde, Manuel Cardona, and Hans-Joachim Queisser. Vol. 56. Springer Series in Solid-State Sciences. Berlin, Heidelberg: Springer, 1985. ISBN: 978-3-642-82501-9 978-3-642-82499-9. DOI: 10.1007/978-3-642-82499-9. URL: http://link.springer.com/10.1007/978-3-642-82499-9 (visited on 05/11/2023).

[73] N. Tancogne-Dejean, F. G. Eich, and A. Rubio. "Time-Dependent Magnons from First Principles". In: *Journal of Chemical Theory and Computation* 16.2 (Feb. 11, 2020). Publisher: American Chemical Society, pp. 1007–1017. ISSN: 1549-9618. DOI: 10.1021/acs.jctc.9b01064. URL: https://doi.org/10.1021/acs.jctc.9b01064 (visited on 05/11/2023).

[74] Anjan Barman et al. "The 2021 Magnonics Roadmap". In: *Journal of Physics. Condensed Matter: An Institute of Physics Journal* 33.41 (Aug. 5, 2021). ISSN: 1361-648X. DOI: 10.1088/1361-648X/abec1a.

[75] Léon Van Hove. "Time-Dependent Correlations between Spins and Neutron Scattering in Ferromagnetic Crystals". In: *Physical Review* 95.6 (Sept. 15, 1954). Publisher: American Physical Society, pp. 1374–1384. DOI: 10.1103/PhysRev.95.1374. URL: https://link.aps.org/doi/10.1103/PhysRev.95.1374 (visited on 05/11/2023).

[76] J. W. Lynn and H. A. Mook. "Temperature dependence of the dynamic susceptibility of nickel". In: *Physical Review B* 23.1 (Jan. 1, 1981). Publisher: American Physical Society, pp. 198–206. DOI: 10.1103/PhysRevB.23.198. URL: https://link.aps.org/doi/10.1103/PhysRevB.23.198 (visited on 05/11/2023).

[77] Tommaso Gorni et al. "turboMagnon – A code for the simulation of spin-wave spectra using the Liouville-Lanczos approach to time-dependent density-functional perturbation theory". In: *Computer Physics Communications* 280 (Nov. 1, 2022), p. 108500. ISSN: 0010-4655. DOI: 10.1016/j.cpc.2022.108500. URL: https://www.sciencedirect.com/science/article/pii/S0010465522002193 (visited on 05/09/2023).

[78] Carsten A. Ullrich and Carsten A. Ullrich. *Time-Dependent Density-Functional Theory: Concepts and Applications*. Oxford Graduate Texts. Oxford, New York: Oxford University Press, Dec. 22, 2011. 542 pp. ISBN: 978-0-19-956302-9.

[79] Simo Huotari. "Spectroscopy in the Frequency Domain". In: *Fundamentals of Time-Dependent Density Functional Theory*. Ed. by Miguel A.L. Marques et al. Lecture Notes in Physics. Berlin, Heidelberg: Springer, 2012,

pp. 15–28. ISBN: 978-3-642-23518-4. DOI: 10.1007/978-3-642-23518-4_2. URL: https://doi.org/10.1007/978-3-642-23518-4_2 (visited on 05/09/2023).

[80] David S. Sholl and Janice A. Steckel. *Density Functional Theory: A Practical Introduction*. John Wiley & Sons, Sept. 20, 2011. 194 pp. ISBN: 978-1-118-21104-5.

[81] June Gunn Lee. *Computational Materials Science: An Introduction, Second Edition*. 2nd ed. Boca Raton: CRC Press, Nov. 25, 2016. 376 pp. ISBN: 978-1-315-36842-9. DOI: 10.1201/9781315368429.

[82] R. O. Jones. "Density functional theory: Its origins, rise to prominence, and future". In: *Reviews of Modern Physics* 87.3 (Aug. 25, 2015). Publisher: American Physical Society, pp. 897–923. DOI: 10.1103/RevModPhys.87.897. URL: https://link.aps.org/doi/10.1103/RevModPhys.87.897 (visited on 05/10/2023).

[83] K. Lejaeghere et al. "Error Estimates for Solid-State Density-Functional Theory Predictions: An Overview by Means of the Ground-State Elemental Crystals". In: *Critical Reviews in Solid State and Materials Sciences* 39.1 (Jan. 1, 2014), pp. 1–24. ISSN: 1040-8436. DOI: 10.1080/10408436.2013.772503. URL: https://doi.org/10.1080/10408436.2013.772503 (visited on 05/10/2023).

[84] Peiyu Cao et al. "Tests on the Accuracy and Scalability of the Full-Potential DFT Method Based on Multiple Scattering Theory". In: *Frontiers in Chemistry* 8 (2020). ISSN: 2296-2646. URL: https://www.frontiersin.org/articles/10.3389/fchem.2020.590047 (visited on 05/10/2023).

[85] Priyanka Makkar and Narendra Nath Ghosh. "A review on the use of DFT for the prediction of the properties of nanomaterials". In: *RSC Advances* 11.45 (2021). Publisher: Royal Society of Chemistry, pp. 27897–27924. DOI: 10.1039/D1RA04876G. URL: https://pubs.rsc.org/en/content/articlelanding/2021/ra/d1ra04876g (visited on 05/10/2023).

[86] Jörg Neugebauer and Tilmann Hickel. "Density functional theory in materials science". In: *WIREs Computational Molecular Science* 3.5 (2013), pp. 438–448. ISSN: 1759-0884. DOI: 10.1002/wcms.1125. URL: https://onlinelibrary.wiley.com/doi/abs/10.1002/wcms.1125 (visited on 05/10/2023).

[87] Philip J. Hasnip et al. "Density functional theory in the solid state". In: *Philosophical Transactions of the Royal Society A: Mathematical, Physical and Engineering Sciences* 372.2011 (Mar. 13, 2014). Publisher: Royal Society, p. 20130270. DOI: 10.1098/rsta.2013.0270. URL: https://royalsocietypublishing.org/doi/10.1098/rsta.2013.0270 (visited on 05/10/2023).

[88] Tanja van Mourik, Michael Bühl, and Marie-Pierre Gaigeot. "Density functional theory across chemistry, physics and biology". In: *Philosophical Transactions of the Royal Society A: Mathematical, Physical and Engineering Sciences* 372.2011 (Mar. 13, 2014). Publisher: Royal Society, p. 20120488. DOI: 10.1098/rsta.2012.0488. URL: https://royalsocietypublishing.org/doi/10.1098/rsta.2012.0488 (visited on 05/10/2023).

[89] Ann E. Mattsson et al. "Designing meaningful density functional theory calculations in materials science—a primer". In: *Modelling and Simulation in Materials Science and Engineering* 13.1 (Nov. 2004), R1. ISSN: 0965-0393. DOI: 10.1088/0965-0393/13/1/R01. URL: https://dx.doi.org/10.1088/0965-0393/13/1/R01 (visited on 05/10/2023).

[90] Kaoru Ohno, Keivan Esfarjani, and Yoshiyuki Kawazoe. "Ab Initio Methods". In: *Computational Materials Science: From Ab Initio to Monte Carlo Methods*. Ed. by Kaoru Ohno, Keivan Esfarjani, and Yoshiyuki Kawazoe. Berlin, Heidelberg: Springer, 2018, pp. 7–197. ISBN: 978-3-662-56542-1. DOI: 10.1007/978-3-662-56542-1_2. URL: https://doi.org/10.1007/978-3-662-56542-1_2 (visited on 05/10/2023).

[91] Feliciano Giustino and Feliciano Giustino. *Materials Modelling using Density Functional Theory: Properties and Predictions*. Oxford, New York: Oxford University Press, May 15, 2014. 304 pp. ISBN: 978-0-19-966243-2.

[92] Stefano Baroni et al. "Phonons and related crystal properties from density-functional perturbation theory". In: *Reviews of Modern Physics* 73.2 (July 6, 2001). Publisher: American Physical Society, pp. 515–562. DOI: 10.1103/RevModPhys.73.515. URL: https://link.aps.org/doi/10.1103/RevModPhys.73.515 (visited on 05/10/2023).

[93] Paolo Giannozzi and Stefano Baroni. "Density-Functional Perturbation Theory". In: *Handbook of Materials Modeling: Methods*. Ed. by Sidney Yip. Dordrecht: Springer Netherlands, 2005, pp. 195–214. ISBN: 978-1-4020-3286-8. DOI: 10.1007/978-1-4020-3286-8_11. URL: https://doi.org/10.1007/978-1-4020-3286-8_11 (visited on 05/10/2023).

[94] P. Hohenberg and W. Kohn. “Inhomogeneous Electron Gas”. In: *Physical Review* 136.3 (Nov. 9, 1964). Publisher: American Physical Society, B864–B871. DOI: 10.1103/PhysRev.136.B864. URL: https://link.aps.org/doi/10.1103/PhysRev.136.B864 (visited on 05/10/2023).

[95] W. Kohn. “Nobel Lecture: Electronic structure of matter—wave functions and density functionals”. In: *Reviews of Modern Physics* 71.5 (Oct. 1, 1999). Publisher: American Physical Society, pp. 1253–1266. DOI: 10.1103/RevModPhys.71.1253. URL: https://link.aps.org/doi/10.1103/RevModPhys.71.1253 (visited on 05/09/2023).

[96] W. Kohn and L. J. Sham. “Self-Consistent Equations Including Exchange and Correlation Effects”. In: *Physical Review* 140.4 (Nov. 15, 1965). Publisher: American Physical Society, A1133–A1138. DOI: 10.1103/PhysRev.140.A1133. URL: https://link.aps.org/doi/10.1103/PhysRev.140.A1133 (visited on 05/10/2023).

[97] Kieron Burke and Lucas O. Wagner. “DFT in a nutshell”. In: *International Journal of Quantum Chemistry* 113.2 (2013), pp. 96–101. ISSN: 1097-461X. DOI: 10.1002/qua.24259. URL: https://onlinelibrary.wiley.com/doi/abs/10.1002/qua.24259 (visited on 05/10/2023).

[98] Sebastian Dick and Marivi Fernandez-Serra. “Machine learning accurate exchange and correlation functionals of the electronic density”. In: *Nature Communications* 11.1 (July 14, 2020). Number: 1 Publisher: Nature Publishing Group, p. 3509. ISSN: 2041-1723. DOI: 10.1038/s41467-020-17265-7. URL: https://www.nature.com/articles/s41467-020-17265-7 (visited on 05/10/2023).

[99] John P. Perdew and Karla Schmidt. “Jacob’s ladder of density functional approximations for the exchange-correlation energy”. In: *AIP Conference Proceedings* 577.1 (July 6, 2001), pp. 1–20. ISSN: 0094-243X. DOI: 10.1063/1.1390175. URL: https://doi.org/10.1063/1.1390175 (visited on 05/10/2023).

[100] Ann E. Mattsson. “In Pursuit of the "Divine" Functional”. In: *Science* 298.5594 (Oct. 25, 2002). Publisher: American Association for the Advancement of Science, pp. 759–760. DOI: 10.1126/science.1077710. URL: https://www.science.org/doi/10.1126/science.1077710 (visited on 05/10/2023).

[101] Roberto Peverati and Donald G. Truhlar. “Quest for a universal density functional: the accuracy of density functionals across a broad spectrum of databases in chemistry and physics”. In: *Philosophical Transac-*

tions of the Royal Society A: Mathematical, Physical and Engineering Sciences 372.2011 (Mar. 13, 2014). Publisher: Royal Society, p. 20120476. DOI: 10.1098/rsta.2012.0476. URL: https://royalsocietypublishing.org/doi/10.1098/rsta.2012.0476 (visited on 05/10/2023).

[102] Carsten A. Ullrich and Zeng-hui Yang. "A Brief Compendium of Time-Dependent Density Functional Theory". In: *Brazilian Journal of Physics* 44.1 (Feb. 1, 2014), pp. 154–188. ISSN: 1678-4448. DOI: 10.1007/s13538-013-0141-2. URL: https://doi.org/10.1007/s13538-013-0141-2 (visited on 05/10/2023).

[103] Eberhard K. U. Gross and Neepa T. Maitra. "Introduction to TDDFT". In: *Fundamentals of Time-Dependent Density Functional Theory*. Ed. by Miguel A.L. Marques et al. Lecture Notes in Physics. Berlin, Heidelberg: Springer, 2012, pp. 53–99. ISBN: 978-3-642-23518-4. DOI: 10.1007/978-3-642-23518-4_4. URL: https://doi.org/10.1007/978-3-642-23518-4_4 (visited on 01/16/2023).

[104] Erich Runge and E. K. U. Gross. "Density-Functional Theory for Time-Dependent Systems". In: *Physical Review Letters* 52.12 (Mar. 19, 1984). Publisher: American Physical Society, pp. 997–1000. DOI: 10.1103/PhysRevLett.52.997. URL: https://link.aps.org/doi/10.1103/PhysRevLett.52.997 (visited on 05/10/2023).

[105] Robert van Leeuwen. "Mapping from Densities to Potentials in Time-Dependent Density-Functional Theory". In: *Physical Review Letters* 82.19 (May 10, 1999). Publisher: American Physical Society, pp. 3863–3866. DOI: 10.1103/PhysRevLett.82.3863. URL: https://link.aps.org/doi/10.1103/PhysRevLett.82.3863 (visited on 05/10/2023).

[106] John P. Perdew and Yue Wang. "Accurate and simple analytic representation of the electron-gas correlation energy". In: *Physical Review B* 45.23 (June 15, 1992). Publisher: American Physical Society, pp. 13244–13249. DOI: 10.1103/PhysRevB.45.13244. URL: https://link.aps.org/doi/10.1103/PhysRevB.45.13244 (visited on 05/10/2023).

[107] Valerio Olevano. "TDDFT, excitations, and spectroscopy". In: *TDDFT, excitations, and spectroscopy*. De Gruyter, Mar. 5, 2018, pp. 101–142. ISBN: 978-3-11-043392-0. DOI: 10.1515/9783110433920-004. URL: https://www.degruyter.com/document/doi/10.1515/9783110433920-004/html (visited on 05/10/2023).

[108] David A. Strubbe et al. “Response Functions in TDDFT: Concepts and Implementation”. In: *Fundamentals of Time-Dependent Density Functional Theory*. Ed. by Miguel A.L. Marques et al. Lecture Notes in Physics. Berlin, Heidelberg: Springer, 2012, pp. 139–166. ISBN: 978-3-642-23518-4. DOI: 10.1007/978-3-642-23518-4_7. URL: https://doi.org/10.1007/978-3-642-23518-4_7 (visited on 01/16/2023).

[109] Silvana Botti et al. “Time-dependent density-functional theory for extended systems”. In: *Reports on Progress in Physics* 70.3 (Feb. 2007), p. 357. ISSN: 0034-4885. DOI: 10.1088/0034-4885/70/3/R02. URL: https://dx.doi.org/10.1088/0034-4885/70/3/R02 (visited on 05/10/2023).

[110] N. Singh et al. “Adiabatic generalized gradient approximation kernel in time-dependent density functional theory”. In: *Physical Review B* 99.3 (Jan. 25, 2019). Publisher: American Physical Society, p. 035151. DOI: 10.1103/PhysRevB.99.035151. URL: https://link.aps.org/doi/10.1103/PhysRevB.99.035151 (visited on 05/09/2023).

[111] Thorbjørn Skovhus and Thomas Olsen. “Dynamic transverse magnetic susceptibility in the projector augmented-wave method: Application to Fe, Ni, and Co”. In: *Physical Review B* 103.24 (June 7, 2021). Publisher: American Physical Society, p. 245110. DOI: 10.1103/PhysRevB.103.245110. URL: https://link.aps.org/doi/10.1103/PhysRevB.103.245110 (visited on 05/11/2023).

[112] Kun Cao et al. “Ab initio calculation of spin fluctuation spectra using time-dependent density functional perturbation theory, plane waves, and pseudopotentials”. In: *Physical Review B* 97.2 (Jan. 19, 2018). Publisher: American Physical Society, p. 024420. DOI: 10.1103/PhysRevB.97.024420. URL: https://link.aps.org/doi/10.1103/PhysRevB.97.024420 (visited on 05/11/2023).

[113] Thorbjørn Skovhus and Thomas Olsen. “Magnons in antiferromagnetic bcc Cr and ${\mathrm{Cr}}_{2}{\mathrm{O}}_{3}$ from time-dependent density functional theory”. In: *Physical Review B* 106.8 (Aug. 22, 2022). Publisher: American Physical Society, p. 085131. DOI: 10.1103/PhysRevB.106.085131. URL: https://link.aps.org/doi/10.1103/PhysRevB.106.085131 (visited on 05/11/2023).

[114] S. Sharma, J. K. Dewhurst, and E. K. U. Gross. “Optical Response of Extended Systems Using Time-Dependent Density Functional Theory”. In: *First Principles Approaches to Spectroscopic Properties of Complex Materials*. Ed. by Cristiana Di Valentin, Silvana Botti, and Matteo Cococcioni.

Topics in Current Chemistry. Berlin, Heidelberg: Springer, 2014, pp. 235–257. ISBN: 978-3-642-55068-3. DOI: 10.1007/128_2014_529. URL: https://doi.org/10.1007/128_2014_529 (visited on 05/09/2023).

[115] Bruno Rousseau, Asier Eiguren, and Aitor Bergara. "Efficient computation of magnon dispersions within time-dependent density functional theory using maximally localized Wannier functions". In: *Physical Review B* 85.5 (Feb. 17, 2012). Publisher: American Physical Society, p. 054305. DOI: 10.1103/PhysRevB.85.054305. URL: https://link.aps.org/doi/10.1103/PhysRevB.85.054305 (visited on 05/11/2023).

[116] *The Elk Code*. URL: http://elk.sourceforge.net/.

[117] A. M. Van der Kraan and K. H. J. Buschow. "The 57Fe Mössbauer isomer shift in intermetallic compounds of iron". In: *Physica B+C* 138.1 (Mar. 2, 1986), pp. 55–62. ISSN: 0378-4363. DOI: 10.1016/0378-4363(86)90492-4. URL: https://www.sciencedirect.com/science/article/pii/0378436386904924 (visited on 05/12/2023).

[118] S. Ligenza. "A Spin-Flip Effect in FeSn". In: *physica status solidi (b)* 45.2 (1971), pp. 721–727. ISSN: 1521-3951. DOI: 10.1002/pssb.2220450236. URL: https://onlinelibrary.wiley.com/doi/abs/10.1002/pssb.2220450236 (visited on 05/12/2023).

[119] David Singh and Lars Nordström. *Planewaves, Pseudopotentials and the LAPW Method*. Springer US, 2006. ISBN: 978-0-387-28780-5. DOI: 10.1007/978-0-387-29684-5. URL: http://link.springer.com/10.1007/978-0-387-29684-5 (visited on 05/12/2023).

[120] Pierluigi Cudazzo, Matteo Gatti, and Angel Rubio. "Local-field effects on the plasmon dispersion of two-dimensional transition metal dichalcogenides". In: *New Journal of Physics* 15.12 (Dec. 2013). Publisher: IOP Publishing, p. 125005. ISSN: 1367-2630. DOI: 10.1088/1367-2630/15/12/125005. URL: https://dx.doi.org/10.1088/1367-2630/15/12/125005 (visited on 05/12/2023).

[121] Felipe H. da Jornada et al. "Universal slow plasmons and giant field enhancement in atomically thin quasi-two-dimensional metals". In: *Nature Communications* 11.1 (Feb. 21, 2020). Number: 1 Publisher: Nature Publishing Group, p. 1013. ISSN: 2041-1723. DOI: 10.1038/s41467-020-14826-8. URL: https://www.nature.com/articles/s41467-020-14826-8 (visited on 05/12/2023).

[122] Jeffrey Goldstone, Abdus Salam, and Steven Weinberg. "Broken Symmetries". In: *Physical Review* 127.3 (Aug. 1, 1962). Publisher: American Physical Society, pp. 965–970. DOI: 10.1103/PhysRev.127.965. URL: https://link.aps.org/doi/10.1103/PhysRev.127.965 (visited on 05/12/2023).

[123] Nisha Singh. "Ab-initio study of magnons in linear and non-linear regimes". In: (2019). Accepted: 2019-12-03T09:10:47Z. DOI: 10.17169/refubium-25791. URL: https://refubium.fu-berlin.de/handle/fub188/26032 (visited on 05/09/2023).

[124] Peter Mohn. *Magnetism in the Solid State*. Vol. 134. Solid-State Sciences. Berlin/Heidelberg: Springer-Verlag, 2006. ISBN: 978-3-540-29384-2. DOI: 10.1007/3-540-30981-0. URL: http://link.springer.com/10.1007/3-540-30981-0 (visited on 05/11/2023).

[125] Sergio M. Rezende, Antonio Azevedo, and Roberto L. Rodríguez-Suárez. "Introduction to antiferromagnetic magnons". In: *Journal of Applied Physics* 126.15 (Oct. 15, 2019), p. 151101. ISSN: 0021-8979. DOI: 10.1063/1.5109132. URL: https://doi.org/10.1063/1.5109132 (visited on 05/27/2023).

[126] Han Gao et al. "Ultra-flat and long-lived plasmons in a strongly correlated oxide". In: *Nature Communications* 13.1 (Aug. 9, 2022). Number: 1 Publisher: Nature Publishing Group, p. 4662. ISSN: 2041-1723. DOI: 10.1038/s41467-022-32359-0. URL: https://www.nature.com/articles/s41467-022-32359-0 (visited on 05/12/2023).

APPENDICES

APPENDIX

A

CONVERGENCE TESTS

To illustrate the convergence tests performed, the curves obtained for different parameters of the loss function for bulk FeSn are shown. The convergence tests for the loss function of monolayer FeSn as well as for the transverse magnetic response function of bulk and monolayer FeSn proceed in a similar manner: a parameter is varied while keeping all other parameters the same; the converged value is then chosen as the value to use in calculations, and one proceeds to test for convergence with respect to another parameter.

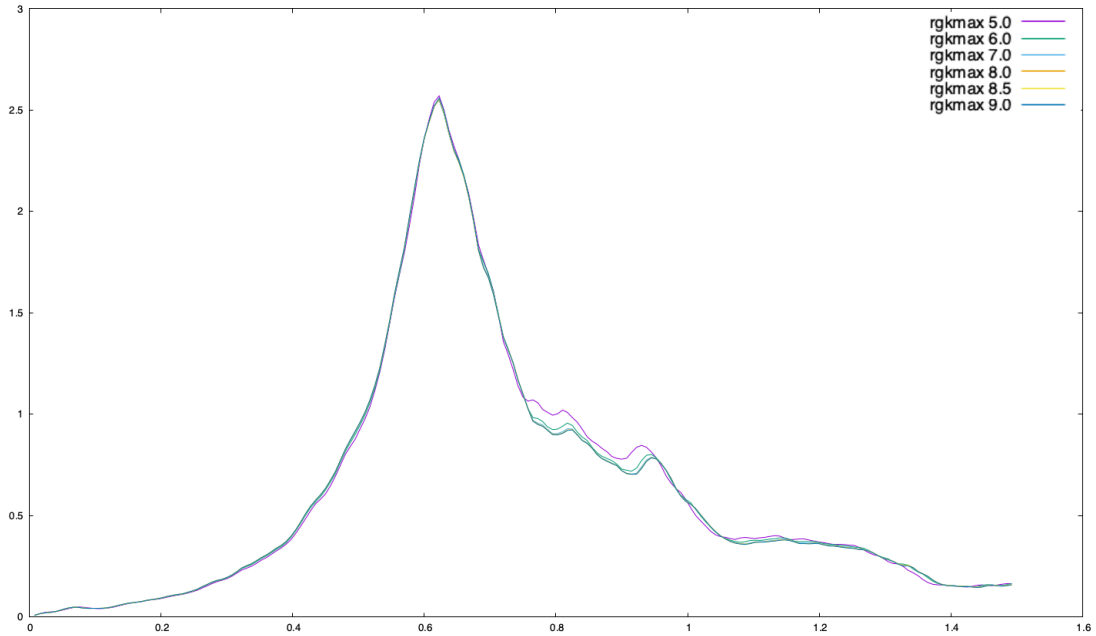

Figure A.0.1: The loss function for various values of the parameter `rgkmax`.

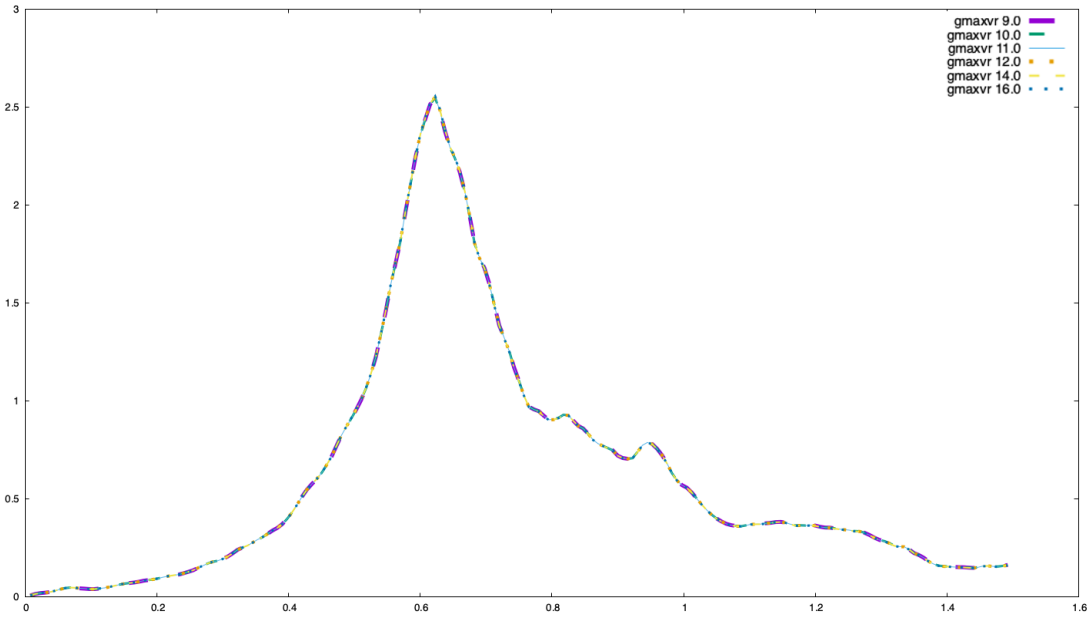

Figure A.0.2: The loss function for various values of the parameter `gmaxvr`.

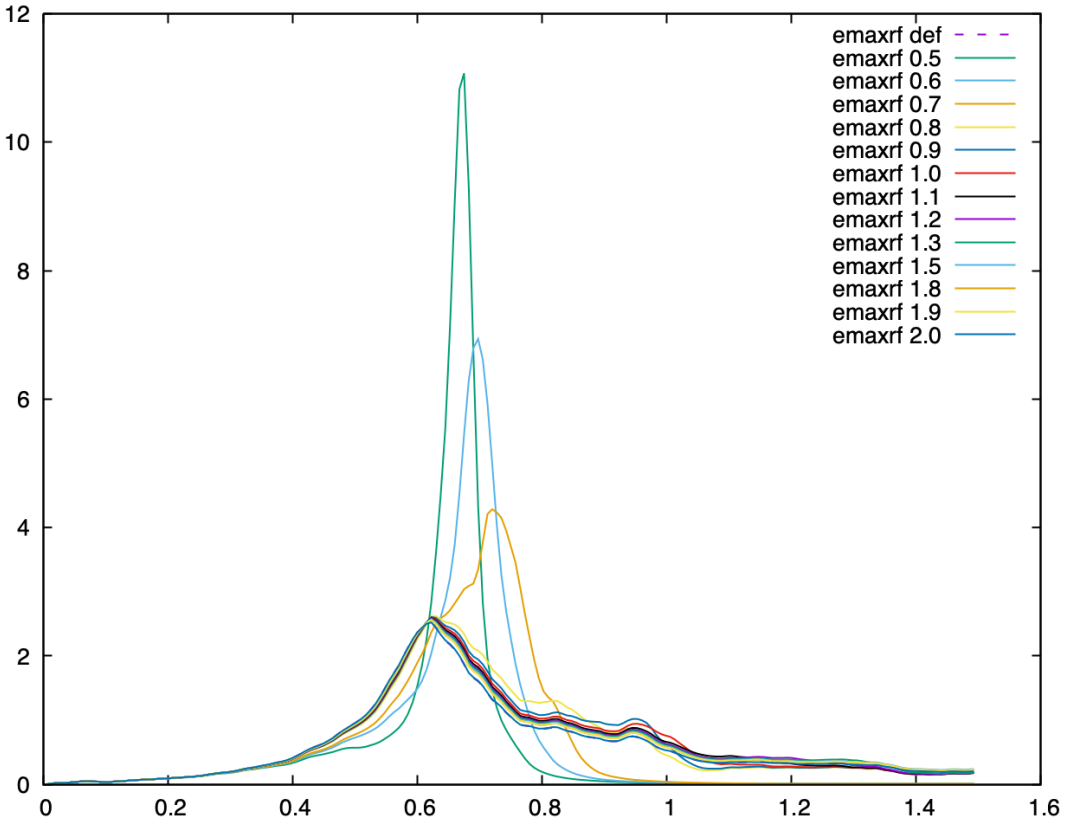

Figure A.0.3: The loss function for various values of the parameter `emaxrf`.

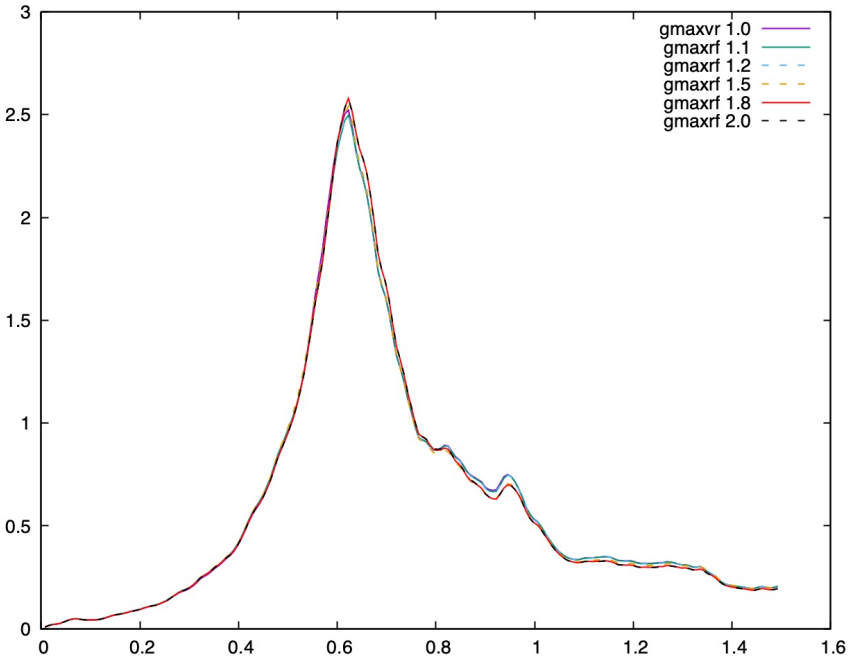

Figure A.0.4: The loss function for various values of the parameter `gmaxrf` for a k-point mesh of $12 \times 12 \times 6$.

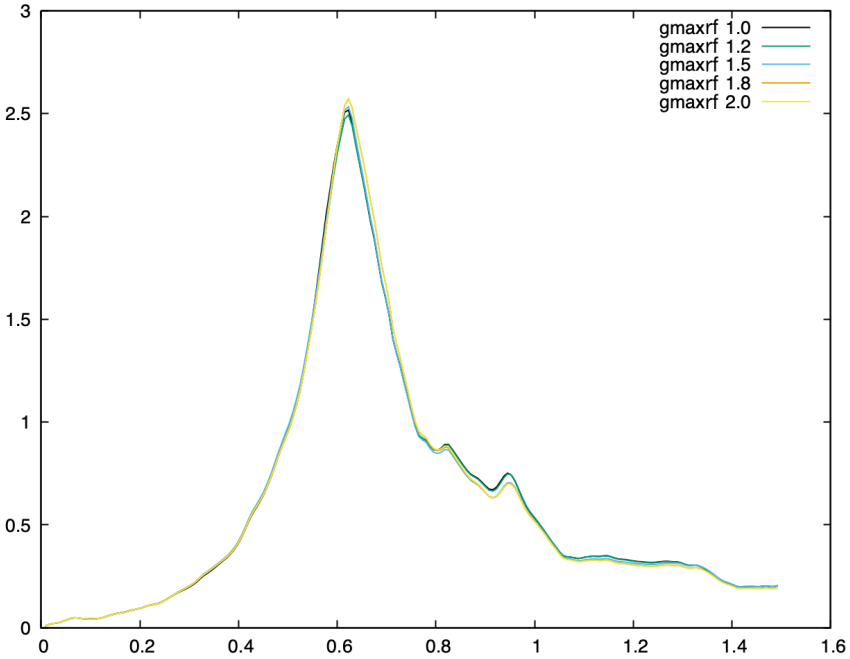

Figure A.0.5: The loss function for various values of the parameter `gmaxrf` for a k-point mesh of $16 \times 16 \times 8$.

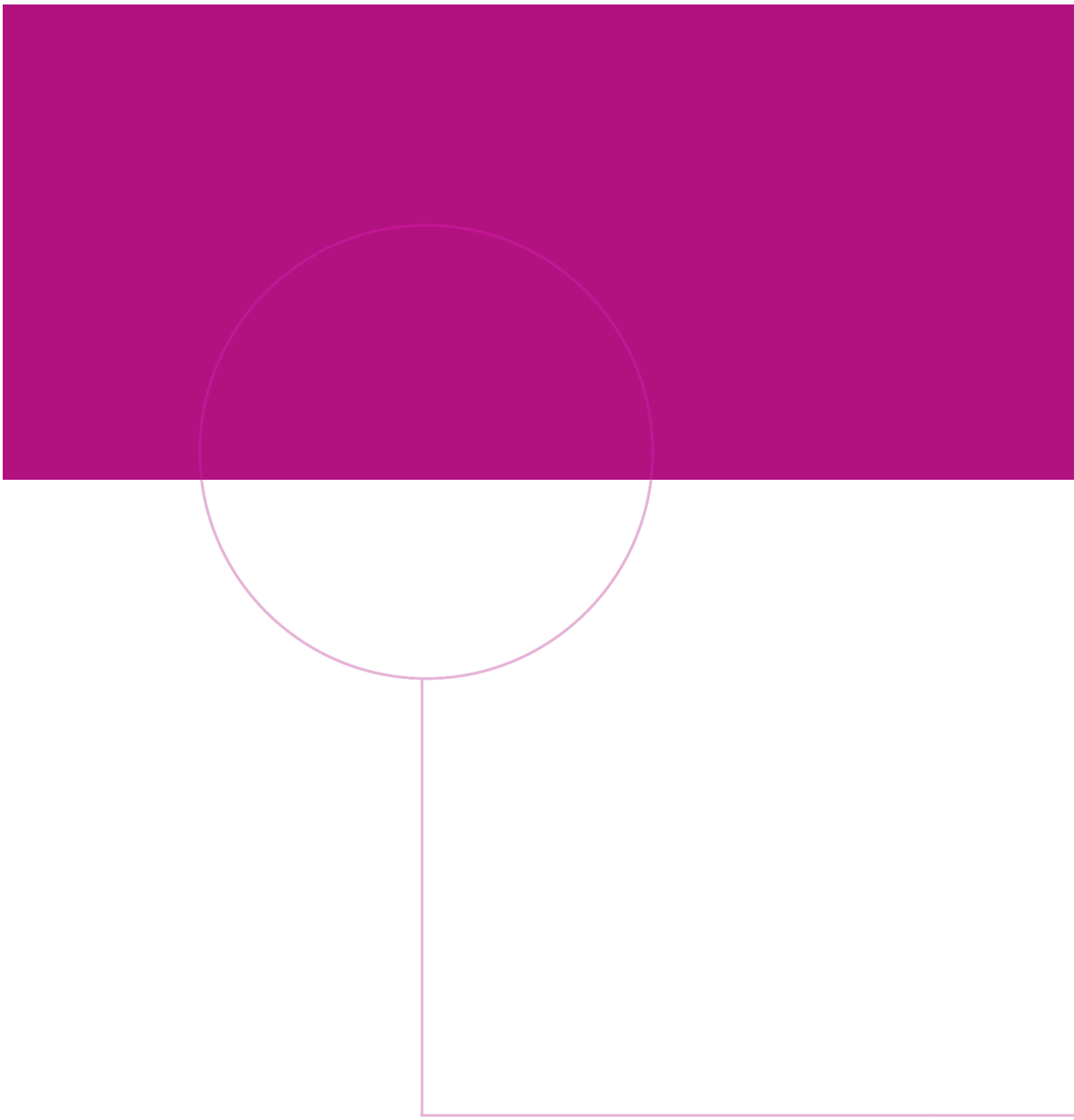

NTNU

Norwegian University of
Science and Technology